

Topological crystalline insulators: From two to three dimensions



Leibniz Institute
for Solid State and
Materials Research
Dresden



TECHNISCHE
UNIVERSITÄT
DRESDEN

Sanjib Kumar Das
geboren am 25.06.1993 in Kalkutta, Indien

Fachrichtung Physik
Fakultät für Mathematik und Naturwissenschaften

This dissertation is submitted for the degree of
Doctor of Philosophy

Eingereicht am: 07.10.2021

Verteidigt am: 27.01.2022

1. Gutachter: Prof. Dr. Jeroen van den Brink
2. Gutachter: Dr. Carmine Ortix

To my parents and grandparents

Table of contents

1	Introduction	1
1.1	Preface	1
1.2	Berry connection and Berry curvature	4
1.3	Quantum Hall effect	6
1.3.1	Bulk-Edge picture and Chern number	8
1.4	Quantum spin Hall effect: two dimensional (2D) time-reversal invariant topological insulators	10
1.4.1	\mathbb{Z}_2 topological invariant	13
1.5	Topological Crystalline Insulators (TCI)	15
1.6	This thesis	18
1.6.1	Outline of the chapters	18
1.6.2	Chapter2	18
1.6.3	Chapter3	19
1.6.4	Chapter4	19
1.6.5	Chapter5	20
2	Topological crystalline insulators from stacked graphene layers	23
2.1	Introduction	23
2.2	Stack of Chern insulating layers of graphene	25
2.3	Stack of quantum spin-Hall layers of graphene	31
2.4	Conclusion	34
3	Dual topology in Jacutingaite Pt_2HgSe_3	37
3.1	Introduction	37
3.2	Topological characterization	38
3.3	Surface Dirac cones	41
3.4	Tight-binding models	42
3.5	Conclusion	47

3.6 Appendix A:Ab-initio results for Pd_2HgSe_3	49
3.7 Appendix B:Different surface Dirac cone positions	50
3.8 Appendix C:Real-space hopping terms	51
4 Hinge electronic structure of strained half-Heuslers	55
4.1 Introduction	55
4.2 Methods	57
4.3 Lithium half-Heuslers	57
4.4 Low energy models	60
4.5 Hinge electronic structure	63
4.6 Conclusions	67
4.7 Appendix: Eight band tight-binding Hamiltonian	69
5 Topological Magnus responses in two and three dimensional systems	77
5.1 Introduction	77
5.2 Formalism of Magnus transport	79
5.3 Results	84
5.3.1 Strained monolayer graphene	84
5.3.2 Strained bilayer graphene	90
5.3.3 Hexagonal warped topological insulator	96
5.3.4 Weyl semimetals	99
5.4 Conclusions	103
6 Conclusion and Outlook	107
Publications	110
Acknowledgement	112
Bibliography	115
List of figures	143
List of tables	155

Chapter 1

Introduction

1.1 Preface

One of the most challenging goals of solid state physics is to search for exotic phases of matter which arise from the quantum nature of electrons. Earlier, the conventional band theory of solids classified materials into three broad categories, namely metals, insulators, and semi-conductors. However, it faced a major surprise after the realization of *topological phases* of matter which required modification of the band theory, in the sense that we learned about the importance of geometric nature of quantum states. The birth of such a topological phase dates back to 1980, when Klaus von Klitzing discovered the Quantum Hall effect [1, 2]. The observation was that, electrons in two dimensions subject to a low temperature and a strong magnetic field show step like features in the resistance. With this major discovery and later on pioneering works by Thouless, Haldane [3, 4] led to the establishment of a new class of materials characterized by topological order.

The fascinating aspect of topological systems is that even though they are insulating in bulk, there exist anomalous states at the boundaries of the system which can conduct [5, 6]. Moreover, these boundary states are usually quantized in number and feature robust dissipationless transport. The robustness arises from the fact that the boundary states are *symmetry* protected (except in the quantum Hall effect which belongs to class A in 1.1), meaning, unless one breaks the bulk symmetry associated with these topological states, or closes the bulk gap, the states do not disappear, and hence show robust topological protection. This remarkable feature has opened up a new range of technological

applications. Particularly, in the field of spintronics devices [7, 8] and topological quantum computers [9–11], one can make use of this robustness feature to counter decoherence effects.

Now that we have mentioned about the existence of such anomalous boundary transport, it is also important to understand how one can characterize such a symmetry protected topological state. As mentioned before, those boundary modes being bulk symmetry protected (bulk-boundary correspondence principle), one can construct a number dubbed as *topological invariant* using the bulk eigenstates to characterize the topology of the system. This number going from zero to nonzero indicates a topological phase transition from a trivial insulating phase. At first, the *topological invariant* may seem as a conventional Landau’s order parameter which also changes its values during the phase transition. However, they are very different. Landau’s order parameter is used to describe a phase transition which is associated with the spontaneous symmetry breaking (SSB), whereas a topological phase transition does not accompany SSB.

The construction of such a *topological invariant* is based on the underlying local symmetry constraints on the bulk Hamiltonian. Local symmetries like time-reversal (anti-unitary), particle-hole (anti-unitary), and chiral operators (unitary) impose the following set of constraints on the Hamiltonian respectively.

$$\Theta\mathcal{H}(-k_x, -k_y, -k_z)\Theta^{-1} = \mathcal{H}(k_x, k_y, k_z), \quad \Theta^2 = \pm 1 \quad (1.1)$$

$$\Xi\mathcal{H}(-k_x, -k_y, -k_z)\Xi^{-1} = -\mathcal{H}(k_x, k_y, k_z), \quad \Xi^2 = \pm 1 \quad (1.2)$$

$$\Pi\mathcal{H}(k_x, k_y, k_z)\Pi^{-1} = -\mathcal{H}(k_x, k_y, k_z), \quad \Pi^2 = 1. \quad (1.3)$$

Θ , Ξ , and Π are the time-reversal, particle-hole and chiral operators, respectively. \mathcal{H} denotes the Hamiltonian of a system which is a function of momenta k_x , k_y , and k_z . For a concrete picture, topological insulators which are classified based on the above three local symmetries fall in the tenfold way symmetry class [12, 13].

Symmetry				d							
AZ	Θ^2	Ξ^2	Π^2	1	2	3	4	5	6	7	8
A	0	0	0	0	\mathbb{Z}	0	\mathbb{Z}	0	\mathbb{Z}	0	\mathbb{Z}
AIII	0	0	1	\mathbb{Z}	0	\mathbb{Z}	0	\mathbb{Z}	0	\mathbb{Z}	0
AI	1	0	0	0	0	0	\mathbb{Z}	0	\mathbb{Z}_2	\mathbb{Z}_2	\mathbb{Z}
BDI	1	1	1	\mathbb{Z}	0	0	0	\mathbb{Z}	0	\mathbb{Z}_2	\mathbb{Z}_2
D	0	1	0	\mathbb{Z}_2	\mathbb{Z}	0	0	0	\mathbb{Z}	0	\mathbb{Z}_2
DIII	-1	1	1	\mathbb{Z}_2	\mathbb{Z}_2	\mathbb{Z}	0	0	0	\mathbb{Z}	0
AII	-1	0	0	0	\mathbb{Z}_2	\mathbb{Z}_2	\mathbb{Z}	0	0	0	\mathbb{Z}
CII	-1	-1	1	\mathbb{Z}	0	\mathbb{Z}_2	\mathbb{Z}_2	\mathbb{Z}	0	0	0
C	0	-1	0	0	\mathbb{Z}	0	\mathbb{Z}_2	\mathbb{Z}_2	\mathbb{Z}	0	0
CI	1	-1	1	0	0	\mathbb{Z}	0	\mathbb{Z}_2	\mathbb{Z}_2	\mathbb{Z}	0

Fig. 1.1 The periodic table (Altland-Zirnbauer classification) for non-interacting topological insulators based on three elementary local symmetries (Θ , Ξ , Π) of the Hamiltonian in different spatial dimensions d . The table is periodic in nature with $d = 8$, known as Bott periodicity. Systems characterized by \mathbb{Z}_2 group as topological invariant indicate only two possible elements 0, 1, with 0 denoting a trivial and 1 denoting a non-trivial topological phase. On the other hand, \mathbb{Z} denotes an integer number which can take any values indicating arbitrary number of anomalous boundary modes in the case $\mathbb{Z} \neq 0$.

However, after the discovery of topological non-trivial phases protected by crystalline symmetries, further works have classified topological systems [14–16] which go beyond the classification table (1.1).

Before delving into the thesis work, I would like to introduce some relevant topics and its concepts which would set some theoretical background.

1.2 Berry connection and Berry curvature

It is well known that electrons in a crystal under periodic potential follow Bloch's theorem [17, 18]. If one writes down the Schrödinger's equation for the electrons in a periodic crystal which reads

$$\left(-\frac{1}{2m} \nabla^2 + \hat{V}(\mathbf{r}) \right) |\Psi\rangle = E |\Psi\rangle, \quad (1.4)$$

where $\hbar = 1$, ∇^2 , $\hat{V}(\mathbf{r})$, m and E are the kinetic energy term, potential energy term, mass and energy of the electron, the solution will be the Bloch states,

$$|\Psi_{n,\mathbf{k}}(\mathbf{r})\rangle = |u_{n,\mathbf{k}}(\mathbf{r})\rangle e^{i\mathbf{k}\cdot\mathbf{r}}. \quad (1.5)$$

In Eq (1.5), $u_{n,\mathbf{k}}(\mathbf{r} + \mathbf{a}) = u_{n,\mathbf{k}}(\mathbf{r})$ is a periodic function, defined by the periodicity (a) of the crystal. Note that each Bloch wave has an usual plane wave part ($e^{i\mathbf{k}\cdot\mathbf{r}}$) multiplied with a periodic function. Moreover, each Bloch state is characterized by n, \mathbf{k} , known as band number and crystal momentum, respectively. Here, crystal momentum \mathbf{k} is restricted to the Brillouin zone, which is periodic because of the lattice translation symmetry.

Earlier, it was understood that any extra phase appearing in $|\Psi_{n,\mathbf{k}}(\mathbf{r})\rangle$ does not change any physics as the phase drops off while calculating any physically measurable quantity. However, below we will see that the geometric nature of such Bloch state can give rise to another interesting phase in solids, called Berry phase [19]. Even though the discussion below will be considered for any general quantum mechanical wavefunction $|\Psi\rangle$, for periodic solids, such states will be a function of band number (n) and crystal momentum (\mathbf{k}).

Let us assume that we have a quantum mechanical system which exists in its non-degenerate ground state, and the Hamiltonian of the system is changed very slowly, so that it remains in its ground state for such a variation. This so called slow change in the Hamiltonian is dubbed as *quantum adiabatic evolution*.

For a detailed description of the origin of Berry connection and Berry curvature, we will closely follow the notation used in this review article [20]. We consider a system for which the Hamiltonian is a function of some parameters $\mathbf{R} = (R_1, R_2, R_3 \dots)$. Now the system follows $H(R) |n(\mathbf{R})\rangle = \varepsilon_n |n(\mathbf{R})\rangle$, where the initial eigenstate is denoted by $|n(\mathbf{R})\rangle$. The Hamiltonian then is *adiabatically* evolved to time t upon varying the parameters \mathbf{R} . During the evolution,

the initial eigenstate still remains an eigenstate of the time evolved Hamiltonian $H(\mathbf{R}(t))$ upto an arbitrary phase. The general expression for the time evolved state can be written as follows:

$$|\Psi_n(t)\rangle = e^{i\gamma_n(t)} e^{-i\int_0^t dt' \varepsilon_n(\mathbf{R}(t'))} |n(\mathbf{R}(t))\rangle \quad (1.6)$$

Eq (1.6) contains two phase factors. The second phase factor is the well known dynamical phase which appears with the energy ε_n . The first phase $\gamma_n(t)$ is the geometric phase (also known as Berry phase), which can be explicitly determined after solving the time dependent Schrödinger's equation

$$i \frac{\partial}{\partial t} |\Psi_n(t)\rangle = H(\mathbf{R}(t)) |\Psi_n(t)\rangle, \quad (1.7)$$

by putting the wavefunction $|\Psi_n(t)\rangle$.

The explicit expression of the geometric phase looks like $\gamma_n = \int_C d\mathbf{R} \cdot \mathcal{A}_n(\mathbf{R})$. Notice that in order to obtain the form γ_n , one needs to perform the integral along a closed path C in the parameter space, when \mathbf{R} changes along that closed contour. The form of $\mathcal{A}_n(\mathbf{R})$ reads;

$$\mathcal{A}_n(\mathbf{R}) = i \langle n(\mathbf{R}) | \frac{\partial}{\partial \mathbf{R}} |n(\mathbf{R})\rangle. \quad (1.8)$$

In Eq (1.8), $\mathcal{A}_n(\mathbf{R})$ is a vector which is called the Berry connection. $\frac{\partial}{\partial \mathbf{R}}$ is the partial derivative with respect to the parameter which is varied, for instance in a periodic lattice, momentum k can be chosen as a parameter which forms a closed Brillouin zone. Note that, Berry connection is a gauge dependent quantity (usually resides on momentum space for periodic solids), and hence bears no physical significance. In electrodynamics, this is similar to the vector potential \vec{A} .

In electrodynamics, the magnetic field \mathbf{B} is obtained by taking the curl of \vec{A} . Analogously, even though the Berry connection is not a physical quantity, one can define a physical quantity in momentum space by taking its curl, known as Berry curvature

$$\Omega_n(\mathbf{R}) = \nabla_{\mathbf{R}} \times \mathcal{A}_n(\mathbf{R}). \quad (1.9)$$

In its compact form, in terms of the summation of the eigenstate Berry curvature takes the following form:

$$\Omega_{\mu\nu}^n(\mathbf{R}) = i \sum_{n' \neq n} \frac{\langle n | \frac{\partial H}{\partial R^\mu} | n' \rangle \langle n' | \frac{\partial H}{\partial R^\nu} | n \rangle - (\nu \leftrightarrow \mu)}{(\varepsilon_n - \varepsilon_{n'})^2}, \quad (1.10)$$

where $\varepsilon_n, \varepsilon_{n'}$ are the corresponding energies of the eigenstates $|n\rangle, |n'\rangle$ respectively.

In the context of two dimensional topological insulators, integration of the Berry curvature over the whole Brillouin zone usually gives rise to topological invariant called the Chern number.

1.3 Quantum Hall effect

In this section, we will go through the discovery of integer Quantum Hall effect (IQHE) [1] which laid the foundational stone in this field of topology. For this discovery Klaus von Klitzing was awarded the 1985 Nobel prize in physics. He observed that electrons in two dimensions subject to a low temperature (1.5K) and a strong magnetic field (15T) show step like (quantized) features in the transverse conductivity. This transverse conductivity also known as Hall conductivity reads as

$$\sigma_{xy} = C \frac{e^2}{h}, \quad C \in \mathbb{Z}, \quad (1.11)$$

where, e is the electron's charge, and h is Planck's constant, respectively.

Let us review the theory behind the origin of the quantized conductivity. The Two dimensional free electron gas (2DEG) has a parabolic dispersion relation $\mathcal{H} = \frac{\hat{\mathbf{p}}^2}{2m}$, where \mathbf{p} , and m are the momentum and mass of the electrons, respectively. Now, in presence of a magnetic field $B\hat{\mathbf{z}}$ applied perpendicular to the xy plane, the dispersion relation is modified by the canonical momentum (known as minimal coupling method) as

$$\mathcal{H} = \frac{1}{2m}(\mathbf{p} + e\mathbf{A})^2. \quad (1.12)$$

In (1.12), \mathbf{A} is the vector potential with $\nabla \times \mathbf{A} = B\hat{\mathbf{z}}$. For further calculation let us choose the Landau gauge $\mathbf{A} = xB\hat{\mathbf{y}}$ for the vector potential. With this gauge choice, the Hamiltonian now can be written down as

$$\mathcal{H} = \frac{1}{2m}\hat{p}_x^2 + \frac{1}{2m}(\hat{p}_y + eBx)^2, \quad (1.13)$$

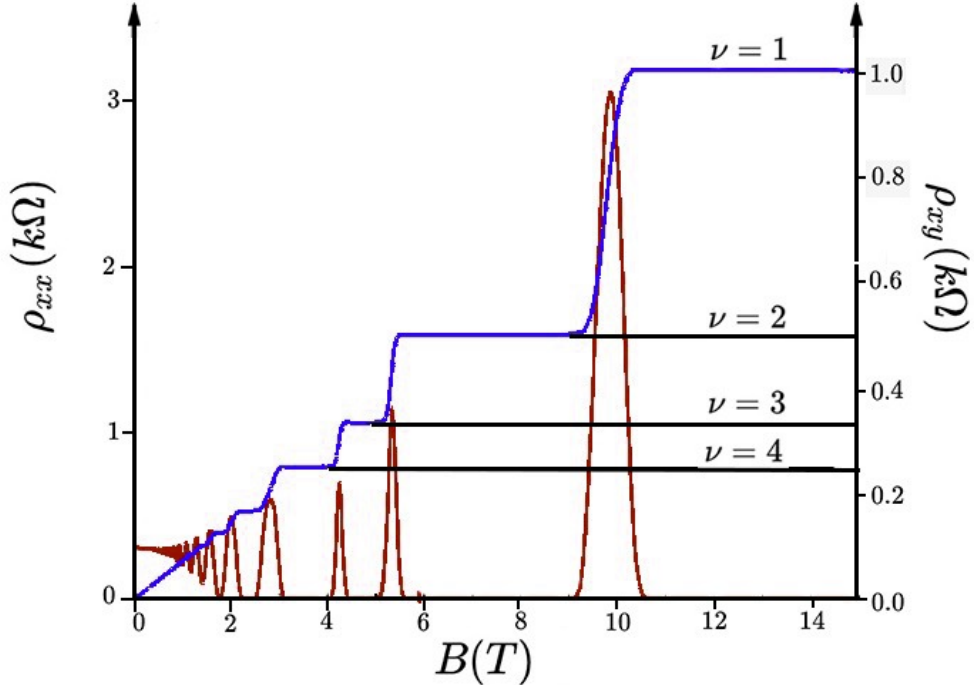


Fig. 1.2 The figure depicts how transverse Hall resistivity ρ_{xy} (blue line) and longitudinal resistivity ρ_{xx} (red line) vary with the applied magnetic field B . Quantized plateaus in ρ_{xy} appear whenever ρ_{xx} goes to zero. Quantized numbers $\nu = 1, 2, 3, 4$ in the figure correspond to Chern number C (in our convention (1.11)). Figure is taken from wikipedia [21].

Noticeably, as \mathbf{A} does not contain any component with position operator y , the corresponding momentum \hat{p}_y is a good quantum number, and hence commutes with the Hamiltonian eq (1.13). This commutation allows us to write down a simplified ansatz for the eigenstate of eq (1.13) as

$$\Psi_{p_y}(x, y) = e^{ip_y y} f_{p_y}(x). \quad (1.14)$$

Note that the ansatz (1.14) contains a plane wave part $e^{ip_y y}$ coming from the free dispersion nature along y . Further, we can simplify the Hamiltonian by introducing the cyclotron frequency $\omega_c = \frac{eB}{m}$, and a magnetic length scale $l_B = \sqrt{\frac{1}{eB}}$. We have been working with the theorist's convention of unit, so wherever \hbar appears, we set it to unity. On simplification, the Hamiltonian of the system now reads

$$\mathcal{H}_{p_y} = \frac{\hat{p}_x^2}{2m} + \frac{m\omega_c^2}{2}(x + p_y l_B^2)^2. \quad (1.15)$$

With the analogous nature of the quantum one dimensional harmonic oscillator Hamiltonian, we can note that the potential part is shifted from origin $x_0 = 0$ to $x_0 = -p_y l_B^2$. But this shift does not change any physics, and hence the energy levels emulate the harmonic oscillator energy levels;

$$E_n = \omega_c \left(n + \frac{1}{2} \right), \quad n \in \mathbb{N} \quad (1.16)$$

where, the quantized energy levels are called Landau levels. Notice that, the Landau levels are proportional to the cyclotron frequency ω_c , which in turn implies that as one increases the magnetic field, the energy of the Landau level increases. One important point to note here is that energies of the Landau levels being not dependent on p_y , they have large degeneracies.

Now the question is why we see IQHE in this 2DEG system at large magnetic field with low temperature? Firstly, the effects of Landau levels come into picture when the electrons which occupy them have much lower thermal energy than the energy limit set by its cyclotron frequency, meaning $k_B T \ll \omega_c$.

What happens with increasing the magnetic field is that, many electrons can occupy the Landau levels. Simple calculation dictates that the number of states per energy level takes the form

$$N = \frac{eBA}{\frac{2\pi}{\Phi}} = \frac{eBA}{\frac{\Phi}{\Phi_0}}, \quad (1.17)$$

where $\Phi_0 = \frac{2\pi}{e}$ is called flux quantum ($= 1$), and Φ is total flux penetrating through the 2DEG system with area A . So, the flux through the system is the measure of number of filled states per Landau level. In the IQH fig (1.2), the alternate plateau and jump in the resistance indicate that, initially the Fermi level which was lying in between two Landau levels (plateau), now crosses one of the levels (jump). This jump between Landau levels has a very deep consequences on the system's transport in terms of its edge and bulk physics.

1.3.1 Bulk-Edge picture and Chern number

In 2DEG, usually upon application of magnetic field, electrons form cyclotron orbits inside the bulk of the sample, whereas at the edges of the sample, electrons can only complete half of circular motion, forming the so called *skipping* orbits.

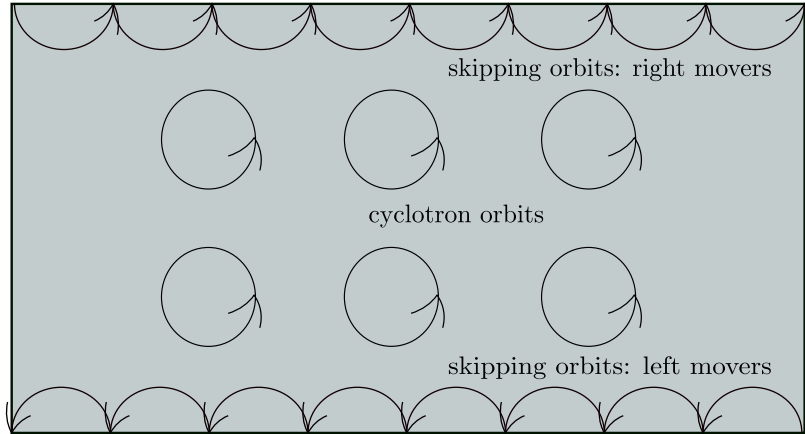


Fig. 1.3 Formation of the cyclotron orbits in the bulk, and skipping orbits at the edge of the system is shown. Magnetic field is applied perpendicular to the plane, and it gives rise to an anti-clockwise motion of the electrons. It is seen that at the upper edge of the sample, while electrons perform half of the orbital motion in the right direction, at the bottom edge they will do the same but in the opposite (left) direction. This happens so that the net current is conserved, giving rise to edge current at the boundaries of the sample.

This skipping motion of electrons at the edge of the sample gives rise to a propagating *edge* state in the system. The fascinating fact is, the *edge* modes are quantized in number and they are very robust against any perturbation.

Until 1982, there was no theory which explained this phenomenon. Thouless, Kohmoto, Nightingale, and Nijs (TKNN) gave the formula [3], which introduced how to determine the number of such edge states in the system. They basically constructed the formula for transverse Hall conductivity from the linear response theory

$$\sigma_{xy} = \frac{e^2}{2\pi h} \iint_{BZ} d^2\mathbf{k} \Omega(\mathbf{k}) \quad (1.18)$$

The integral is performed over a closed Brillouin zone formed by $d^2\mathbf{k}$ in momentum space. $\Omega(\mathbf{k})$ is the Berry curvature which we have discussed in the previous section. For reminder, it is defined as;

$$\Omega(\mathbf{k}) = \partial_{k_x} A_y - \partial_{k_y} A_x. \quad (1.19)$$

Upon comparing with eq (1.11) and eq (1.18), we can define the so called topological invariant dubbed as *Chern* number for IQHE

$$C = \frac{1}{2\pi} \iint_{BZ} d^2\mathbf{k} \Omega(\mathbf{k}), \quad C \in \mathbb{Z}. \quad (1.20)$$

Interestingly, the Chern number reflects the count of chiral edge states present in the system.

1.4 Quantum spin Hall effect: two dimensional (2D) time-reversal invariant topological insulators

From the earlier section on QHE in 2DEG, we have seen that in order to realize robust dissipationless boundary transport, one needs to apply an external magnetic field. However, in 1988 Haldane showed that there can exist quantized Hall conductance even in absence of the applied magnetic field. This phenomenon is known as *Quantum anomalous Hall effect* (QAHE) [4]. Essentially, what he suggested is that, magnetic field is not the only key ingredient for realizing a topological phase. Rather, if one could break time-reversal symmetry (TRS) without applying such a magnetic field, it can still in principle be possible to realize nonzero Hall conductance. In Haldane's model, the TRS breaking perturbation was generated by the flux inside each plaquette in the hexagonal graphene.

The importance of TRS breaking can be clearly understood by studying the nature of Berry curvature (BC). Earlier we have seen that Chern number (C) is obtained by integrating out the BC over the whole Brillouin zone, which gives rise to nontrivial topology (if only $C \neq 0$). Under TRS, BC changes its sign, meaning it is odd.

$$\Theta \Omega(k_x, k_y) \Theta^{-1} = -\Omega(-k_x, -k_y) \quad (1.21)$$

where, Θ (anti-unitary) is the TRS operator defined generally as $\Theta = \mathcal{U}\mathcal{K}$. Here, \mathcal{U} denotes the unitary part and \mathcal{K} is the complex conjugation. k_x, k_y are the momentum components. Naturally, BC being an odd function, the integration of BC performed over the Brillouin zone vanishes, resulting in net zero C . Hence, the system cannot show any nontrivial topology unless TRS is broken.

So until now, we discussed that to realize any non-trivial topological phases, we would need to break TRS. Although this discovery enriched the field as far as theoretical model is concerned, it became experimentally challenging to find real

materials which show QAHE. It is worth mentioning that the first experimental observation of QAHE phenomena was reported recently in 2013 [22], where thin films of chromium-doped $(\text{Bi},\text{Sb})_2\text{Te}_3$ exhibited quantized Hall response at zero external magnetic field.

A significant revival of interest in topology came with the discovery of quantum spin Hall effect (QSHE) in Graphene (2004). In these works [23, 24], Kane and Mele showed that a monolayer graphene can host topological properties in presence of spin-orbit coupling (SOC), which preserves TRS. Specifically, they proposed to realize a pair of *spin polarized* counter-propagating edge states at each edge of the two dimensional system. TRS maps one *spin momentum locked* edge state $|\Psi(\mathbf{k}, \uparrow)\rangle$ to its Kramers' partner $|\Psi(-\mathbf{k}, \downarrow)\rangle$, and they are robust to any TRS preserving perturbation.

QSHE opened up a new avenue in terms of realizing topological insulators in the lab as far as real materials are concerned. Graphene being made of lighter carbon atoms, it does not have strong SOC, hence it was hard to observe QSHE in graphene as originally proposed. Soon after, 2D-TRS invariant TI phase was observed in CdTe/HgTe quantum wells [25–27] which have stronger SOC driven band inversion. Remarkably, quantized spin Hall conductance of $\frac{2e^2}{h}$ was observed, which is 2 times more (because of spin degeneracy) than that of the QHE response. Since then, one of the key goals is to realize large band gap QSH materials and significant number of discoveries has been made in this direction experimentally [28–34].

In the rest of this section, we will discuss more about QSHE physics in the context of graphene, and define the topological invariant which classifies the nontrivial phase. We start with the Kane-Mele Hamiltonian which reads

$$\mathcal{H} = \sum_{\langle ij \rangle, \alpha} t c_{i,\alpha}^\dagger c_{j,\alpha} + \sum_{\langle\langle ij \rangle\rangle, \alpha\beta} it_2 \nu_{ij} s_{\alpha\beta}^z c_{i,\alpha}^\dagger c_{j,\beta}, \quad (1.22)$$

where the first and second term represent the usual nearest neighbor hopping and the next nearest neighbor hopping. t, t_2 are the strength of those hoppings, respectively. $\nu_{ij} = \frac{2}{\sqrt{3}}(\hat{\mathbf{d}}_1 \times \hat{\mathbf{d}}_2)_z = \pm 1$ depending on if an electron makes a left (right) turn to reach to the second nearest neighbor. $\hat{\mathbf{d}}_1, \hat{\mathbf{d}}_2$ are the unit vectors of the two consecutive bonds which electron traverses in going from site j to i . The spin dependent second neighbor term is considered to take into account the SOC, giving rise to a SOC driven topological bulk band gap. Furthermore, the

system in the strip geometry shows *helical* edge states living at both edges of the system.

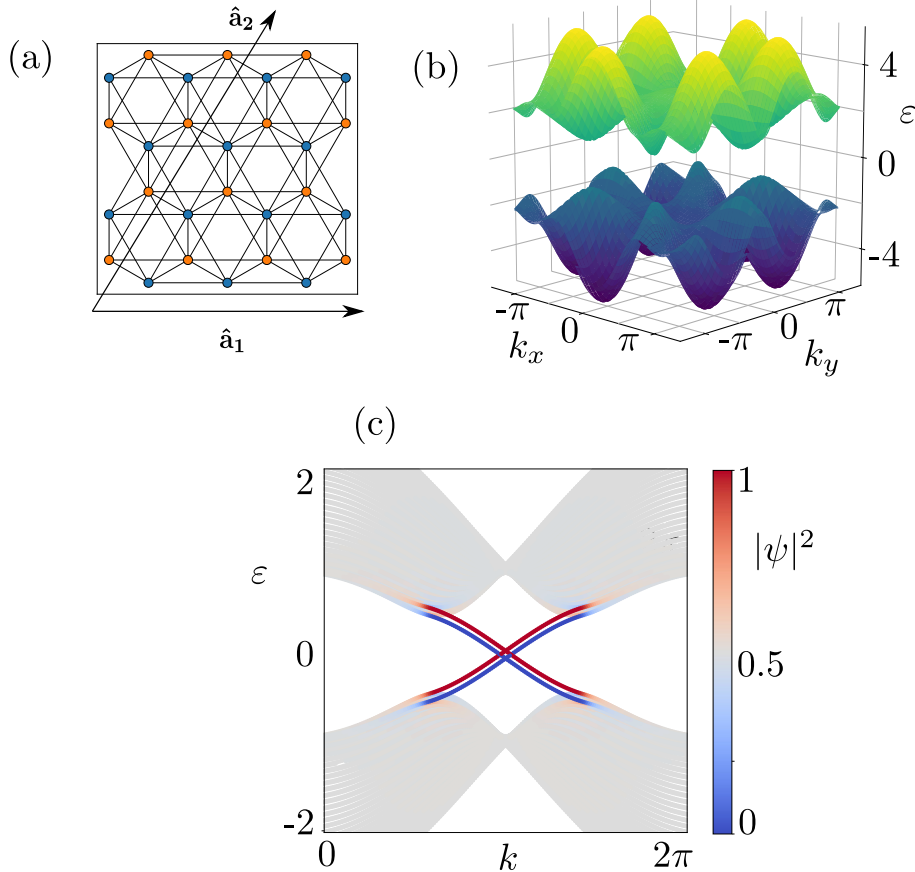


Fig. 1.4 (a) Graphene with nearest and next-nearest neighbor hopping. $\hat{a}_1 = (1, 0)$, $\hat{a}_2 = (\frac{1}{2}, \frac{\sqrt{3}}{2})$ are the Bravais lattice vectors. Different sub-lattice(s) in the unit cell of graphene is indicated by blue and orange colors respectively. (b) Gapped bulk bandstructure of graphene with Kane-Mele Hamiltonian [24]. In presence of the second nearest neighbor term, bulk Dirac cones get gapped. (c) Bandstructure in the slab geometry is shown for $W = 60$ unit cells finite along the \hat{a}_2 -direction. Parameters taken as $t = 1$, $t_2 = 0.15$, $\lambda_v = 0.1$. energy ε , and momentum k are measured in the unit of t , and $1/a_1$ respectively. λ_v is the staggered sub-lattice potential (λ_v). Gapless spin-polarized helical edge states are depicted, i.e. at each edge of the system, there is counter-propagating edge states corresponding to spin up and spin down channel.

1.4.1 \mathbb{Z}_2 topological invariant

In table 1.1, TRS symmetry protected 2D topological systems fall into the class AII with topological invariant defined as \mathbb{Z}_2 . Let us proceed to understand how one can define such \mathbb{Z}_2 invariant. For this purpose we will very briefly review the concept of *time-reversal polarization* established by Fu, Kane [35, 36], which is at the core of defining the topological invariants in these systems (both 2D and 3D).

Following Kramers' theorem, in presence of TRS (only for spinful fermions, $\Theta^2 = -1$), each state will have its Kramers' partner with same energy but opposite momentum $-\mathbf{k}$, i.e., state defined as $|u(\mathbf{k})\rangle$ will be degenerate with $|u(-\mathbf{k})\rangle$. This demands that any TRS invariant system will have even ($2N$) number of bands where, N denotes the number of pairs of eigenstates.

Unlike the usual charge polarization which is defined by the sum of the Wannier centers of all of the bands, Fu and Kane proposed (for TRS invariant systems), it is enough to keep track of the center of one of the Kramers' degenerate Wannier state by defining a quantity called partial polarization. The $2N$ set of eigenstates with N pairs satisfy

$$|u_{-\mathbf{k},\alpha}^I\rangle = -e^{i\chi_{\mathbf{k},\alpha}}\Theta|u_{\mathbf{k},\alpha}^{II}\rangle \quad (1.23)$$

$$|u_{-\mathbf{k},\alpha}^{II}\rangle = e^{i\chi_{-\mathbf{k},\alpha}}\Theta|u_{\mathbf{k},\alpha}^I\rangle, \quad (1.24)$$

where $\alpha = 1, \dots, N$, and I,II denote the two set(s) of eigenstate connected by Kramers' theorem. $\chi_{\mathbf{k},-\mathbf{k}}$ are smooth functions. With this, the partial polarization corresponding to one of the sets $s=I$ or II can be written as

$$P^s = \frac{1}{2\pi} \int_{-\pi}^{\pi} d\mathbf{k} \mathcal{A}^s(\mathbf{k}), \quad (1.25)$$

where the quantity

$$\mathcal{A}^s(\mathbf{k}) = i \sum_{\alpha} \langle u_{\mathbf{k},\alpha}^s | \nabla_{\mathbf{k}} | u_{\mathbf{k},\alpha}^s \rangle \quad (1.26)$$

is called the Berry connection. Notice that, partial polarization (1.25) for each set s is not a gauge invariant quantity as it changes with integer multiple of lattice constants under a general $U(2N)$ gauge transformation. However, the difference of partial polarization for two sets defines a physical quantity (only in presence of TRS), termed as time-reversal polarization. This reads

$$P_\theta = P^I - P^{II}. \quad (1.27)$$

The above quantity P_θ is defined modulo an integer. If we skip some of the algebraic steps mentioned in [35], Fu-Kane obtained the following relation

$$(-1)^{P_\theta} = \frac{\sqrt{\det[\omega(0)]}}{Pf[\omega(0)]} \frac{\sqrt{\det[\omega(\pi)]}}{Pf[\omega(\pi)]}. \quad (1.28)$$

In eq (1.28), $Pf[\omega]$ is called Pfaffian. Pfaffian of an anti-symmetric matrix ω has the property $\det[\omega] = Pf[\omega]^2$. ω is a $U(2N)$ matrix. More generally, ω is called sewing matrix, which in presence of TRS reads

$$\omega_{\alpha\beta}(\mathbf{k}) = \langle u_{-\mathbf{k}\alpha} | \Theta | u_{\mathbf{k},\beta} \rangle. \quad (1.29)$$

Proceeding further, Fu-Kane defined the \mathbb{Z}_2 invariant ν as

$$(-1)^\nu = \prod_{i=1}^4 \frac{\sqrt{\det[\omega(\Gamma_i)]}}{Pf[\omega(\Gamma_i)]} \quad (1.30)$$

Notice that the product runs over four time-reversal invariant momentum (TRIM) points (Γ_i) in the 2D Brillouin zone (BZ), namely for $(0, 0)$, $(\pi, 0)$, $(0, \pi)$, (π, π) . $\nu = 1$ in this case corresponds to a 2D-QSHI phase.

The generalization of QSHI in three dimensions (3D) gives rise to so called *strong* and *weak* topological phases. Correspondingly, the topological invariant was further extended by Fu-Kane-Mele [37]. In this case (3D), four \mathbb{Z}_2 indices $(\nu_0; \nu_1, \nu_2, \nu_3)$ classify the topological phases, with nonzero ν_0 representing a strong topological insulating phase (STI), and the other nonzero values of (ν_1, ν_2, ν_3) represent weak topological insulating phase (WTI).

In 3D we have eight TRIM points which can be denoted by the reciprocal lattice vectors \mathbf{b}_i ,

$$\Gamma_{i=(n_1, n_2, n_3)} = \frac{1}{2}(n_1\mathbf{b}_1 + n_2\mathbf{b}_2 + n_3\mathbf{b}_3) \quad (1.31)$$

with $n_j \in \{0, 1\}$.

The main idea here is to define \mathbb{Z}_2 index for each of the 2D surfaces in the 3D BZ. For each of this plane, we require four TRIM points to write down the

\mathbb{Z}_2 index ν as

$$(-1)^\nu = \prod_{i=1}^4 \delta_i, \quad \delta_i = \frac{\sqrt{\det[\omega(\Gamma_i)]}}{Pf[\omega(\Gamma_i)]} \quad (1.32)$$

Now, with this Fu-Kane-Mele strong and weak topological invariants read

$$(-1)^{\nu_0} = \prod_{n_j=0,1} \delta_{n_1, n_2, n_3} \quad (1.33)$$

$$(-1)^{\nu_{i=1,2,3}} = \prod_{n_i=1, n_j \neq i=0,1} \delta_{n_1, n_2, n_3} \quad (1.34)$$

where there could only be four independent \mathbb{Z}_2 invariants. Note that, δ_{n_1, n_2, n_3} is a topological number quantized to -1 or 1 .

In the case of strong \mathbb{Z}_2 index being nontrivial ($\nu_0 = 1$), one expects to realize odd number of in-gap surface states which connect the valence and conduction band. Importantly, the observation of these states is independent of the choice of the surface, meaning that choosing any surface termination for a real material which is a STI will inevitably show these states. On the other hand, if the strong invariant is trivial ($\nu_0 = 1$), but the weak invariant is nontrivial ($\nu_i \neq 0$), we expect to see even number of in-gap states in the bulk gap. These WTI states are not robust against any lattice translational symmetry breaking perturbation.

1.5 Topological Crystalline Insulators (TCI)

From our previous discussions, we have seen that QHE required breaking of TRS. On the other hand, QSH is only realized in TRS preserving SOC systems, which give rise to bulk band inversion. And most of the materials showing the nontrivial topological phases were classified using the tenfold symmetry classification table given by Altland-Zirnbauer. However, this classification required further modifications after Fu proposed to realize topological phases which are protected by crystalline symmetries [38, 39]. The class of materials showing this nontrivial phase are dubbed as *topological crystalline insulators* (TCI) [40, 41]. Crystalline symmetries in lattice being ubiquitous, this opened up a whole new platform to discover topological insulators.

In the seminal work [40], Fu predicted a 3D tight-binding model which realizes gapless surface states protected by a C_4 rotational symmetry in combination with TRS. Specifically, he showed that the surface (001) which preserves C_4 symmetry exhibits the gapless surface states. And it is in fact true with TCI sys-

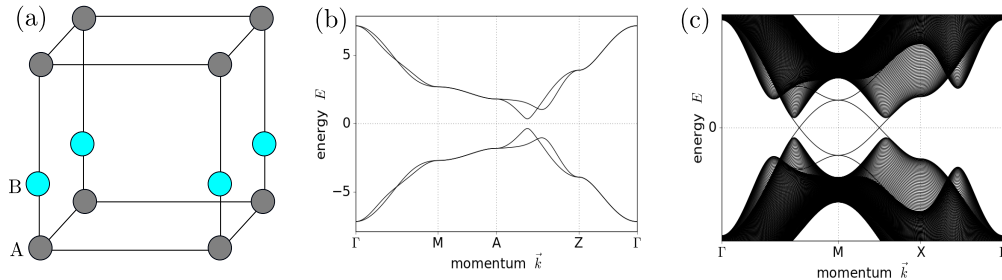


Fig. 1.5 (a) Tetragonal lattice structure with two atoms A and B in the unit cell. (b) Bulk bandstructure for the Hamiltonian as mentioned in Eq. (2) of [40]. It can be seen that the bulk spectrum is gapped everywhere in the BZ. (c) Slab bandstructure for (001) surface shows the existence of topologically protected gapless states. The gapless surface states originating from the C_4 crystalline symmetry are quadratic in nature.

tems, meaning only those surfaces which preserve the crystalline symmetry will show gapless states. From this feature, one can immediately draw a distinction between a STI and a TCI, as in the case of a STI, all surfaces will carry gapless states unlike TCI. Soon after the proposal of Fu's theoretical model, experimental realizations were made for SnTe material [42, 43]. This 3D rock-salt crystal hosts as a pair of stable gapless surface states, where the mirror invariant plane lies. Hence, SnTe was classified as mirror symmetry protected TCI. To calculate the invariant for a mirror TCI, one defines a so called *mirror Chern number* (MCN). We briefly discuss this below.

The main idea behind defining a MCN is to decompose the Hilbert space into the mirror invariant sectors. This is possible because a surface in the BZ can be left invariant under mirror operation as shown in Fig 1.6, where mirror operation M_y leaves the planes $k_y = 0$ and $k_y = \pi$ invariant [44]. Such mirror invariant sectors are further defined by the mirror eigenvalues. For instance, a 3D spinful system with mirror eigenvalues $+i$ and $-i$, can be decomposed into two mirror ($\pm i$) sub-spaces. Basically, now the Bloch Hamiltonian of the full system can be written in block forms, where each block corresponds to mirror eigenvalues $\pm i$, respectively. Following this, one can define a Chern number ($C_{\pm i}$) for each of the blocks, and then the difference in $C_{\pm i}$ between the two blocks gives rise to MCN, which reads

$$C_M = \frac{C_{+i} - C_{-i}}{2}. \quad (1.35)$$

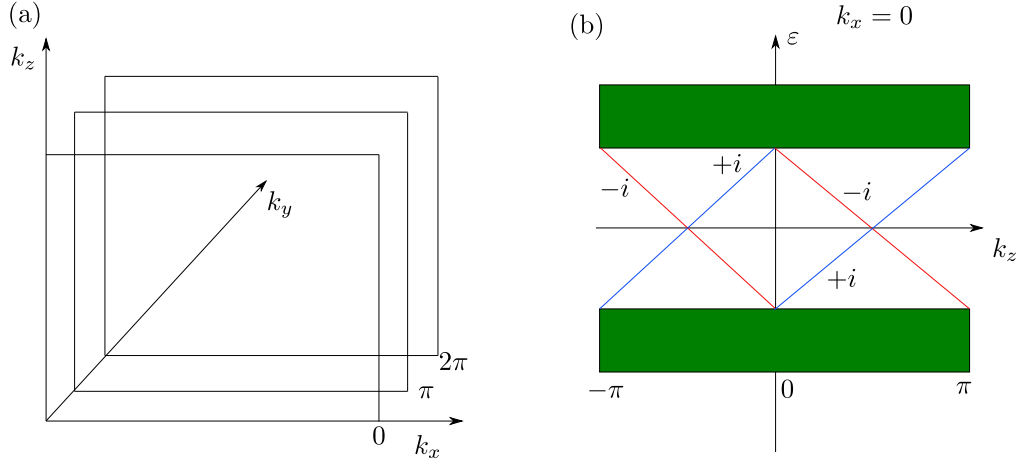


Fig. 1.6 (a) Schematic BZ for a topological crystalline insulator with mirror symmetry M_y . Due to M_y , there are two planes in the surface BZ which are left invariant, namely $k_y = 0, \pi$. (b) Schematic surface band structure (along $k_x = 0$ cut) with two chiral edge states for each mirror invariant plane.

The topological invariant C_M denotes the number of gapless surface states in the system. For SnTe, $C_M = -2$ corresponds to two topologically protected Dirac cones. Discovery of TCI has impacted the field of topological insulator immensely in terms of material search [45–48]. Very recently, there have been significant works which classify band structure topology of all 233 space groups, and 1651 magnetic space groups [49–51].

1.6 This thesis

This thesis mostly deals with the realization of non-interacting topological phases in both realistic and toy model scenarios. In particular, it focuses on exploring the TCI phases. There have been prior theoretical works in the literature concerning the TCIs based on layered setups [52, 53]. Along this route, the dissertation first uncovers that one can attain such a TCI phase in stacked graphene system under certain conditions. Furthermore, it investigates that in 3D, a naturally occurring mineral called Jacutingaite (Pt_2HgSe_3) is expected to show both TCI and WTI phases. Both Density Functional Theory (DFT) and minimal tight-binding calculations are performed to capture the topological phases. In this direction, we proposed a new tight-binding model to capture the dual topological nature of materials. Following this, the thesis will aim at understanding the topological phases, appearing for two cubic 3D half-Heusler materials ($\text{LiBiZn}, \text{LiSbZn}$) belonging to the space group 216. In this context, higher order topology has been explored in these systems. Finally, the thesis presents a flavor of newly discovered topological transport phenomena, namely Magnus Hall effect in two and three dimensional systems. Effects of strain, warping, and tilt on response have been explored in detail.

1.6.1 Outline of the chapters

Here we present the brief outline of the rest of the chapters presented in this thesis.

1.6.2 Chapter2

In principle the stacking of different 2D materials allows the construction of 3D systems with entirely new electronic properties. In this chapter, we will study how one can realize topological crystalline insulators (TCI) protected by mirror symmetry in heterostructures consisting of graphene monolayers separated by two-dimensional polar spacers. The polar spacers are arranged such that they can induce an alternating doping and/or spin-orbit coupling in the adjacent graphene sheets. When spin-orbit coupling dominates, the non-trivial phase arises due to the fact that each graphene sheet enters a quantum spin-Hall phase. Instead, when the graphene layers are electron and hole doped in an alternating fashion, a uniform magnetic field leads to the formation of quantum Hall phases with

opposite Chern numbers. Thus we realize that it has the remarkable property that unlike previously proposed and observed TCIs, the non-trivial topology is generated by an external time-reversal breaking perturbation.

1.6.3 Chapter3

Using two dimensional (2D) TI layers as building blocks, there have been numerous works done to obtain novel topological phases. Most of these quasi-two-dimensional systems realize weak topological phases in presence of translation symmetry along the stacking direction of the 2D TIs. However, recently it has been found that topological phases of electronic systems often coexist in a material, well-known examples being systems which are both strong and weak topological insulators. More recently, a number of materials have been found to have the topological structure of both a weak topological phase and a mirror-protected topological crystalline phase.

In this chapter, we first focus on the naturally occurring mineral called Jacutingaite (Pt_2HgSe_3), and show based on density-functional calculations that it realizes this dual topological phase and that the same conclusion holds for Pd_2HgSe_3 . What makes this layered system more interesting is the fact that monolayer version of Jacutingaite is predicted to have a sizable band gap of 0.5eV, featuring a novel quantum spin Hall insulator.

Further, we introduce tight-binding models that capture the essential topological properties of this dual topological phase in materials with three-fold rotation symmetry and use these models to describe the main features of the surface spectral density of different materials in the class.

In this work, my contribution was to come up with the tight-binding model which captures the topological features observed in these minerals. DFT calculations were mainly performed by my collaborator Jorge Facio.

1.6.4 Chapter4

In search of further interesting topological phases, we go beyond quasi-two-dimensional system and, pay our attention to a 3D cubic half-Heusler system, which realizes different topology under strain.

Half-Heusler compounds are a material class with a large potential for the study of distinct electronic states. In this chapter, we investigate from first-principles the possibility of hinge modes in very proximate topological phases

tunable by moderate uniaxial strain. We consider the compounds LiSbZn and LiBiZn. While LiSbZn has a topologically trivial band structure, the larger spin-orbit coupling of Bi causes a band inversion in LiBiZn.

We predict the existence of topologically trivial hinge states in both cases. The hinge modes are affected by the bulk topological phase transitions, but in an indirect way: topological surface modes, when present, hybridize with the hinge states and obscure their visibility. Thus, we find that the most visible hinge modes actually occur when no band inversions are present in the material. Our work highlights the interplay and competition between surface and hinge modes in half-Heuslers, and may help guide the experimental search for robust boundary signatures in these materials. In this context, we also present a minimal tight-binding Hamiltonian which captures the topology of materials falling in the space group (216).

Regarding this work, I mainly performed the hinge band structure calculations after obtaining the DFT based wannier tight-binding Hamiltonians from my collaborator Jorge Facio. I also managed to come up with a minimal truncated Wannier tight-binding Hamiltonian, which can be fruitfully used for these material class with space group 216 in order to understand the topology.

1.6.5 Chapter5

Shifting our attention slightly away from realizing the topological phases in real materials, in this chapter we would focus on a very interesting topological transport property, dubbed as Magnus Hall response.

Recently, time-reversal symmetric but inversion broken systems with non-trivial Berry curvature in the presence of a built-in electric field have been proposed to exhibit a new type of linear Hall effect in ballistic regime, namely, the Magnus Hall effect. The transverse current here is caused by the Magnus velocity that is proportional to the built-in electric field enabling us to examine the Magnus responses, in particular, Magnus Hall conductivity and Magnus Nernst conductivity, with chemical potential.

Starting with two-dimensional (2D) topological systems, we find that warping induced asymmetry in both the Fermi surface and Berry curvature can in general enhance the Magnus response for monolayer graphene and surface states of topological insulator. The strain alone is only responsible for Magnus valley

responses in monolayer graphene while warping leads to finite Magnus response there.

Interestingly, on the other hand, strain can change the Fermi surface character substantially that further results in distinct behavior of Magnus transport coefficients as we observe in bilayer graphene. These responses there remain almost insensitive to warping unlike the case of monolayer graphene.

And finally, going beyond 2D systems, we also investigate the Magnus responses in three-dimensional multi-Weyl semimetals (mWSMs) to probe the effect of tilt and anisotropic nonlinear energy dispersion. Remarkably, Magnus responses can only survive for the WSMs with chiral tilt. In particular, our study indicates that the chiral (achiral) tilt engenders Magnus (Magnus valley) responses. Therefore, Magnus responses can be used as a tool to distinguish between the untilted and tilted WSMs in experiments. In addition, we find that the Magnus Hall responses get suppressed with increasing the nonlinearity associated with the band touching around multi-Weyl node.

Chapter 2

Topological crystalline insulators from stacked graphene layers

2.1 Introduction

The foundation of topology in condensed matter physics was first laid by the experimental discovery of the integer quantum Hall effect[1] and the subsequent theoretical work on quantized Hall conductances in two-dimensional (2D) periodic potentials.[3] However, the different ways in which topology can manifest in crystals were mostly unexplored until the prediction of the quantum spin Hall effect in graphene,[23, 24] which was termed a \mathbb{Z}_2 topological insulator (TI). Soon after this, the quantum spin Hall effect and the associated topological phase transition were experimentally observed in HgTe quantum wells.[25, 26] In the following years, the study of topological phases of matter has led to numerous rich discoveries in various condensed matter systems.[5, 6, 36]

Topological insulators are defined as having a gapped bulk, but hosting gapless, anomalous states on their boundaries, states which are protected by the symmetry of the system. Depending on the nature of the symmetry, topologically non-trivial phases are characterized by different integers, called topological invariants. A change in the value of these invariants marks a transition to a topologically different phase, one hosting either a different number of boundary states, or boundary states of a different chirality. A systematic classification of which types of topological phases are possible was first carried out in the case of fundamental symmetries: time-reversal (TRS), particle-hole, and chiral symmetry.[14, 54] Apart from these fundamental symmetries however, spatial

symmetries can also give rise to topological insulating phases in materials. The latter are called weak topological insulators in the case of lattice translations,[36] and topological crystalline insulators (TCI)[40, 42, 41] for symmetries such as mirror, rotation, or glide. Recently, the experimental discovery of mirror symmetry protected TCIs in the SnTe material class has made a tremendous impact in this field of research.[43, 45, 46] There have been many works reported in the literature, classifying TCI based on their lattice symmetries,[55, 38, 56–60] proposing new materials which realize TCI phases,[61, 62, 48] and studying the robustness of their boundary states.[63]

One of the main interesting challenges is to construct new types of topological phases by exploiting the spatial symmetries of the system. In this context, layered structures of suitable materials can be engineered to build topologically nontrivial heterostructures.[64, 65] It has been shown that 3D TCIs can be constructed by stacking 2D TCI layers,[52] but also by using 2D Chern insulators stacked in an antiferromagnetic fashion, such that the sign of the Chern number changes in every second layer.[66] The latter model, called an “antiferromagnetic topological insulator”, was recently modified in order to describe 3D TCIs protected by mirror symmetry,[53] glide symmetry,[67, 68] to show that TCIs can occur in periodically driven systems,[69] as well as to study the newly discovered higher-order TIs.[70–73]

From an experimental point of view, building a heterostructure of Chern insulators with opposite topological invariants is hindered by an immediate practical difficulty. To change the sign of the Chern number one must typically reverse the direction of the applied magnetic field. While this may be achieved on sufficiently long distances, a field reversal on the atomic scale of the heterostructure’s unit cell is highly impractical. One way to overcome this difficulty would be to use 3D materials which order anti-ferromagnetically and simultaneously realize quantum anomalous Hall phases in the 2D limit. However, to our knowledge such a material has not yet been reported.

In this work, we adopt an entirely different strategy, one which does not rely on alternating magnetic fields, but on the Dirac nature of charge carriers in graphene. It is well known that, due to the zeroth Landau level of graphene, the velocity of the quantum Hall edge states can be switched not only by reversing the magnetic field direction, but also under a constant field, by a small shift of the chemical potential across the charge neutrality point.[74] As such, we consider a heterostructure in which the graphene layers are separated by 2D insulating

systems which are polar, as shown in Fig. 2.1. By reversing the polarization of every second spacer layer, it is in principle possible to obtain a system in which adjacent graphene sheets have an alternating electron and hole doping. In this case, applying a uniform magnetic field along the stacking direction opens a topological gap in the graphene layers, but in such a way that they carry opposite Chern numbers.

In the following, we examine the system in two different limits, depending on which materials are used for the spacer layers. If the latter are composed of light elements, we can expect spin-orbit coupling (SOC) to be negligible, and the heterostructure can be treated as an effectively spinless model. In Section 2.2, we show that in this case an intrinsically magnetic TCI phase is realized, one which requires an externally applied magnetic field to exist. On the other hand, when the polar spacers contain heavy elements, they may lead to proximity-induced SOC in the graphene layers, such that each layer forms a quantum-spin Hall phase.[75] In Section 2.3, we show that when SOC terms are larger than the doping, a time-reversal symmetric TCI phase can be realized. We conclude and discuss directions for future research in Section 4.6.

2.2 Stack of Chern insulating layers of graphene

We begin by examining the first of two limits, in which the graphene sheets experience a negligible SOC, such that the heterostructure forms an effectively spinless system. In this limit, we show that due to the alternating electron and hole doping of adjacent layers, applying a magnetic field parallel to the stacking direction results in a mirror symmetry protected TCI.

In the absence of SOC, the out of plane spin component of electrons in graphene is conserved, such that each spin sector can be treated independently. We therefore model the heterostructure as a 3D system of spinless electrons hopping on a lattice of AA-stacked honeycomb layers. The real space Hamiltonian reads

$$\begin{aligned} \mathcal{H} = & \sum_{\langle ij \rangle, \alpha} t c_{i,\alpha}^\dagger c_{j,\alpha}^{\alpha} + \mu \sum_{i,\alpha} (-1)^\alpha c_{i,\alpha}^\dagger c_{i,\alpha}^{\alpha} \\ & + \sum_{i,\alpha} \left[t_z c_{i,\alpha}^\dagger c_{i,\alpha}^{\alpha+1} + \text{h.c.} \right], \end{aligned} \quad (2.1)$$

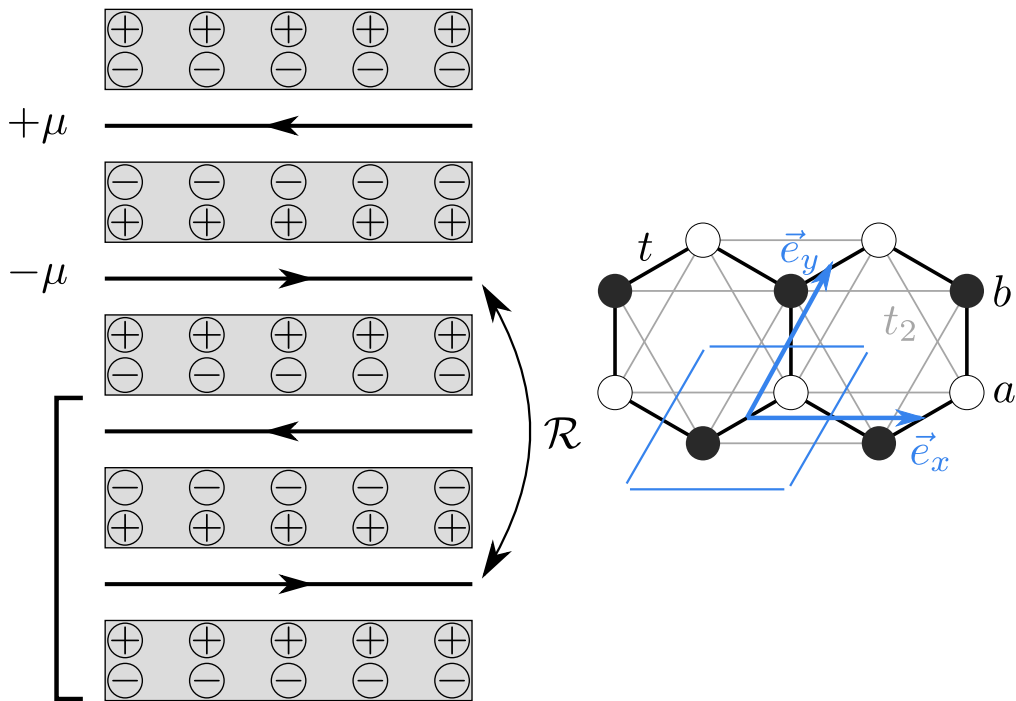


Fig. 2.1 Left: Three-dimensional system formed out of graphene layers (horizontal lines) separated by thin insulating layers (gray boxes). The spacers are polar, having a positively charged (+) and a negatively charged (−) side. Using spacer layers with an alternating orientation leads to graphene sheets which have an alternating doping ($\pm\mu$). The unit cell of the heterostructure (bracket) consists of two graphene layers, and the full system shows reflection symmetry about one layer (\mathcal{R}). By applying a uniform magnetic field along the stacking direction, neighboring graphene layers form quantum Hall phases with opposite Chern numbers, such that their chiral edge states propagate in opposite directions (horizontal arrows). Right: our conventions for the graphene lattice, with Bravais vectors \vec{e}_x and \vec{e}_y . Nearest and next nearest neighbor hoppings are labeled t and t_2 . There are two sites, denoted a and b in every unit cell (marked by a blue contour).

where $c_{i,\alpha}^\dagger$ ($c_{i,\alpha}$) creates (annihilates) fermions on site i in layer α and $\langle \dots \rangle$ denotes nearest neighbors (see Fig. 2.1). The first term is a nearest neighbor hopping, which we set to $t = 1$ throughout the following, whereas μ is an on-site energy which models the alternating doping of adjacent graphene systems. As such, there are two layers in each unit cell. The last term of Eq. (2.1) models inter-layer coupling, with hopping to the layer below having an amplitude t_z and hopping to the layer above an amplitude t_z^* . In practice, this term will decay exponentially with the separation of neighboring graphene sheets, requiring the use of very thin spacers. However, as we show in the following, a TCI phase can

be realized even when t_z is the smallest energy scale of the problem, provided it does not vanish exactly. In the latter case, the system cannot be treated as three-dimensional, since the heterostructure is composed of isolated 2D systems.

The momentum space form of Eq. (2.1) is given by

$$\begin{aligned} \mathcal{H}(\vec{k}) &= \begin{pmatrix} \mathcal{H}_+(k_x, k_y) & t_z^* + t_z e^{-ik_z} \\ t_z + t_z^* e^{ik_z} & \mathcal{H}_-(k_x, k_y) \end{pmatrix} \\ \mathcal{H}_\pm(k_x, k_y) &= t \left[1 + \cos(k_x) + \cos(k_y) \right] \tau_x \\ &\quad + t \left[\sin(k_x) + \sin(k_y) \right] \tau_y \pm \mu \end{aligned} \quad (2.2)$$

Here, \mathcal{H}_\pm are the Hamiltonians of graphene layers experiencing a $\pm\mu$ energy shift, $\vec{k} = (k_x, k_y, k_z)$, $k_{x,y}$ are the in-plane momentum components along $\vec{e}_{x,y}$ (see Fig. 2.1), and k_z is the momentum along the stacking direction. The Pauli matrices τ parameterize the a and b sublattice degree of freedom. Lastly, the 2×2 grading on the first line of Eq. (2.2) encodes the degree of freedom associated to the two layers in the unit cell, which we denote in the following using Pauli matrices η .

Choosing a real valued inter-layer coupling, $t_z = t_z^*$, the Hamiltonian Eq. (2.2) obeys a spinless mirror symmetry of the form

$$\mathcal{R}(k_z) = \tau_0 \otimes \begin{pmatrix} 1 & 0 \\ 0 & e^{ik_z} \end{pmatrix}, \quad (2.3)$$

such that

$$\mathcal{R}(k_z) \mathcal{H}(k_x, k_y, k_z) \mathcal{R}(k_z)^{-1} = \mathcal{H}(k_x, k_y, -k_z). \quad (2.4)$$

As a consequence, the terms proportional to t_z vanish on the mirror invariant plane of the Brillouin zone, $k_z = \pi$, and the two graphene monolayers are effectively decoupled from each other. Further, since for $k_z = \pi$ the mirror operator is $\mathcal{R} = \tau_0 \eta_z$, electronic states in adjacent monolayers have different mirror eigenvalues, $+1$ and -1 . This naturally opens the possibility of stabilizing a mirror symmetry protected TCI if the graphene sheets enter Chern insulating phases when a magnetic field is applied.

Since we are dealing with an effective spinless model valid for each of the two spin sectors, we introduce an orbital magnetic field through the usual Peierls substitution. We choose a gauge in which the in-plane hopping within each unit cell is modified as $t \rightarrow t \exp(i\Phi n_y)$, where n_y is an integer labeling the unit cells

in the \vec{e}_y direction (see Fig. 2.1), and Φ is the Peierls phase. The latter physically represents the number of magnetic fluxes penetrating a hexagonal plaquette with area a_{\square} due to a perpendicular magnetic field B , such that $\Phi = Ba_{\square}e/h$.

Using the Kwant code,[76, 77] we compute the bandstructure of a single graphene sheet in a ribbon geometry with zig-zag edges, translationally invariant along \vec{e}_x , and consisting of $W = 100$ unit cells in the \vec{e}_y direction (see Fig. 2.1). Note that our gauge choice for the Peierls substitution is only compatible with translation symmetry along \vec{e}_x . As shown in Fig. 2.2, for a single graphene monolayer the gapless Dirac cone spectrum becomes gapped under the addition of the orbital field, which leads to the formation of Landau levels. Characteristic to graphene and other hexagonal lattice systems, there exists a Landau level at the charge neutrality point, $E = 0$. Away from this point, the system enters quantum Hall phases with opposite Chern numbers, $C = +1$ for $E > 0$ and $C = -1$ for $E < 0$.

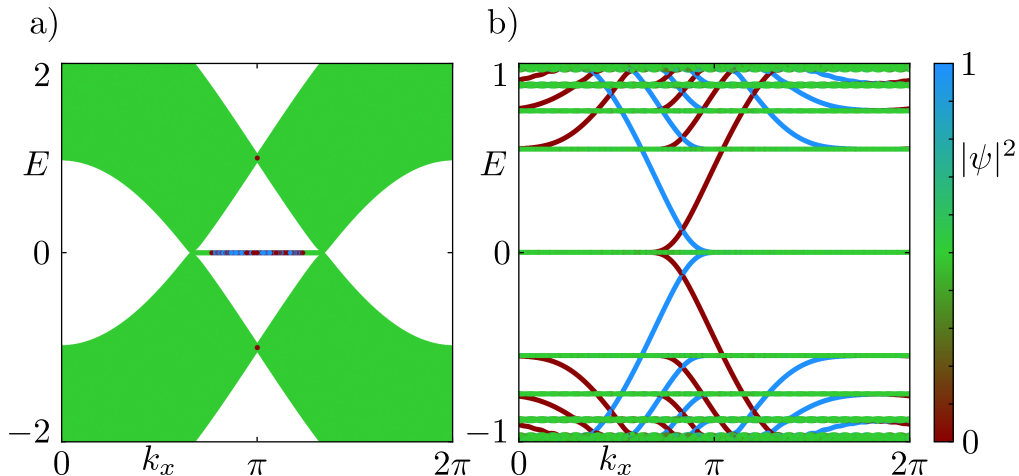


Fig. 2.2 Bandstructure of a single monolayer of spinless graphene in a ribbon geometry (infinite along \vec{e}_x , $W = 100$ unit cells along \vec{e}_y), using $t = 1$ and $\mu = 0$. In the absence of a magnetic field ($\Phi = 0$, panel a), two bulk Dirac cones are connected by dispersionless boundary states localized on the two zig-zag edges of the ribbon. With a magnetic flux $\Phi = 0.18$ (panel b) the bulk spectrum consists of Landau levels, and chiral edge modes appear at the two boundaries of the ribbon. The color scale denotes the probability density of a state integrated over half of the ribbon (unit cells indexed by $0 \leq n_y < W/2$), such that modes localized on opposite boundaries of the ribbon are shown in blue and red, respectively.

Given the bandstructure of Fig. 2.2b, we expect the alternating doping μ to ensure that adjacent graphene layers of the 3D system have opposite Chern

numbers after the magnetic field is turned on, so that their chiral edge states have opposite velocities. Moreover, since states of neighboring graphene sheets are decoupled at $k_z = \pi$ and have opposite mirror eigenvalues, these chiral modes remain orthogonal on the mirror invariant plane due to Eq. (2.4), leading to the formation of surface Dirac cones. The full heterostructure then realizes a mirror symmetric TCI phase with a mirror Chern number

$$C_M = \frac{C_+ - C_-}{2}, \quad (2.5)$$

where $C_{\pm} = \pm 1$ are the Chern numbers (computed at $k_z = \pi$) of graphene layers experiencing a $\pm \mu$ energy shift, such that $C_M = 1$. Note that, due to Eqs. (2.3) and (2.4), on the plane $k_z = 0$ the reflection operator is equal to the identity matrix, $\mathcal{R}(0) = 1$. The system then cannot be block-diagonalized into different mirror eigenspaces. It could still be possible that the full Chern number at $k_z = 0$ is nonzero, but, lacking disjoint sectors with opposite mirror eigenvalue, such a topological phase would not be protected by mirror symmetry, corresponding instead to a stack of quantum Hall systems with co-propagating edge modes.

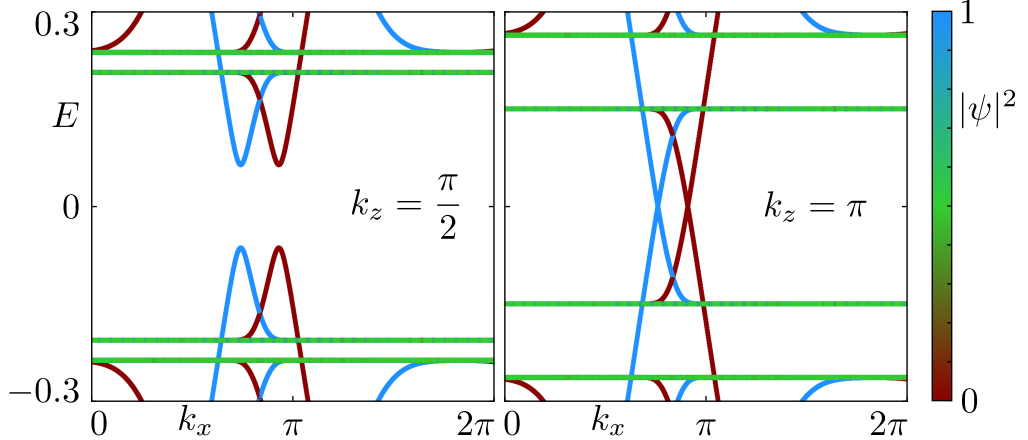


Fig. 2.3 Bandstructure of the graphene heterostructure with Hamiltonian Eq.(2.2) in an infinite slab geometry with hard wall boundary conditions in the \vec{e}_y direction and a width of $W = 100$ unit cells. We use $t = 1$, $\Phi = 0.18$, $\mu = 0.3$, and $t_z = 0.1$. The left and right panels show the bandstructures for $k_z = \pi/2$ and $k_z = \pi$, respectively. One Dirac cone appears on each surface, positioned on the mirror invariant $k_z = \pi$ line of the surface BZ. The color scale is the same as in Fig. 2.2. In order for the inter-layer coupling to efficiently gap out the edge modes away from the mirror line, we have added a sublattice symmetry breaking term to the model $\mu_s \tau_z \eta_z$, with $\mu_s = 0.15$.

We confirm the presence of surface Dirac cones by computing the bandstructure of Eq. (2.2) in a slab geometry, infinite in the stacking direction and along \vec{e}_x , but containing $W = 100$ sites in the \vec{e}_y direction. As shown in Fig. 2.3, on each surface the chiral modes of adjacent layers cross at $k_z = \pi$, but gap out away from this line, forming a surface Dirac cone protected by mirror symmetry. When determining the bandstructures, we have noticed that due to the high symmetry of $\mathcal{H}(\vec{k})$, the inter-layer coupling t_z does not efficiently couple the chiral modes away from the mirror plane, leading to surface nodal lines that wind across the surface BZ in the k_z direction. The surface nodal lines are a consequence of a spurious sublattice symmetry of the model, and occur both for zig-zag and armchair terminations of the graphene layers. Since we are interested in the phenomenology of TCIs protected purely by mirror, we have lowered the symmetry of the initial Hamiltonian $\mathcal{H}(\vec{k})$ by adding a sublattice symmetry breaking term, $\mu_s \tau_z \eta_z$, which enables the chiral edge modes to couple away from $k_z = \pi$. This term does not break the mirror symmetry Eq. (2.3), such that the mirror Chern number remains non-trivial, provided that μ_s is not large enough to close the bulk gap.

As we have shown, the heterostructure of oppositely doped graphene layers enters a TCI phase under an externally applied magnetic field. Unlike previously observed TCIs, this phase is only present when time-reversal symmetry is explicitly broken, since the spectrum is gapless in the zero field case. As long as SOC is negligibly weak, each spin component of the graphene charge carriers behaves according to the Hamiltonian Eq. (2.2), such that the full system contains two surface Dirac cones, which are protected by the conservation of the out of plane spin component. Further, the precise form of the mirror symmetry Eq. (2.3) may be tuned by altering the materials forming the polar spacer layers, and therefore the inter-layer coupling t_z . If, for instance, we choose an imaginary hopping between graphene monolayers, $t_z = -t_z^*$, then the mirror operator would read $\mathcal{R} = \tau_0 \otimes \text{diag}(1, -e^{ik_z})$, and the surface Dirac cones would be positioned at a different mirror invariant plane, $k_z = 0$. Notice however that for a generic, complex valued t_z the heterostructure Hamiltonian Eq. (2.2) would break both this mirror symmetry and that of Eq. (2.3). To introduce complex inter-layer hoppings one would have to modify Eq. (2.2) such that the phase of the hopping to the layer above is opposite to the phase of the hopping to the layer below. For instance, replacing the off-diagonal blocks of this Hamiltonian with $|t_z|e^{i\theta}(1 + e^{ik_z})$ would preserve mirror symmetry for any

value of the complex phase θ , as evidenced by the fact that the term still vanishes at $k_z = \pi$.

Finally, we note that there is no threshold value of t_z for which a TCI phase is realized, meaning that the inter-layer coupling can be the smallest energy scale of the problem. Reducing the value of t_z by increasing the thickness of the spacer layers does not remove the topologically protected surface Dirac cones, but simply reduces their velocity in the k_z direction.

2.3 Stack of quantum spin-Hall layers of graphene

The negligibly small value of SOC in free standing graphene[78, 79] enabled us to use a spinless model when discussing the heterostructure of Fig. 2.1, provided that the polar spacers contain light elements. It is however known that graphene in proximity to heavy atoms or 2D materials containing heavy atoms may lead to large induced SOC terms.[80, 81] In Ref. [82] for instance, it was shown that a SOC-driven quantum spin-Hall phase with a gap as large as 80 meV may be realized in graphene sandwiched between oppositely oriented 2D layers of BiTeX (X=Cl, Br, I). Motivated by this fact, in the following we study the heterostructure in the limit in which SOC is larger than the alternating doping of adjacent graphene sheets.

We describe the system using AA-stacked copies of spin- $\frac{1}{2}$ graphene models. The 3D real space Hamiltonian now reads

$$\begin{aligned} \mathcal{H}_{\frac{1}{2}} = & \sum_{\langle ij \rangle, \alpha} t c_{i,\alpha}^\dagger c_{j,\alpha}^{j,\alpha} + \mu \sum_{i,\alpha} (-1)^\alpha c_{i,\alpha}^\dagger c_{i,\alpha}^{i,\alpha} \\ & + \sum_{\langle\langle ij \rangle\rangle, \alpha} i t_2 \nu_{ij} c_{i,\alpha}^\dagger \sigma_z c_{j,\alpha}^{j,\alpha} \\ & + \sum_{i,\alpha} \left[c_{i,\alpha}^\dagger T_z c_{i,\alpha}^{i,\alpha+1} + \text{h.c.} \right], \end{aligned} \quad (2.6)$$

where $c_{i,\alpha}^\dagger = (c_{i,\alpha,\uparrow}^\dagger, c_{i,\alpha,\downarrow}^\dagger)$ creates fermions with spin \uparrow, \downarrow on site i in layer α , $\langle \dots \rangle$ and $\langle\langle \dots \rangle\rangle$ denote nearest and next nearest neighbors (see Fig. 2.1), and the Pauli matrices σ parameterize the spin degree of freedom. The first two terms, t and μ , have the same meaning as before, whereas the term proportional to t_2 is the usual intrinsic SOC term,[75] an imaginary next nearest neighbor hopping. The sign $\nu_{ij} = \pm 1$ is positive whenever the path connecting sites i and j rotates

counter-clockwise, and negative for a clockwise rotation. Finally, T_z is a matrix describing electron hopping between neighboring graphene layers.

As before, we begin by discussing the decoupled limit $T_z = 0$, when each of the graphene layers is an independent 2D system. Since in the simple model Eq. (2.6) the SOC term commutes with σ_z , we can write the Hamiltonian separately for each spin component $s = \pm$ and each of the two layers in a unit cell $l = \pm$ as

$$\begin{aligned} \mathcal{H}_{l=\pm, s=\pm} = & t \left[1 + \cos(k_x) + \cos(k_y) \right] \tau_x + \\ & t \left[\sin(k_x) + \sin(k_y) \right] \tau_y + l \cdot \mu \tau_0 + \\ & s \cdot 2t_2 \left[\sin(k_x) - \sin(k_y) \right. \\ & \left. - \sin(k_x - k_y) \right] \tau_0. \end{aligned} \quad (2.7)$$

The heterostructure obeys a spinful time-reversal symmetry with operator $\mathcal{T} = i\tau_0\eta_0\sigma_y\mathcal{K}$ and \mathcal{K} complex conjugation. Further, the system also obeys a spinful mirror symmetry about one layer, which takes the form

$$\mathcal{R}_{\frac{1}{2}}(k_z) = \begin{pmatrix} \tau_0\sigma_z & 0 \\ 0 & \tau_0\sigma_z e^{ik_z} \end{pmatrix}, \quad (2.8)$$

where the 2×2 grading is in the layer degree of freedom, η . Note that the reflection symmetry Eq. (2.8) anti-commutes with the time-reversal symmetry operator. In general, the commutation relation between the two operators is gauge dependent, since it is always possible to re-define $\mathcal{R}_{\frac{1}{2}} \rightarrow i\mathcal{R}_{\frac{1}{2}}$, such that the new operator commutes with time-reversal. We choose the basis conventionally used in topological classification studies,[38] in which the two symmetries anti-commute if the system is spinful.

The two spin eigenstates in each monolayer have opposite mirror eigenvalues.[83, 84] This means that under the addition of an intrinsic SOC term, $t_2 > 0$, each graphene sheet simultaneously realizes a quantum spin-Hall phase as well as a 2D TCI phase, since the different spin sectors have opposite Chern numbers $C = \pm 1$.

For the inter-layer coupling we choose a term which respects both time-reversal as well as mirror symmetry, but mixes the two spin components, as one can expect when the polar spacers contain heavy elements. We set $T_z = i\sigma_x t_z$ in Eq. (2.6), where the real number t_z is the strength of the coupling, such that the

full momentum space Hamiltonian is

$$\mathcal{H}_{\frac{1}{2}}(\vec{k}) = \begin{pmatrix} \mathcal{H}_{+,+} & 0 & 0 & A \\ 0 & \mathcal{H}_{+,-} & A & 0 \\ 0 & A^\dagger & \mathcal{H}_{-,+} & 0 \\ A^\dagger & 0 & 0 & \mathcal{H}_{-,-} \end{pmatrix} \quad (2.9)$$

with $A = it_z(1 - e^{ik_z})\tau_0$. Notice that according to Eq. (2.8), even when the inter-layer coupling is added, there are now two different planes on which a mirror Chern number can be defined, $k_z = 0$ and $k_z = \pi$, unlike the spinless model discussed in the previous section. Crucially however, the mirror eigenvalues of every second layer reverse when going from $k_z = 0$ to $k_z = \pi$, which allows for a different mirror Chern number on each mirror invariant plane. When $k_z = 0$, eigenstates of the spin-up sector (i.e. those of $\mathcal{H}_{+,+}$ and $\mathcal{H}_{-,+}$) have the same mirror eigenvalue as well as the same Chern number, both of which are opposite to those of $\mathcal{H}_{+,-}$ and $\mathcal{H}_{-,-}$. As such, the 3D coupled system realizes a TCI with mirror Chern number $C_M = 2$, and two surface Dirac cones are expected to appear on the $k_z = 0$ line of the surface BZ. On the other plane, $k_z = \pi$, the mirror eigenvalues switch both when changing the spin sector as well as the layer, leading to a trivial topological invariant. This is because the eigenspace with positive mirror eigenvalue is formed by $\mathcal{H}_{+,+}$ and $\mathcal{H}_{-,-}$, which in total have a vanishing Chern number.

To confirm the presence of surface Dirac cones only at $k_z = 0$, we plot in Fig. 2.4 the bandstructure of the system in an infinite slab geometry, with translational invariance along the stacking direction and \vec{e}_x , and containing $W = 100$ unit cells in the \vec{e}_y direction. The intrinsic SOC term $t_2 = 0.5$ is now larger than the alternating doping, $\mu = 0.1$, such that each graphene layer independently realizes a quantum spin-Hall phase. At $k_z = 0$, the mirror Chern number $C_M = 2$ means that surface states with the same mirror eigenvalue propagate in the same direction, such that they cannot be gaped out. In contrast, at $k_z = \pi$, there are surface modes with opposite velocities in each mirror eigenspace, allowing the inter-layer coupling to produce a gapped surface.

Finally, notice that for this system the topological surface modes would persist even in the limit of vanishing doping, $\mu = 0$. In this case, the unit cell would be halved, containing a single monolayer, and the heterostructure would realize a weak topological insulator, protected by time-reversal symmetry and translation along the stacking direction. However, the additional mirror

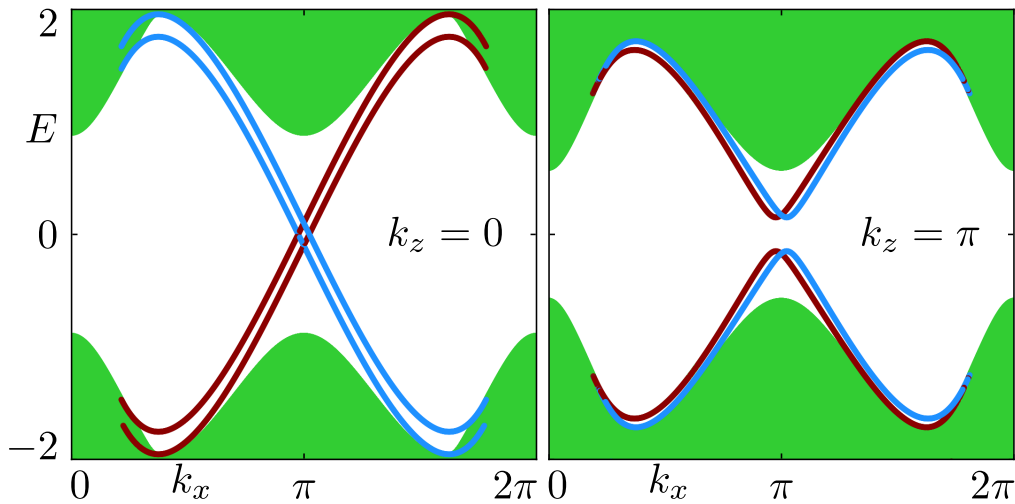


Fig. 2.4 Bandstructure of the spinful graphene heterostructure [Eq. (2.9)] in an infinite slab geometry ($W = 100$ unit cells along \vec{e}_y). We use $t = 1$, $t_2 = 0.5$, $\mu = 0.1$, and $t_z = 0.2$. Only bulk modes (shown in green) and states on one of the two surfaces are plotted. The color of the surface modes denotes the mirror sector of each state: red for an eigenvalue $+1$ and blue for -1 . At $k_z = 0$ (left), the nonzero mirror Chern number leads to the appearance of two Dirac cones on the surface. States having the same mirror eigenvalue propagate in the same direction, so they are topologically protected. In contrast, for the other mirror invariant plane $k_z = \pi$ (right), the mirror Chern number vanishes. There are both left and right moving surface modes in each of the two mirror sectors, which are gapped out by the inter-layer coupling term.

symmetry Eq. (2.8) leads to an increased protection of the surface Dirac cones, allowing them to persist even as $\mu \neq 0$, due to the system's non-trivial mirror Chern number.

2.4 Conclusion

We have shown that multilayers of graphene can exhibit a topological crystalline insulating phase protected by reflection symmetry. We considered a heterostructure formed by graphene monolayers sandwiched between oppositely oriented 2D polar spacers, such as BiTeX[82] or ultra-thin ferroelectric polymers.[85, 86] The spacers may lead both to an alternating doping as well as to a proximity induced SOC in the graphene sheets. Both limits were shown to lead to a mirror-symmetry protected TCI phase, hosting two Dirac cones on each surface. When the polar spacers are made of light elements, such that they induce a negligibly

small SOC, the heterostructure can be treated as an effectively spinless system. In this case, we have shown that due to the alternating electron and hole doping of adjacent graphene layers, they form quantum Hall phases with opposite Chern numbers under a uniform magnetic field. The resulting phase is an “intrinsically magnetic TCI”, one which requires the breaking of time-reversal symmetry in order to exist. In the opposite limit, when SOC is larger than the doping, the system instead realizes a time-reversal symmetric TCI with a mirror Chern number of 2. Similar to KHgX ($\text{X}=\text{As, Sb, Bi}$),[47] the surface modes can be understood as originating from two quantum spin-Hall systems which are forbidden to gap each other out in the presence of mirror symmetry.

Our work focused only on toy models and discussed the possibility for TCI heterostructures to exist as a proof of principle. We hope that this study will motivate future ab initio approaches to graphene heterostructures and their potential for realizing TCIs. There are a large number of 2D materials which may be combined in van der Waals heterostructures[87–89] and which show a variety of physical properties, such as polarity, magnetism, or SOC. It would be interesting to combine machine learning algorithms with density functional theory methods to automate the search for topologically non-trivial heterostructures.

On the experimental side, we expect that such layered systems will first be fabricated using only a few graphene sheets, so that the system is not fully three-dimensional. In the small thickness regime, it may be possible to gate the sample using external electrodes, such that the doping of adjacent graphene monolayers can be more readily controlled. Further, studying heterostructures composed of a few layers would open the possibility of observing the so called “even-odd effect” in TCIs. The latter was originally discussed in WTIIs,[90] and states that a system containing an even number of layers may be gapped by inter-layer coupling, whereas one containing an odd number must host topologically protected gapless modes on its surface. For the systems studied here, the same criterion applies with respect to the parity of the number of graphene sheets, both in the time-reversal symmetric and in the magnetic TCI limits.

Chapter 3

Dual topology in Jacutingaite Pt_2HgSe_3

3.1 Introduction

The understanding of bulk-boundary correspondence in condensed matter systems — namely, the connection between bulk topological invariants and electronic properties at the system boundary — has come a long way since the discovery of the quantum Hall effect [3]. This path exhibits as hallmarks the generalization to systems with time-reversal symmetry, which lead to the discovery of three-dimensional (3D) strong topological insulators (TIs) [91, 92, 37], the subsequent understanding of the role played by crystalline symmetries, which lead to the identification of weak topological insulators (WTIs) [37, 90] and of topological crystalline insulators (TCIs) [40, 93], and the comprehension of how the correspondence works in topological semimetals [94–97]. Recently, the relation between bulk and boundary has been further extended by the discovery of higher-order topological insulators (HOTIs) [98–114, 71, 115–121].

The identification of materials that can realize topologically nontrivial phases is naturally important. Recently, it was predicted that a two-dimensional (2D) monolayer of the naturally occurring mineral called Jacutingaite [122], Pt_2HgSe_3 , can realize the quantum spin Hall insulator (QSHI) state [123]. Furthermore, it was argued that the competition between large spin-orbit coupling, associated with Hg and Pt atoms, and inherent lattice instabilities towards the breaking of inversion symmetry lead to a topological state robust at room temperature and switchable by external electric fields. First experimental results on the

QSHI state have been reported [124], and it was suggested that the monolayer may become superconducting as well [125]. In view of these results, it is of interest to study the topological properties of the electronic structure in the three-dimensional compound.

In this work, we first address this issue and show that Pt_2HgSe_3 is both a weak topological phase and a mirror-protected topological crystalline phase. This result places Jacutingaite in the list of materials which can host surface states protected by different, unrelated crystalline symmetries [126–128, 103, 129, 48]. Second, we construct minimal tight-binding models that capture the essential topological properties of this dual topological phase in materials with three-fold rotation symmetry and compare their associated surface spectral density with those of different materials in the class.

The rest of this work is organized as follows. In Sections 3.2 and 3.3 we use density functional theory to determine the bulk bandstructure of Pt_2HgSe_3 , together with its topological invariants and surface states. We then introduce tight-binding models which reproduce the topology of this material in Section 3.4, and conclude in Section 3.5. The Appendix is devoted to providing results on Pd_2HgSe_3 , as well as more details on the tight-binding models.

3.2 Topological characterization

Pt_2HgSe_3 and Pd_2HgSe_3 are layered compounds with space group $P\bar{3}m1$ (164) [122, 130]. The Hg atoms are positioned in a triangular environment delimited by planes of Se and Pt (or Pd) and form a buckled honeycomb lattice [see Fig. 3.1a]. We performed fully relativistic density functional theory (DFT) calculations using the generalized gradient approximation (GGA) for the exchange and correlation functional [131],¹. In the following, we base our discussion on the Pt compound, but similar results are obtained for the Pd case (presented in Appendix 3.6). Figure 3.1c shows the bandstructure of Pt_2HgSe_3 and its density of states, $D(\varepsilon)$, which indicates that the material is a semimetal with small electron and hole pockets. Similar to Bi [104], the spin-orbit coupling (SOC) opens a topological gap (~ 20 meV) throughout the full Brillouin zone (BZ) between the bands that gives rise to the electron pockets and those that host the

¹We used the FPLO code [131] version 18.55 with a tetrahedron method for numerical integrations using 16^3 k-point mesh in the BZ.

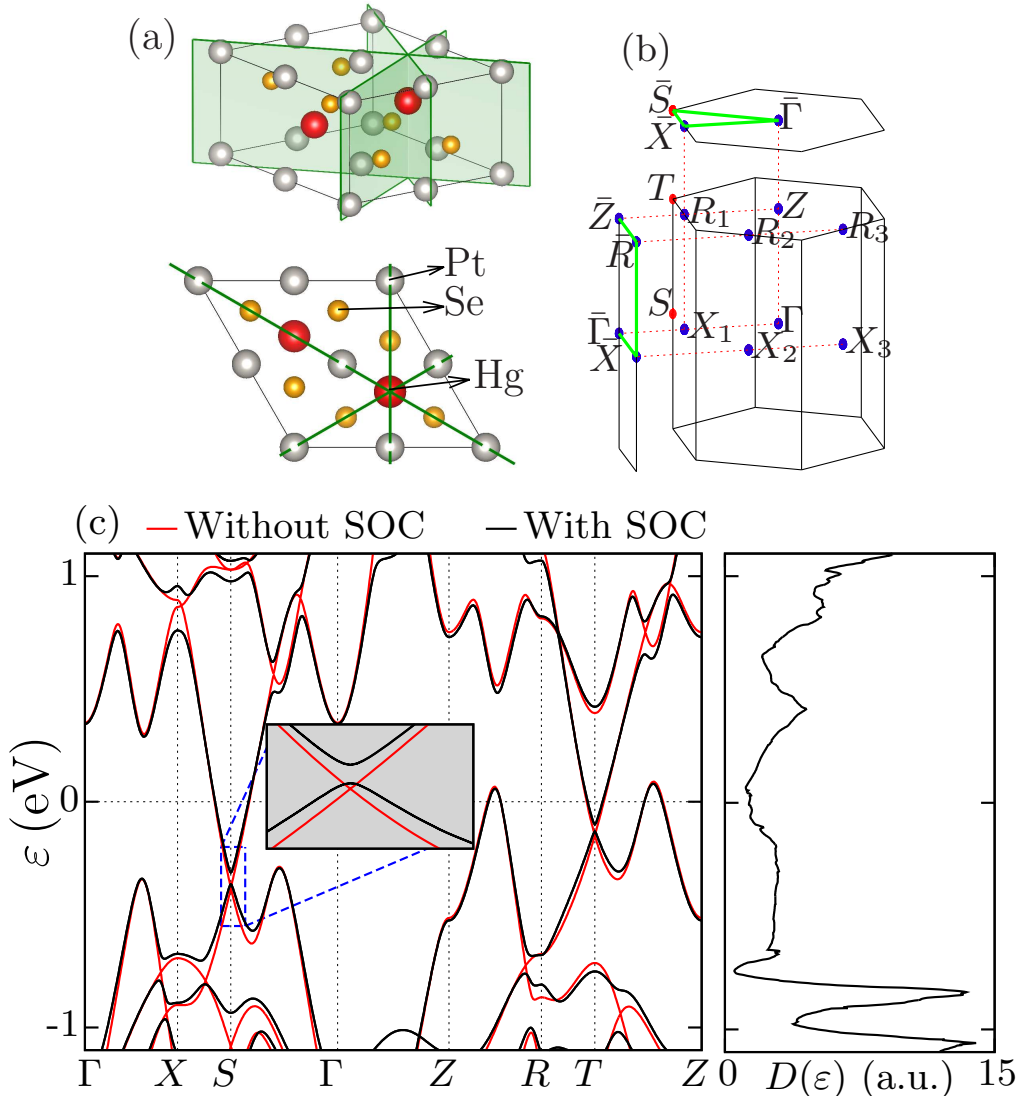


Fig. 3.1 Panel (a): Crystal structure of Pt_2HgSe_3 . The three mirror planes are shown as shaded areas (top) and as green lines (bottom). Panel (b): Bulk and surface Brillouin zones (BZ). Time-reversal invariant points are colored blue and points belonging to the surface BZ are indicated with an over-line. Panel (c): Bandstructure and density of states, $D(\varepsilon)$, of Pt_2HgSe_3 with (black) and without (red) spin-orbit coupling.

hole pockets. This allows us to characterize the topological structure of the latter set of bands.

We first focus on the \mathbb{Z}_2 time-reversal polarization invariants [35, 132]. Since the system has inversion symmetry, we use the Fu-Kane formulas based on the parity of the occupied Bloch states at the time-reversal invariant momenta (TRIM) in the Brillouin zone (BZ) [36]. The TRIM are sketched in Fig. 3.1b

and the parity invariants take the values $\delta(X) = \delta(R) = 1$ and $\delta(\Gamma) = \delta(Z) = -1$. Hence, we obtain the four \mathbb{Z}_2 indexes $(\nu_0; \nu_1 \nu_2 \nu_3) = (0; 001)$, where ν_0 is the strong topological invariant and $\nu_{1,2,3}$ are the three weak topological invariants. This result is consistent with the idea of engineering weak topological insulators by stacking QSHI layers along one direction, previously realized in KHgSb [133], Bi_xSe_y [134] and $\text{Bi}_{14}\text{Rh}_3\text{I}_9$ [135]. Namely, if the stacking preserves translational invariance along the stacking direction, z in our case, the helical edge states associated with each QSHI layer form surface Dirac cones at momenta $k_z = 0, \pi$. As long as translation symmetry is preserved, the surface Dirac cones cannot hybridize and gap out, since they occur at different k_z . Note, however, that not all materials which realize a QSHI in the single layer limit are in a 3D weak topological phase, a counter-example being elemental Bi [136]. As such the topological invariants of the bulk compound cannot, in general, be inferred from the behavior of a monolayer.

We also note in passing an ambiguity associated with the methodology used for computing the parity invariants. While our calculation includes all of the occupied Kramers pairs, ab-initio methods based on pseudo-potentials necessarily constrain the calculation to states in a certain energy windows and this may result in a global sign difference of the parity invariants. For instance, when performing calculations using the VASP code [137, 138], we obtained the opposite indexes, +1 at Γ and Z and -1 at the other TRIMs ². This ambiguity is nevertheless of little importance, since predictions regarding the surface spectral density involve in general a product of an even number of parity invariants [139].

An alternative view of the nontrivial topology is provided by the framework of elementary band representations (EBRs) [140, 141]. According to this view, the nontrivial topology should be reflected in the fact that it is not possible to decompose the occupied bands into physical EBRs. In centrosymmetric systems, a distinctive property of physical EBRs is that the number of parity eigenvalues equal to -1 per Kramers pair must be a multiple of 4, a fact that provides a simple criterion to assess whether a material is topologically trivial or not [142]. We find that the number of negative parity eigenvalues modulo 4 to be 2, thus demonstrating nontrivial topology ³.

The stacking of 2D Pt_2HgSe_3 layers in 3D Jacutingaite preserves symmetries other than translation, which can lead to additional topological invariants. In

²In the VASP calculation the parity invariants are computed for states in the energy windows $[-17.5, 0]$ eV.

³We find 64 parity eigenvalues equal to -1 at X and R and 61 at Γ and Z .

particular, in this work we focus on the reflection symmetries: one mirror plane in momentum space contains the points Γ , Z and X , while two additional mirrors are obtained by $2\pi/3$ rotations with respect to the z axis [see Fig. 3.1a and b]. Since a mirror rotates the electron spin by an angle π , it leads to a wavefunction of opposite sign when applied twice. Therefore, the mirror symmetry operator satisfies $M^2 = -1$ and, accordingly, Bloch states belonging to a mirror plane can be labeled with a mirror eigenvalue equal to $\pm i$. This introduces a partition of the space formed by Bloch states with momentum in the mirror plane into two subspaces and allows to define a Chern number in each of them as

$$C^\pm = \frac{1}{2\pi} \sum_n \int_{\mathcal{M}} d\mathbf{S} \cdot \Omega_n^\pm(\mathbf{k}). \quad (3.1)$$

Here, n labels occupied states, $d\mathbf{S}$ is a differential surface element of the mirror plane \mathcal{M} and $\Omega_n^\pm(\mathbf{k})$ is the Berry curvature associated with the subspace of mirror eigenvalue $\pm i$. It is computed as $\Omega_n^\pm(\mathbf{k}) = \nabla_{\mathbf{k}} \times \mathbf{A}_n^\pm(\mathbf{k})$, with $\mathbf{A}_n^\pm(\mathbf{k}) = -i\langle u_{n\mathbf{k}}^\pm | \partial_{\mathbf{k}} u_{n\mathbf{k}}^\pm \rangle$ the Berry connection, and $|u_{n\mathbf{k}}^\pm\rangle$ the Hamiltonian eigenstates within a given subspace. A nonzero mirror Chern number, $C_{\mathcal{M}} = (C^+ - C^-)/2$, signals the existence of topologically protected states on surfaces that preserve the mirror symmetry. In Pt_2HgSe_3 and Pd_2HgSe_3 we obtain $C_{\mathcal{M}} = -2$ for each of the three mirror planes⁴, which means that these materials can realize helical HOTI phases under suitable surface perturbations, as shown in Ref. [103]. Together with the nontrivial weak topological invariant, the nonzero mirror Chern numbers enable us to predict that Pt_2HgSe_3 is in a dual topological phase, one which is present in a naturally occurring mineral.

3.3 Surface Dirac cones

We now present surface spectral densities computed for semi-infinite systems obtained by cutting the crystal perpendicular to the [100] or [001] directions. In both cases, we chose surfaces terminated by Hg atoms. For these calculations, we built a tight-binding Hamiltonian based on Wannier functions associated with orbitals $6s$, $6p$, and $5d$ of Hg and of Pt, and $4p$ of Se. The Wannier-interpolated band-structure accurately reproduces the DFT results in the energy range $[-9\text{eV}, 5\text{eV}]$.

⁴As a benchmark, we have computed the mirror Chern number for Bi_2Te_3 , obtaining as a result -1, and for SnTe , obtaining as a result -2, values that agree with the literature.

Figure 3.2a shows the momentum-resolved spectral density associated with the [100] surface along a path connecting the surface TRIMs $\bar{\Gamma}$, \bar{X} , \bar{R} , and \bar{Z} [see Fig. 3.1b]. The spectral density features two Dirac cones, one centered at \bar{X} and one at \bar{R} . The connectivity of these surface states with the projection of the bulk valence and conduction bands is consistent with the surface fermion parity invariants, which can be computed from the bulk parity invariants as $\pi(\Lambda_a) = (-1)^{n_b} \delta(\Gamma_i) \delta(\Gamma_j)$ [139]. Here, $\Gamma_{i,j}$ are the bulk TRIMs, whose projection coincides with the surface TRIM Λ_a , and n_b is the number of occupied Kramers pairs. The opposite parity invariants at Γ and X makes $\pi(\bar{\Gamma})$ and $\pi(\bar{X})$ have opposite signs. This reflects a change in the time-reversal polarization on going from $\bar{\Gamma}$ to \bar{X} and, accordingly, along a path connecting these points, surface bands must intersect an odd number of times a generic Fermi energy lying within the bulk topological gap, as observed. On the other hand, $\pi(\bar{X}) = \pi(\bar{R})$, such that surface states along this path do not connect bulk valence and conducting states. Lastly, the odd number of intersections should occur also along $\bar{R} - \bar{Z}$, but on this path the bulk state projections overlap, such that the surface gap closes.

Finally, Fig. 3.2b shows the spectral density associated with the [001] surface. While the projected bulk valence and conducting bands leads to a closing of the surface gap, a pair of Dirac cones are visible at \bar{X} , consistent with having $|C_{\mathcal{M}}| = -2$.

3.4 Tight-binding models

Having established that Pt_2HgSe_3 and Pd_2HgSe_3 simultaneously realize weak and topological crystalline phases, we will now introduce tight-binding models that capture the essential topological features of this class of materials, which has been found to also include Bi_2TeI [126, 127], Bi_2TeBr [128], BiTe [129] and BiSe [103]. Specifically, we will construct systems with three-fold rotation symmetry, which are both WTI and TCI⁵. Our models consist of two coupled strong 3D TIs, a construction similar to the so called “double strong TI” of Ref. [72]. Each strong TI is defined on a triangular lattice with Bravais vectors $\mathbf{a}_1 = (1, 0, 0)$, $\mathbf{a}_2 = (-1/2, \sqrt{3}/2, 0)$, and $\mathbf{a}_3 = (0, 0, 1)$, as shown in Fig. 3.3a.

⁵Strictly speaking, Bi_2TeI has a small distortion that reduces the symmetry from trigonal to monoclinic, but this distortion is usually neglected, see Ref. [127]

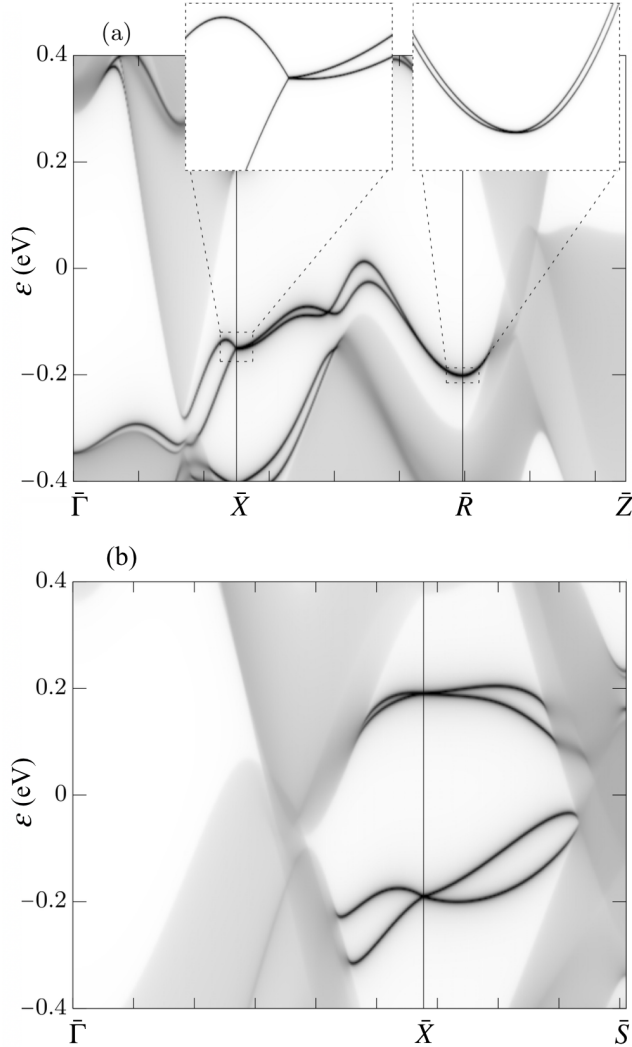


Fig. 3.2 Momentum-resolved surface spectral densities. Panel (a): [100] surface. Dirac cones associated with the weak topological index are observed at \bar{X} and \bar{R} . The insets show a zoom in on the Dirac cones. Panel (b): [001] surface. A pair of Dirac cones associated with the mirror Chern number are observed at \bar{X} .

Its momentum space Hamiltonian takes the form:

$$\begin{aligned}
 H_{\text{TI}}(\mathbf{k}) = & \Gamma_1[\mu + f(k_1, k_2) - \cos(k_3)] \\
 & + \lambda [\Gamma_2 \sin(k_1) + \Gamma_{2,1} \sin(k_2) \\
 & \quad - \Gamma_{2,2} \sin(k_1 + k_2) + \Gamma_3 \sin(k_3)].
 \end{aligned} \tag{3.2}$$

Here, $\mathbf{k} = (k_1, k_2, k_3)$ is the crystal momentum vector, where $k_j = \mathbf{k} \cdot \mathbf{a}_j$. The matrices $\Gamma_1 = \tau_z \sigma_0$, $\Gamma_2 = \tau_x \sigma_x$, and $\Gamma_3 = \tau_y \sigma_0$, where Pauli matrices τ encode

the degree of freedom associated with two orbitals per site, whereas Pauli matrices σ parametrize the spin degree of freedom. Further, the matrices $\Gamma_{2,1}$ and $\Gamma_{2,2}$ are obtained from Γ_2 by applying a three-fold rotation around the z axis:

$$\Gamma_{2,j} = C_3^j \Gamma_2 C_3^{-j}, \quad C_3 = \tau_0 \exp\left(i \frac{\pi}{3} \sigma_z\right). \quad (3.3)$$

The scalar function $f(k_1, k_2)$ encodes the in-plane hoppings of the model, and for Eq. 3.2 to describe a strong TI, it must be such that the system presents band inversions at an odd number of TRIMs. In the following we consider two specific examples of $f(k_1, k_2)$ that will allow us not only to describe the topology of Jacutingaite but also to connect with other materials predicted to be both WTI and TCI [126, 129]. The function is such that H_{TI} has either one band inversion at $\mathbf{k} = (0, 0, 0)$, or a total of three band inversions at $(0, \pi, 0)$, $(\pi, 0, 0)$, and $(\pi, \pi, 0)$. The resulting functions are:

$$f^{(\Gamma)} = - \sum_{j=0}^2 \cos(C_3^j k_1), \quad (3.4)$$

$$f^{(X)} = \frac{3}{8} \sum_{j=0}^2 \cos(2C_3^j k_1) [\cos(C_3^{j+1} k_1) + \cos(C_3^{j+2} k_1) - 2], \quad (3.5)$$

where C_3 denotes the action of a three-fold rotation on a momentum component: $C_3 k_1 = k_2$ and $C_3 k_2 = -k_1 - k_2$.

For both choices of $f(k_1, k_2)$, the Hamiltonian Eq. (3.2) obeys an inversion symmetry $I = \tau_z \sigma_0$, time-reversal symmetry $T = i\tau_0 \sigma_y K$ with K complex conjugation, as well as the three-fold rotation symmetry C_3 of Eq. (3.3):

$$C_3^\dagger H_{\text{TI}}(k_1, k_2, k_3) C_3 = H_{\text{TI}}(k_2, -k_1 - k_2, k_3). \quad (3.6)$$

Its topological structure is determined by the values of μ and λ . For both $f^{(\Gamma)}$ and $f^{(X)}$, setting $\mu = 3$ and $\lambda = 1$, the model realizes a strong 3D TI with \mathbb{Z}_2 indices $(\nu_0; \nu_1 \nu_2 \nu_3) = (1; 000)$.

Crucially, the model Eq. (3.2) is also mirror symmetric. There exists a mirror symmetry on the $k_1 = -2k_2$ plane of the BZ, $M_1 = i\tau_0 \sigma_x$,

$$M_1^\dagger H_{\text{TI}}(k_1, k_2, k_3) M_1 = H_{\text{TI}}(k_1, -k_1 - k_2, k_3), \quad (3.7)$$

as well as two other mirror symmetries obtained through rotation, $M_2 = C_3^{-1} M_1 C_3$ and $M_3 = C_3^{-2} M_1 C_3^2$, with mirror planes $k_2 = -2k_1$ and $k_1 = k_2$, respectively.

On each mirror-invariant plane, H_{TI} can be block-diagonalized into sectors corresponding to mirror eigenvalues $\pm i$. By computing the Chern number associated with each sector, Eq. (3.1), we find a mirror Chern number $C_{\mathcal{M}} = -1$ on each of the mirror planes. As such the tight-binding model of Eq. (3.2) is simultaneously a strong 3D TI and a TCI.

We will follow our construction of a dual WTI and TCI Hamiltonian using the case $f = f^{(\Gamma)}(k_1, k_2)$, for which the Hamiltonian takes the form used in Ref. [104] and hosts a single Dirac cone on each surface of the system, positioned at the $\bar{\Gamma}$ point of the surface BZ. Similar steps are presented in Apps. 3.7 and 3.8 for the case defined by Eq. (3.5). We consider two copies of H_{TI} which are displaced relative to each other by half of a unit cell in the z direction [143]. The full momentum space Hamiltonian is an 8×8 matrix having the block form

$$H(\mathbf{k}) = \begin{pmatrix} H_{\text{TI}}(k_1, k_2, k_3) + \varepsilon & \alpha A(k_1, k_2) \\ \alpha A(k_1, k_2) & H_{\text{TI}}(k_1, k_2, k_3 + \pi) - \varepsilon \end{pmatrix}, \quad (3.8)$$

where ε is a relative energy shift between the two TI blocks, $A(k_1, k_2)$ is a coupling term (to be defined later), and α is its strength.

For $\alpha = 0$, the Hamiltonian Eq. (3.8) is a block-diagonal double strong TI which obeys the same symmetries as H_{TI} . Time-reversal, inversion, rotation, as well as the three mirror symmetries have the same matrix structure in τ and σ space, and are block-diagonal in the space of the two 3D TIs. There are now, however, two band inversions in total. The upper block contributes a band inversion at $\mathbf{k} = 0$, as discussed before, whereas the lower one has inverted bands at $\mathbf{k} = (0, 0, \pi)$, due to the extra momentum shift. As such, the parity invariants associated with Eq. (3.8) are identical to Pt_2HgSe_3 , $\delta(\Gamma) = \delta(Z) = -1$, marking it as a WTI with \mathbb{Z}_2 indices $(\nu_0; \nu_1 \nu_2 \nu_3) = (0; 001)$. A [100] surface will exhibit two surface Dirac cones, one at $k_z = 0$ and one at $k_z = \pi$, protected by time-reversal and translation along z .

By combining two TI blocks, we have obtained a system with a trivial strong index, $\nu_0 = 0$, due to the latter's \mathbb{Z}_2 classification. Mirror Chern numbers, on the other hand, have an integer classification, which means that the Hamiltonian Eq. (3.8) is also a TCI with mirror Chern numbers given by the sum of the invariants in each block. We find $C_{\mathcal{M}} = -2$ on each of the three mirror planes, reproducing the behavior of Pt_2HgSe_3 and Pd_2HgSe_3 . Due to this dual topology, H will exhibit surface Dirac cones not only on its side surfaces, but on the top,

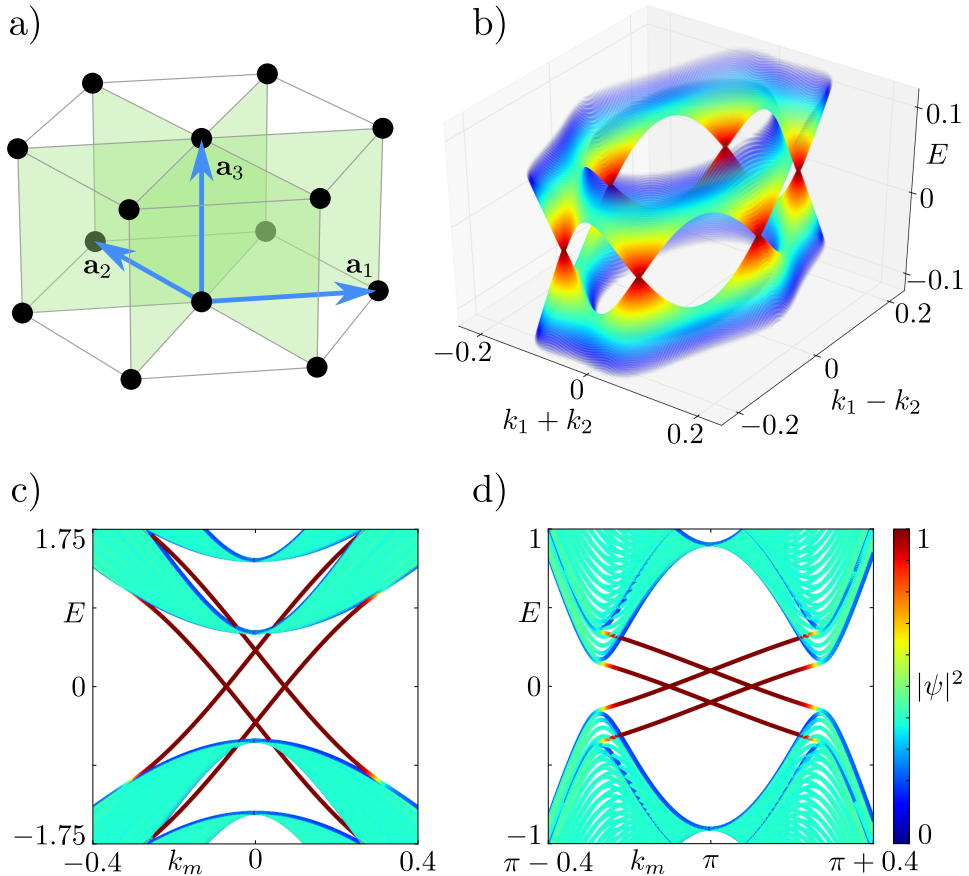


Fig. 3.3 Panel (a): Triangular lattice model of H_{TI} , Eqs. (3.2) and (3.4). Sites are shown in black, hoppings in gray, and mirror planes as shaded areas. The blue arrows represent Bravais vectors $\mathbf{a}_{1,2,3}$. Panel (b): Bandstructure of the model defined by Eqs. (3.8) and (3.4) computed in a slab geometry. Only states on the top surface are shown. Panel (c): Cut of the same bandstructure along the $k_1 = k_2$ mirror plane, with k_m labeling the momentum along the mirror plane. Panel (d): Bandstructure for model defined by Eqs. (3.8) and (3.5), along the same $k_1 = k_2$ mirror plane. All bandstructures are obtained in a slab geometry with hard wall boundary conditions perpendicular to \mathbf{a}_3 and a thickness of 40 unit cells. In (b) and (c) we set $\mu = 3$, $\lambda = 1$, $\alpha = 5$, and $\varepsilon = 0.4$, whereas $\varepsilon = 0.1$ in panel (d). The color scale in panels (c) and (d) denotes the integrated probability density of wavefunctions on the top- and bottom-most 8 sites of the slab, such that surface modes appear in red (dark gray) and bulk modes in light green (light gray).

[001] surface as well. For $\alpha = 0$, there are two surface Dirac cones positioned at the $\bar{\Gamma}$ point of the surface BZ and at energies $\pm\varepsilon$.

As long as the two TI blocks remain uncoupled, the surface Dirac cones are orthogonal to each other, such that a circular band crossing occurs at $E = 0$

whenever $\varepsilon \neq 0$. This band crossing, however, is an artifact of the block-diagonal nature associated with the choice $\alpha = 0$. For $\alpha \neq 0$, the two TI blocks couple, lifting the degeneracy. We choose an off-diagonal coupling term $A(k_1, k_2) = \tau_x \sigma_z \sum_{j=0}^2 \sin(C_3^j(k_1 - k_2))$ which preserves time-reversal, inversion, as well as rotation and mirror symmetries. Due to this term, the circular band crossing is lifted everywhere except on the three mirror planes. The result is that the [001] surface now hosts a total of six Dirac cones. On each of the three mirror planes there exists a pair of Dirac cones positioned symmetrically around $\bar{\Gamma}$ due to time-reversal symmetry, as shown in Fig. 3.3b for a slab geometry calculation. Their position can be tuned with the relative energy shift of the two TI blocks, ε .

Fig. 3.3c shows the bandstructure along a mirror plane in a larger energy scale. Notice that the branches of the two $E = 0$ Dirac cones positioned symmetrically around $\bar{\Gamma}$ can intersect at the TRIM giving rise to a second pair of Dirac cones. In a given material, details of the bulk bandstructure and of the surface potential will dictate if all or some of these four Dirac cones are observed. For instance, DFT calculations in Bi_2TeI [126] have highlighted Dirac cones both at $\bar{\Gamma}$ and away from the TRIM, and similar results are found in Bi_2TeBr [128] and in BiTe [129]. Different to these materials, Jacutingaite has two observable surface Dirac cones at \bar{X} (see Fig. 3.2b), while the possible Dirac cones away of the TRIMs are hidden by the projection of the bulk spectral density. This scenario is better described by Hamiltonian Eq. 3.8 with the choice $f(k_1, k_2) = f^{(X)}$. In this case, as Fig. 3.3d depicts, the Dirac cones are positioned closer to and symmetrically with respect to $(\pi, \pi, 0)$.

3.5 Conclusion

We have shown that the naturally occurring and recently synthesized Pt_2HgSe_3 and Pd_2HgSe_3 belong to the class of systems that simultaneously realize weak and topological crystalline phases. In addition, we have introduced a set of tight-binding models that contain the essential properties of this dual topological phase, reproducing the main features of the surface spectral densities which have been predicted for different materials in the class.

We note that, similar to elemental bismuth [104], these topologically non-trivial materials are not insulators, but semimetals with small electron and hole pockets. Since they lack a bulk mobility gap, it is unlikely that they will show surface dominated transport, due to the fact that disorder, which is unavoidable

in any realistic setup, will scatter surface electrons into the bulk. However, the systems we have studied have well defined topological gaps throughout their BZ, meaning that weak and strong \mathbb{Z}_2 topological indices as well as mirror Chern numbers can be meaningfully computed. These invariants necessarily lead to surface states in the energy range defining the topological gap, shown in Section 3.3, which may be visualized using energy and/or momentum sensitive techniques, such as angle-resolved photo-emission spectroscopy, or scanning tunneling spectroscopy. Thus, we hope that our work will motivate experimental studies on Jacutingaite, aimed at probing the topology of its surface modes.

Further, we hope that the tight-binding models we have introduced will allow for a better theoretical understanding of WTI+TCI materials. These include the behavior of the system under various surface perturbations, for which it can become a HOTI [103], the behavior of modes localized to step edges, which have recently been reported in Bi_2TeI [127], as well as the effect of disorder. Moreover, they may be used to understand the degree to which surface modes can influence transport properties in the presence of coexisting bulk states, similar to the studies done for 2D systems in Refs. [144, 145].

3.6 Appendix A:Ab-initio results for Pd_2HgSe_3

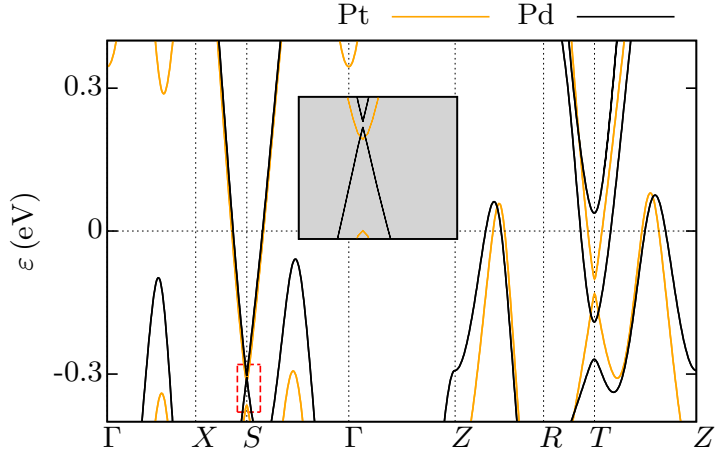


Fig. 3.4 Bandstructure of Pd_2HgSe_3 and of Pt_2HgSe_3 . The inset presents a zoom of the area enclosed by the red dotted-line square.

We performed Density Functional Theory (DFT) calculations for Pd_2HgSe_3 using the crystal structure reported in Ref. [130]. We used the same calculation setup as in the main text of this article. The energy dispersion of Pd_2HgSe_3 and of Pt_2HgSe_3 present the same features, as shown in Fig. 3.4. The main difference is the smaller topological gap between valence and conducting states observed in the Pd based compound. We obtained for Pd_2HgSe_3 the same parity invariants as for Pt_2HgSe_3 , and hence the same time reversal polarization invariants. Namely, $\delta(X) = \delta(R) = 1$, $\delta(\Gamma) = \delta(Z) = -1$ and $\mathbb{Z}_2 = (0; 001)$.

We also built a tight-binding Hamiltonian for Pd_2HgSe_3 based on Wannier functions associated with orbitals $6s$, $6p$ and $5d$ of Hg, $5s$, $5p$ and $4d$ of Pd and $4p$ of Se and used this Hamiltonian for computing surface spectral densities. Fig. 3.5(a) presents the spectral densities at the surface [100]. While surface Dirac cones are visible at \bar{X} and \bar{R} , the projection of the bulk bands closes the surface gap between surface time-reversal invariants momenta of different surface parity invariant, and hence, does not allow us to analyze the connectivity between the surface Dirac cones and bulk valence and conduction states. Fig. 3.5(b) shows the spectral density associated with the surface [001] which, as in Pt_2HgSe_3 , features two Dirac cones at \bar{X} .

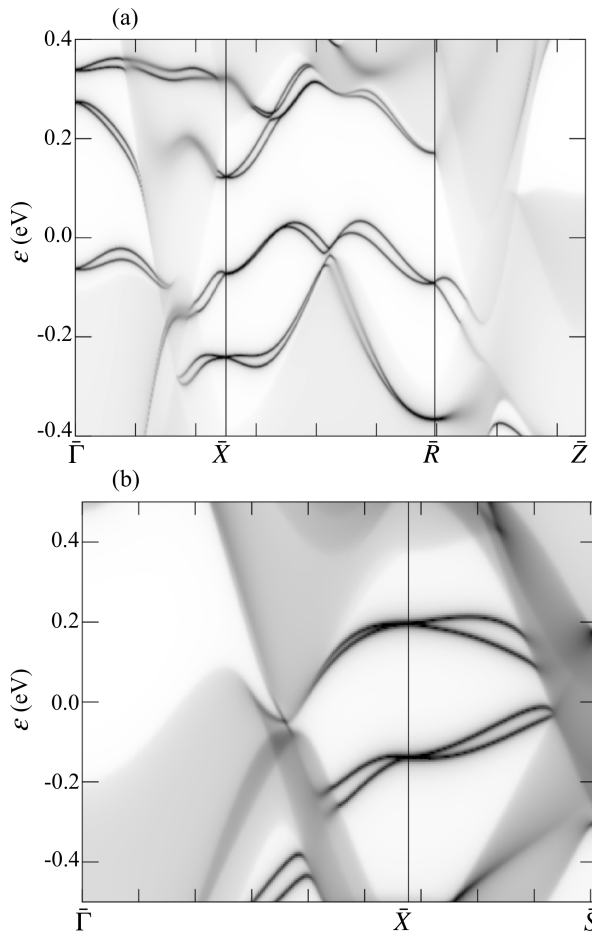


Fig. 3.5 Momentum-resolved surface spectral densities of Pd_2HgSe_3 . Left: [100] surface. Right: [001] surface. A pair of Dirac cones associated with the mirror Chern number are observed at \bar{X} .

3.7 Appendix B: Different surface Dirac cone positions

As explained in the main text, the [001] surface spectral density of Pt_2HgSe_3 presents two Dirac cones at \bar{X} (and at the other TRIMs connected to \bar{X} by $2\pi/3$ rotations). Within the 8-band tight-binding models considered in this work, this surface spectral density is better described by the model which presents band inversions at the boundaries of the 3D BZ, such that $\delta(X) = \delta(R) = -1$ and $\delta(\Gamma) = \delta(Z) = +1$. These parity invariants differ in a global sign with those computed with FPLO, but as the comparison with the VASP calculations shows,

they coincide with the ab-initio results when the parity invariant calculation is constrained to the energy windows $[-17.5, 0]$ eV.

In the following, we reformulate the construction presented in the main text for this case. We follow the same strategy, namely to start with two 3D TI blocks. However, unlike H_{TI} of Eq. (2) in the main text, which had a single band inversion at Γ , we choose a TI block which has a total of three band inversions, positioned at the three X points of the BZ. For the TI Hamiltonian presented in the main text, Eq. (3.2), we now focus on the case in which the function $f(k_1, k_2)$ is

$$\begin{aligned} f(k_1, k_2) = f^{(X)}(k_1, k_2) = & \frac{3}{8} \left\{ \cos(2k_2) \left[-2 + \cos(k_1) + \cos(k_1 + k_2) \right] \right. \\ & + \cos(2k_1) \left[-2 + \cos(k_2) + \cos(k_1 + k_2) \right] \\ & \left. + \cos(2(k_1 + k_2)) \left[-2 + \cos(k_1) + \cos(k_2) \right] \right\}. \end{aligned} \quad (3.9)$$

In the next section, we detail the real-space structure of these hopping terms. Due to the form of Eq. (3.9), H_{TI} obeys the same symmetries as the TI model introduced in the main text: time-reversal, inversion, three-fold rotation, as well as the three mirrors. Setting as before $\mu = 3$ and $\lambda = 1$, the model realizes a simultaneous strong TI with \mathbb{Z}_2 indices $(\nu_0; \nu_1 \nu_2 \nu_3) = (1; 000)$ and TCI with mirror Chern numbers $C_{\mathcal{M}} = -1$ on each of the three mirror planes. Crucially however, there are now three band inversions in the model, occurring at $(k_1, k_2, k_3) = (\pi, 0, 0)$, $(0, \pi, 0)$, and $(\pi, \pi, 0)$, such that the $[001]$ surface hosts a total of three Dirac cones, positioned at the \bar{X} points of the surface BZ. By forming a double strong TI as in Eq. (3.8), we obtain a dual topological phase, which is simultaneously a WTI and a TCI with $C_{\mathcal{M}} = -2$. Figure 3.6 shows the bandstructure of the model in a slab geometry, infinite in both k_1 and k_2 and with a thickness of 40 unit cells in the z direction.

3.8 Appendix C:Real-space hopping terms

The real-space structure of the Hamiltonian H_{TI} of Eq. (3.2) together with the function $f^{(\Gamma)}$ of Eq. (3.4) are the same as in Ref. [103]. For the model with three band inversions at the X points, however, the momentum-space function $f^{(X)}$ of Eq. (3.9) leads to longer ranged, in-plane hoppings in real space. These hoppings,

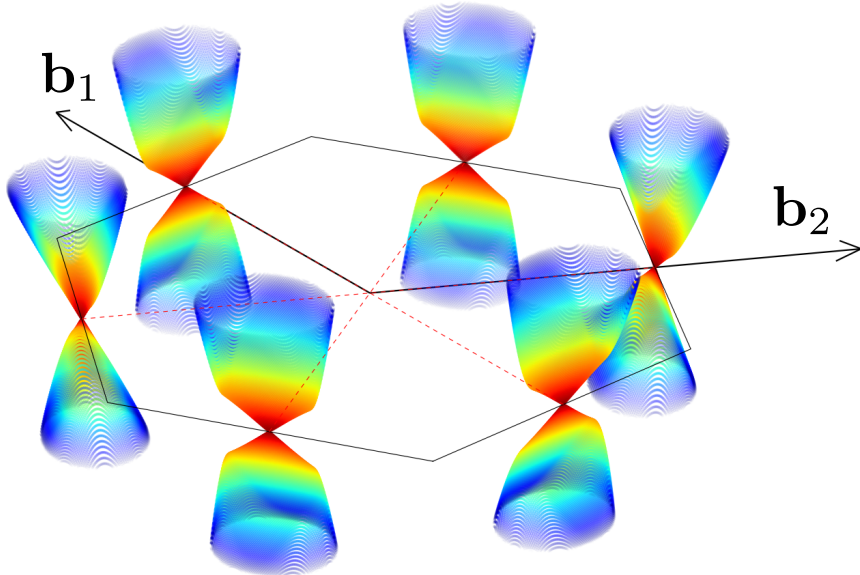


Fig. 3.6 Bandstructure of the model obtained using Eq. (3.9) in an infinite slab geometry, with thickness of 40 unit cells in the z direction, using $\mu = 3$ and $\lambda = 1$. Only states which are localized on the top surface and have energies $|E| \leq 1$ are shown. To better visualize the surface Dirac cones, we set $\alpha = \varepsilon = 0$, such that each Dirac cone is doubly degenerate. The hexagonal contour marks the boundary of the surface BZ, mirror invariant lines are shown in dashed red, and black arrows indicate the reciprocal lattice vectors of the surface $\mathbf{b}_1 = (\sqrt{3}/2, 1/2)$ and $\mathbf{b}_2 = (0, -1)$.

which all have the same matrix structure, $\Gamma_1 = \tau_z \sigma_0$, are shown schematically in Fig. 3.7. Their amplitudes are $t_1 = -3/8$, $t_2 = 3/16$, and $t_3 = 3/32$.

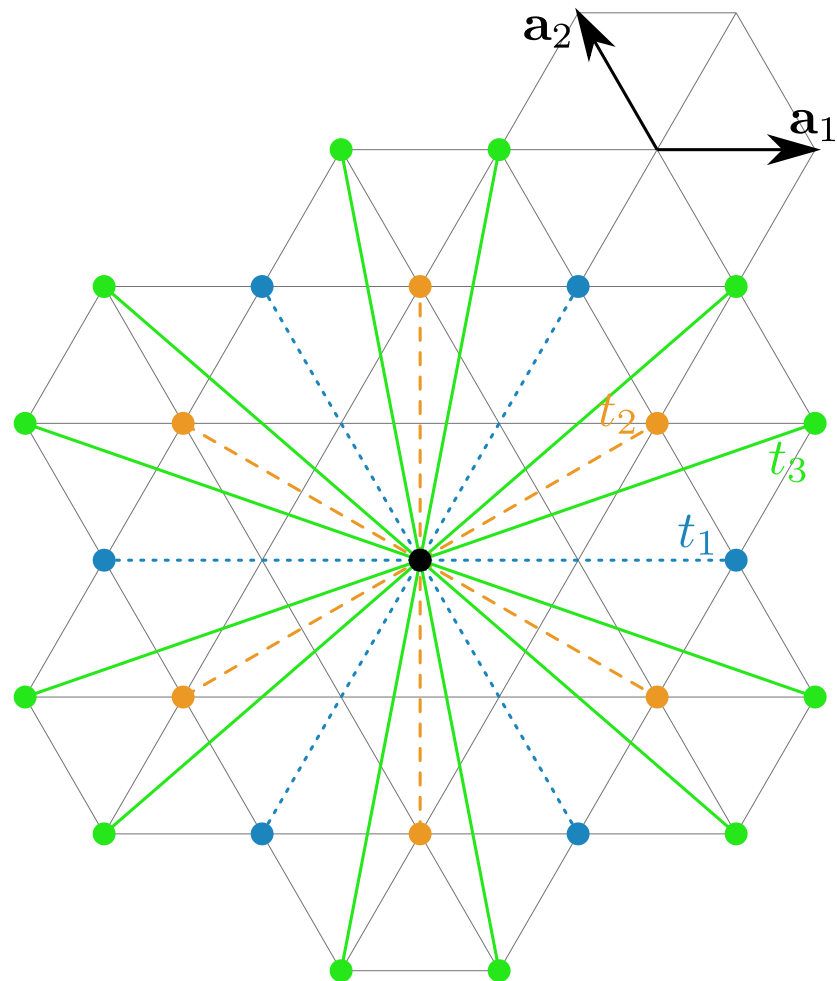


Fig. 3.7 Sketch of the real-space hopping terms corresponding to the function $f^{(X)}$ of Eq. (3.9). Shown is the triangular lattice describing H_{TI} at constant z coordinate. Starting from a site on The hopping amplitudes are $t_1 = -3/8$ (blue dotted lines), $t_2 = 3/16$ (orange dashed lines), and $t_3 = 3/32$ (green solid lines). The structure of the hoppings preserves the three-fold rotation symmetry of the model.

Chapter 4

Hinge electronic structure of strained half-Heuslers

4.1 Introduction

Low-dimensional boundaries of a system, such as hinges and corners, can host interesting electronic properties as recently uncovered by the discovery of higher-order topological insulators (HOTIs) and of higher-order quantized electric multipole moments. [146–150, 70, 151–153]. In three dimensions, a second order topological insulator is characterized by an insulating bulk, insulating surfaces and metallic hinges. Elementary Bi has been found to offer a material realization of such phase when crystals are cut preserving the bulk trigonal symmetry [70, 154]. Classifications of symmetry-protected HOTI phases have been performed [155–158] and the study of hinge states in a plethora of platforms is nowadays very active [159–163].

The possibility of hinge states in gapless semimetals has also been recognized [164–167] and the quest for specific materials where to study them is naturally important. Ref. [166] showed the existence of hinge states in models relevant for various candidate Dirac semimetals, such as Cd_3As_2 and KMgBi . Ref. [168] argued about the importance of hinge states in $\beta\text{-MoTe}_2$ for the interpretation of its surface electronic structure while Ref. [169] reported evidence of hinge states in the related compound WTe_2 .

Recently, it has been suggested the possibility of HOTI phases in the broad set of half-Heusler (hH) compounds [170]. Half-Heuslers are ternary compounds with the space group (SG) No. 216 [171–173]. They present at low energy a very

similar electronic structure to that of CdTe or HgTe, the latter one a reference example of nontrivial electronic topology since the first predictions [25, 174] and experimental confirmation [175, 176] of hosting a topological insulating phase under strain. The richness of HgTe goes hand in hand with the simplicity of its band structure, the hallmark of which is an inversion between the so-called Γ_6 and Γ_8 bands [177]. In the cubic phase, the Γ_8 bands exhibit a fourfold crossing at low energies which enforces a semimetallic phase. An appropriate reduction of the symmetry opens a gap, yielding a strong topological insulator (TI).

The additional atom in the unit cell of hHs can serve different purposes, such as providing a knob to change the unit-cell volume, which in turn reflects on the electronic structure, or stabilizing various long-range ordered phases [178], making hHs an interesting platform to explore the interplay between such diversity and topological properties of the electronic structure. This potential naturally motivated extensive *ab initio* computational searches [179–181] that yielded as a result the identification of dozens of band-inverted Hhs, namely compounds in which the bands follow the hierarchy $\varepsilon_{\Gamma_8} > \varepsilon_{\Gamma_6}$, some of which were experimentally confirmed [182, 183]. Later, the possibility of realizing the Weyl semimetal phase in different members of the class further enriched the prospects of non-trivial topology in hHs. This was shown in studies that considered different mechanisms that act to reduce the cubic symmetry, including magnetic fields [184–186] or uniaxial strain [187]. These axial perturbations break the three-fold rotational symmetries that protect the fourfold crossing of the Γ_8 bands [188], opening a gap in these bands and eventually leading to the creation of Weyl nodes.

The above-mentioned suggestion of HOTI phases in hHs is based on a study of a four-band model reasonably accurate to describe the Γ_8 bands [170]. In this work, we investigate the problem by means of density-functional theory (DFT) calculations and of ab-initio derived tight-binding models. Our calculations show the existence of electronic states on certain hinges of hHs with either $\varepsilon_{\Gamma_8} > \varepsilon_{\Gamma_6}$ or with $\varepsilon_{\Gamma_8} < \varepsilon_{\Gamma_6}$. Importantly, we find these hinge states to be topologically trivial. Further, we show that they are critically affected by the topology of the bulk electronic structure due to trivial hybridization effects: topological surface states, when present, hybridize with the hinge modes which, as a consequence, avoid being exponentially localized around the hinges.

This paper is organized as follows. In Sec. 4.2, we describe methodological aspects of this work. In Sec. 4.3, we present the bulk and surface electronic structure of the lithium-based half-Heusler compounds LiBiZn and LiSbZn. In Sec. 4.4, we discuss relevant Hamiltonians that describe the low energy electronic properties of these compounds and in Sec. 4.5 we present hinge band structure calculations. Sec. 4.6 contains our concluding remarks. The Appendix. 4.7 provides 8-band tight-binding Hamiltonians suitable to describe LiBiZn and LiSbZn.

4.2 Methods

Density functional theory (DFT) calculations were performed with the FPLO code [189] version 18.57, treating the spin-orbit coupling in the fully-relativistic four-component formalism and performing numerical Brillouin zone integrations with the tetrahedron method using a mesh of $30 \times 30 \times 30$ subdivisions. We relaxed the crystal structure by minimization of the total energy. For the simulation of uniaxial strain, we fixed the deformation of the lattice parameter c , and relaxed the perpendicular lattice parameters under the constraint $a = b$. To parametrize the deformation, we define $\delta = (c_0 - c)/c_0$, where c_0 is the equilibrium lattice parameter.

Starting from the DFT results, tight-binding models were obtained by construction of Wannier functions with the projective method as implemented in FPLO. Based on the analysis of the orbital-projected density of states, we consider an eight band model that includes Bi-6p (or Sb-5p) and Zn-4s orbitals. These tight-binding models were used for the study of the electronic structure at surfaces and hinges. For the former, we considered semi-infinite slabs using the PYFPLO module of the FPLO code, while for the latter we solved finite systems using own codes based on Kwant [76] (more details are presented in Section 4.5).

4.3 Lithium half-Heuslers

The crystal structure of a hH compound of formula XYZ can be regarded as two displaced zinc-blende lattices formed by XZ and YZ pairs of atoms (Fig. 4.1a). With this notation, X and Y occupy the crystallographically equivalent sites $4a$

and $4b$, forming a rock salt structure, while Z is positioned at the site $4c$. We will consider the cases $X=\text{Li}$, $Y=\text{Bi}$ or Sb and $Z=\text{Zn}$.

We choose Li-based hHs because, as we will show, their simplicity facilitate the construction of low-energy tight-binding models that accurately reproduce the density-functional calculations with a minimum effort in terms of number of bands. This allow us to tackle the problem of studying the hinge electronic structure using realistic tight-binding Hamiltonians.

While both LiSbZn and LiBiZn have originally been studied in the hexagonal phase [190, 191], the former has also been grown in the cubic phase [192] and the latter has recently been predicted to present a cubic phase as ground state [193]. We notice that within the same cubic space group, there are two variants defined by the crystallographic site occupied by the Zn atoms. In particular, in the family LiZnT ($T=\text{N, P, As}$), the Zn atoms are found in the Y position. On the other hand, Ref. [192] has shown that the compound LiSbZn is different, since Zn occupies the Z position. We have compared the total energy of these two variants for LiBiZn and LiSbZn , obtaining that the structure with Zn in the Z site has lower energy. We notice that for both structures the Bi and Zn atoms — which provide the dominant contribution near the Fermi energy, as will be shown below — form a zinc-blende lattice and therefore, both variants have similar low-energy band structures.

We obtain for the fully relaxed compounds the lattice parameters $a = 6.584 \text{ \AA}$ for LiBiZn and $a = 6.350 \text{ \AA}$ for LiSbZn . Figures 2 (c) and (d) show the band structure and the orbital-projected density of states $D(\varepsilon)$ of LiBiZn and of LiSbZn , respectively. In both cases, $\text{Bi-}6p$ or $\text{Sb-}5p$ states dominate the electronic structure in the energy windows shown and exhibit a substantial hybridization with $\text{Zn-}4s$ and $\text{Li-}2s$. The main difference between compounds is the relative position of the Γ_6 and Γ_8 bands, which accommodate in total four electrons per unit cell. In LiSbZn , the energies of these bands obey $\varepsilon_{\Gamma_8} < \varepsilon_{\Gamma_6}$, so that the Γ_8 bands are completely filled and the compound is an insulator. In LiBiZn , the opposite arrangement leads to half-filled Γ_8 bands, enforcing a semimetallic state. In this case, a clear $s-p$ inversion is noticeable near Γ . In Appendix 4.7 we present an eight-band tight-binding model suitable to describe both compounds. An analysis of the model parameters indicates that the main difference between compounds is the larger local spin-orbit coupling in the Bi-based compound. Thus, these compounds having $\varepsilon_{\Gamma_8} > \varepsilon_{\Gamma_6}$ (LiBiZn) or $\varepsilon_{\Gamma_8} < \varepsilon_{\Gamma_6}$ (LiSbZn) provide a framework for the study of the hinge electronic structure of both band-inverted

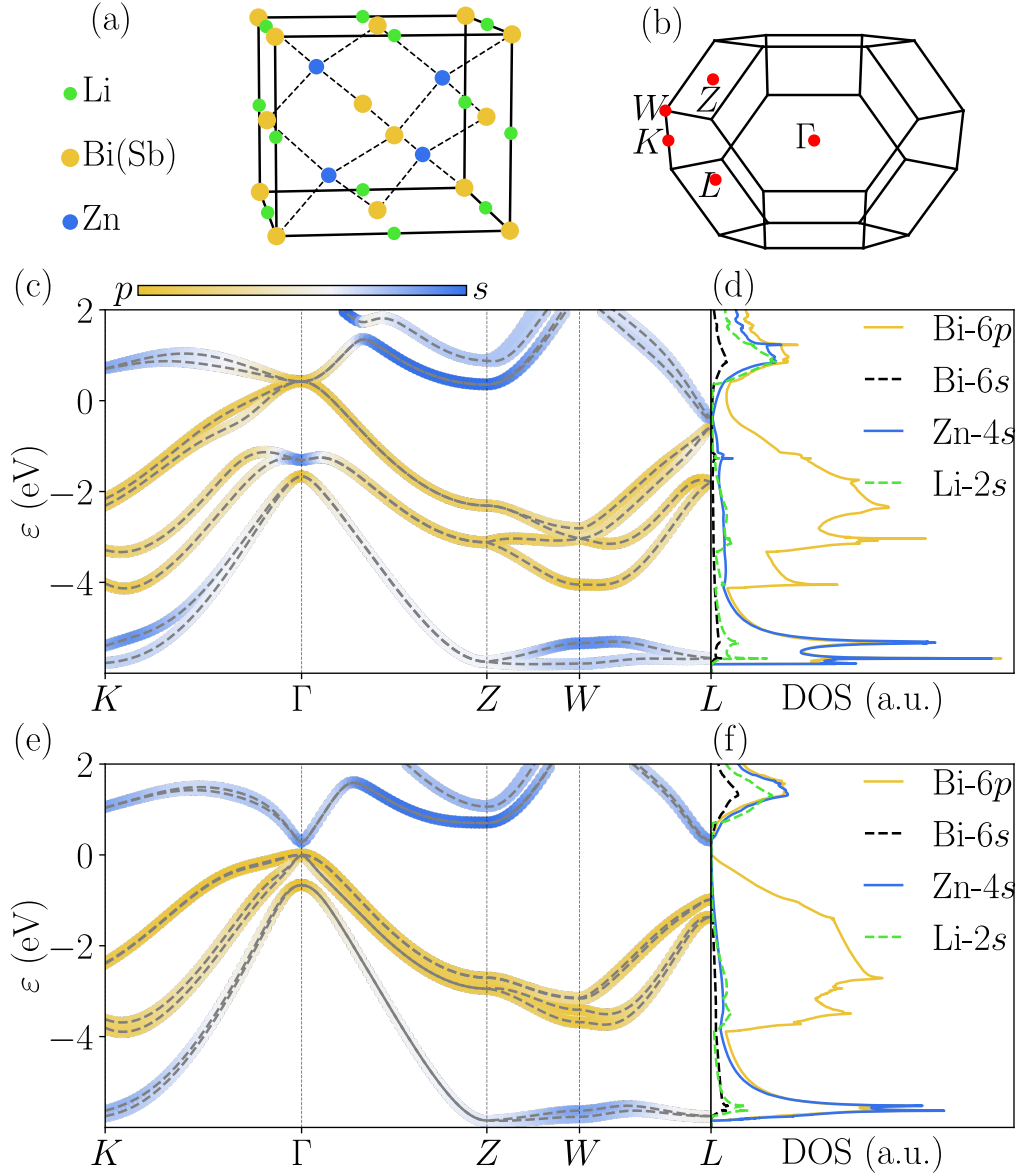


Fig. 4.1 (a) Crystal structure. (b) Brillouin zone. (c,d) Band structure and density of states of LiBiZn and LiSbZn, respectively. The weight associated with Bi-6p (or Sb-5p) is depicted in orange while that of Zn-4s, Bi-6s (or Sb-5s) and Li-2s in blue.

and normal systems having very similar chemical and physical properties (e.g. lattice parameters and orbital composition of low-energy bands).

The fourfold crossing present at Γ_8 is protected by the threefold rotation symmetries along the unit-cell diagonals [188]. Therefore, perturbations that reduce the cubic symmetry will generically gap out this crossing. Here we consider the case of uniaxial strain along the \hat{z} direction, either compressing

(negative δ in our convention) or stretching the system. Under such perturbations, the crystal symmetry becomes $\bar{I}\bar{4}m2$ (SG 119). Figures 4.2 (a) and (b) show the band structures of LiBiZn near Γ corresponding to $\delta = 0, \pm 0.02$. For both signs of δ , we find that the Γ_8 bands remain gapless in a wide range of strain $-0.04 < \delta < 0.04$. For $\delta < 0$, a Dirac cone along ΓZ closes the gap. For $\delta > 0$, Weyl nodes closing the gap are found in the $k_z = 0$ plane. Similarly, in LiSbZn strain opens a gap at the fourfold crosssing. In this case, the system remains insulating with only a weak change in fundamental gap formed between the Γ_8 and Γ_6 bands (not shown).

Lastly, we notice the existence of planes defined by three of the time-reversal invariant momenta (more details in Section 4.4) which present for finite strain a well defined gap in the full Brillouin zone for any sign of strain and have a nontrivial \mathbb{Z}_2 index. Thus, for finite δ the electronic structure is characterized by either Weyl or Dirac points which close the gap of the Γ_8 bands, but which coexist with two-dimensional planes that realize quantum spin Hall insulating (QSHI) phases.

To conclude this Section, we briefly present how these properties influence the surface spectral features. We focus on LiBiZn and consider the Zn-terminated [1,-1,0] surface, which is perpendicular to the direction in which strain is applied. Figures 4.3 (a) and (b) show results for $\delta = -0.02$ and $\delta = 0.02$, respectively. The path chosen includes segments perpendicular ($K\Gamma$) or parallel (ΓZ) to the direction of the strain. Surface states with Dirac cones located at the Brillouin zone border (K and Z) are observed for both signs of strain. We notice that for a LiBi-terminated surface, while the connectivity provided by the surface states between the projection of the bulk valence and conducting bands is the same, the Dirac cone at Z or K is pushed into the bulk projection (not shown). As shown in Figures 4.3 (c) and (d), the main role of strain is observed near Γ : the spectrum becomes gapped at Γ and gapless at the projection of the Dirac cone (along ΓZ and $\delta < 0$) or of the Weyl nodes (along $K\Gamma$ and $\delta > 0$).

4.4 Low energy models

The salient feature of the low energy band structure of band-inverted hHs is the seemingly quadratic touching at Γ , which involves four bands. A model that describes a quadratic fermionic band touching at an isolated point and is often invoked as relevant for hHs materials is the spin 3/2 Luttinger Hamiltonian.

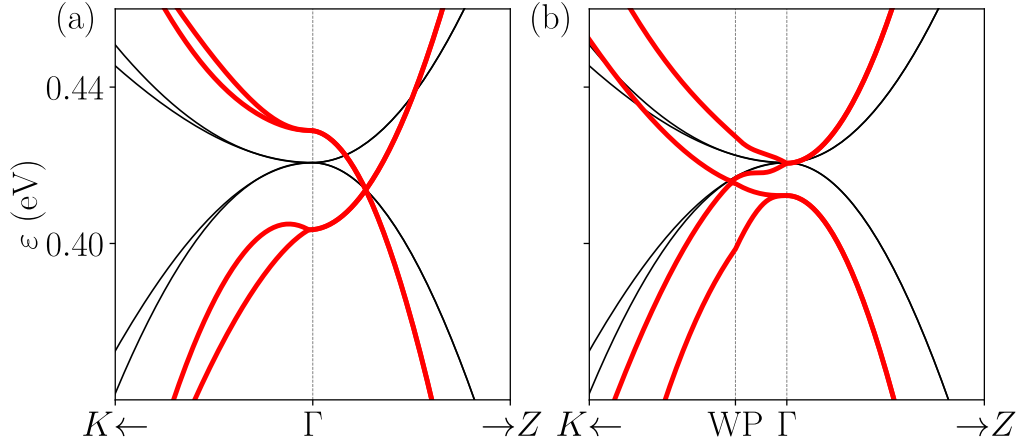


Fig. 4.2 (a) Band structure of LiBiZn under uniaxial strain $\delta = -0.02$. Thinner black curves are the bands without strain. (b) Band structure for $\delta = 0.02$. The path chosen include one of the eight Weyl nodes found in the $k_z = 0$ plane, of coordinates $\frac{2\pi}{a}(0.017, 0.006, 0)$.

This model is rooted in the $\mathbf{k} \cdot \mathbf{p}$ perturbation theory [194] and has been used for investigating, e.g., spin-Hall conductivity [195], non-Fermi-liquid topological phases [196], light-matter interaction in Weyl semimetals [197] and also superconducting pairing properties [198, 199]. More recently, the topological properties of this model have been analyzed in Ref. [170], where it was found that uniaxial strain leads to the formation of HOTI phases. Thus, it is naturally important to understand how these results apply to hHs.

Following Ref. [170], we consider the model Hamiltonian

$$\begin{aligned} \mathcal{H}(\mathbf{k}) = & t \sum_{j=1}^2 \sin(k_j a) \gamma_j \\ & + \left[-t_3 \cos(k_3 a) + m_z + t_0 \sum_{j=1}^2 [1 - \cos(k_j a)] \right] \gamma_3 \\ & \Delta_1 [\cos(k_2 a) - \cos(k_1 a)] \gamma_4 + \Delta_2 \sin(k_1 a) \sin(k_2 a) \gamma_5, \end{aligned} \quad (4.1)$$

where a is the lattice constant, $\mathbf{k} = (k_1, k_2, k_3)$ is the momentum vector, and γ_j , $1 \leq j \leq 5$, are the mutually anticommuting 4×4 Hermitian matrices satisfying the algebra $\{\gamma_i, \gamma_j\} = 2\delta_{ij}$. These can be represented as $\gamma_1 = \sigma_3 \tau_1$, $\gamma_2 = \sigma_0 \tau_2$, $\gamma_3 = \sigma_0 \tau_3$, $\gamma_4 = \sigma_1 \tau_1$, $\gamma_5 = \sigma_2 \tau_1$, where σ and τ Pauli matrices encode the spin and orbital degrees of freedom, respectively. As shown by Ref. [170], expansion of this model around Γ can be mapped to the Luttinger Hamiltonian. The model describes well the low energy dispersion of band-inverted hHs, with the caveat

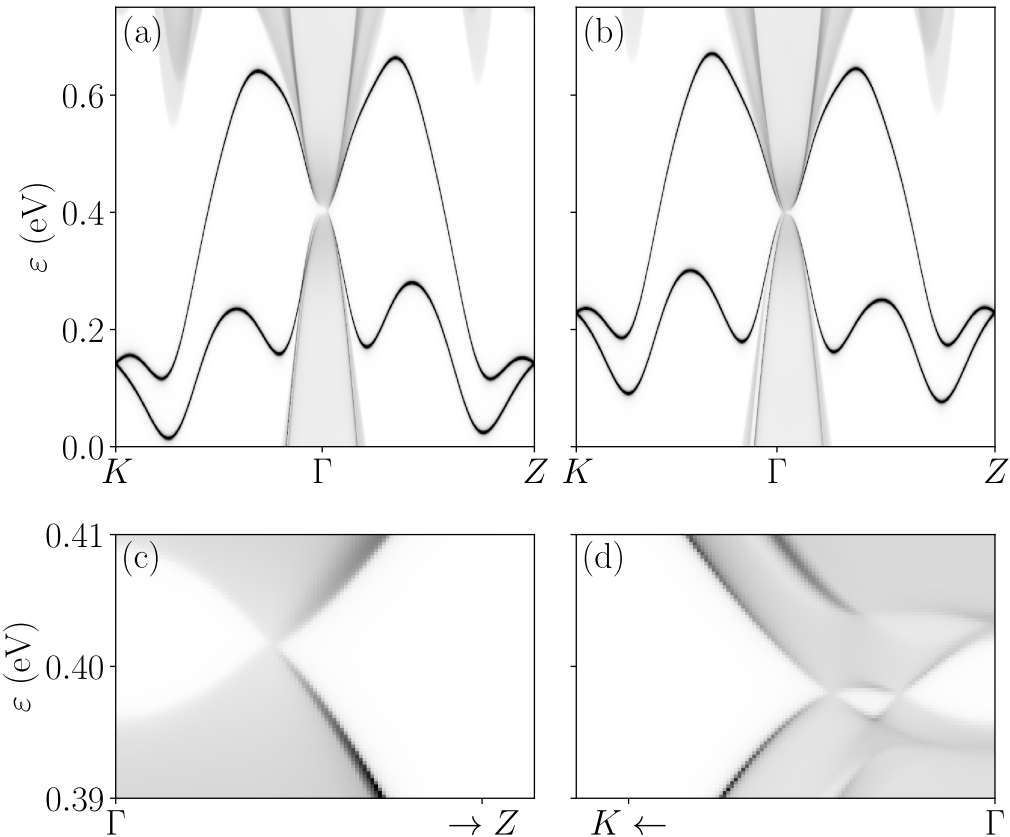


Fig. 4.3 (a) [1,-1,0] Zn-terminated surface spectral density structure of LiBiZn under uniaxial strain $\delta = -0.02$. The panel on the right is a zoom of the white square in the left panel. (b) Analogous results for strain $\delta = 0.02$. (c),(d) Zoom of the data in (a),(b), respectively. The path width in the zooms is $0.04 \times 2\pi/a$.

that additional crystal symmetries make the crossing not isolated in actual hHs. Namely, within the model, the bands split in four at any momenta infinitesimally away from Γ while in the material there are lines (e.g. Γ - X) where the bands split only in pairs [see Fig. 4.1 (c, d)]¹.

The term $\delta = (-t_3 \cos k_3 a + m_z) \gamma_3$ mimics the effects of strain along the [001] direction². Depending on the sign of δ at $k_3 = 0$, this term leads the model Eq. (4.1) to either a Dirac semimetal phase ($t_3 > m_z$), or to a stack of quantum spin Hall insulating(3D) phases ($t_3 < m_z$). Interestingly, these phases support higher-order topological modes along certain hinges [170].

¹See [188] for a demonstration that only materials in the SGs 207-214 can host fourfold crossings whose low energy description is exactly that of spin 3/2 quasiparticles.

²For consistency with our DFT results, we define δ with an opposite sign to Ref. [170].

We observe that the topological properties of the Hamiltonian Eq. (4.1) are in general different from those of hHs we consider. First, in the case of LiBiZn, the stack of QSHI phases is instead replaced by a Weyl semimetal phase, as shown in Fig. 4.3(b). Second, and more fundamental, as shown in earlier studies in HgTe [200] and also in some hHs [201], to faithfully describe not only the energy dispersion in a given energy window but also global topological properties of the full (occupied) band structure, a model for hHs must have at least six orbitals per primitive unit cell [201]. This follows from the fact that the band inversion that drives the non-trivial topology is between the quartet of bands Γ_8 and the doublet Γ_6 . The difference between the effects of strain on the model Eq. (4.1) and on a model for hHs containing six (or more) bands can be appreciated noticing that, as mentioned above for LiBiZn, band-inverted hHs have in the Brillouin zone planes which realize a QSHI phase under finite strain of *any* sign. On the contrary, in the case of the model Eq. (4.1), these planes undergo a phase transition from a QSHI to a trivial insulator as the strain changes sign.

To illustrate the difference in topology, Figs. 4.4 (a) and (b) show the Wilson loop computed in the $k_3 = 0$ plane for positive or negative strain, respectively, for the model Eq. (4.1). The different winding indicates a change in the value of the \mathbb{Z}_2 invariant for different signs of strain. On the other hand, the \mathbb{Z}_2 invariant in LiBiZn remains nontrivial independently of the sign of strain, as indicated by the evolution of the Wannier centers shown in Figs. 4.4 (c) and (d) for compressive and tensile strain, respectively. Therefore, the electronic structure of both surfaces and hinges can be very different between a system described by the model Eq. (4.1) and hHs.

4.5 Hinge electronic structure

In this section, we present hinge band structure calculations for LiBiZn and LiSbZn. These are based on tight-binding Hamiltonians associated with Wannier functions constructed from DFT calculations. As explained above, a six-band model would be the minimal option to correctly capture the topology of band-inverted hHs. However, it is problematic to obtain such a model from a Wannierization processs consisting in the projection of the Khon-Sham wave functions onto pre-defined local orbitals, essentialy because the low-energy six bands have a strong mixture of Bi-6p and s-like orbitals (primarily from Zn but also in smaller amount from Li and Bi as well). This makes the definition of the local

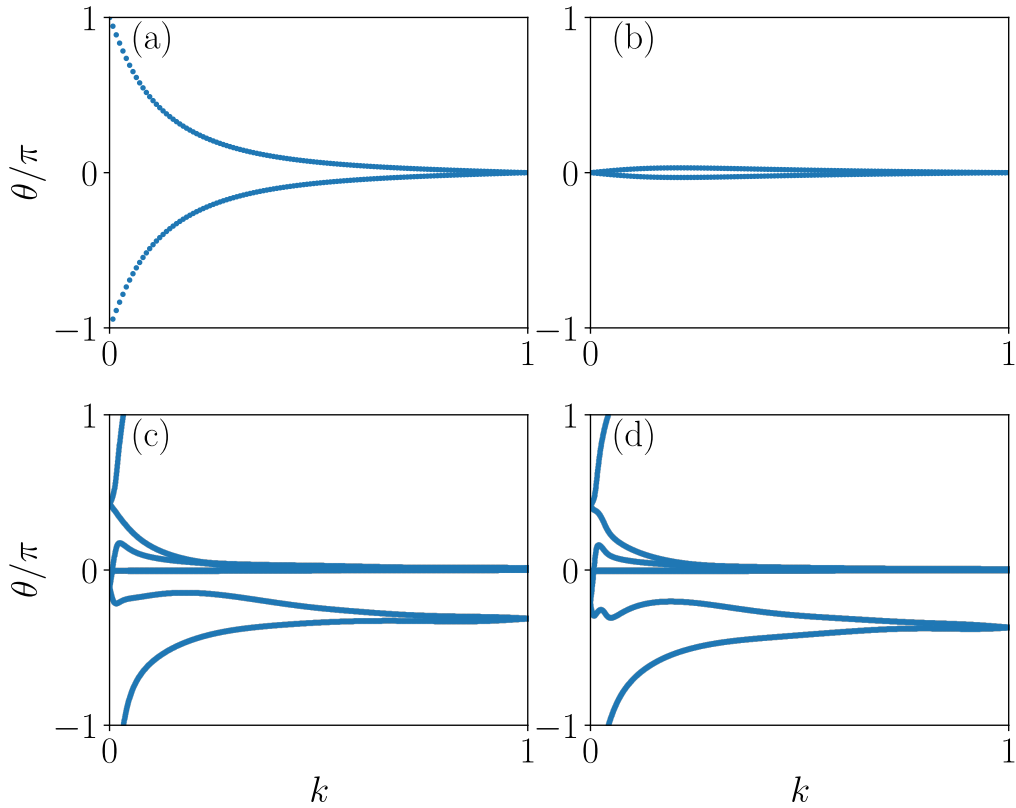


Fig. 4.4 (a) Wilson loop in the $k_z = 0$ plane for the four band model Eq. 4.1 with $\delta < 0$. (b) Same for $\delta > 0$. (c) Wannier center evolution in the plane defined by the TRIMs Γ , $\vec{G}_1/2$ and $\vec{G}_2/2$ for LiZnBi under compressive strain. (d) Same as (c) in the case of tensile strain.

orbitals onto which project unknown. Therefore, at the expense of a numerically more demanding hinge bandstructure calculation, we shall work with 8-band models including all Bi 6p (or Sb 5p) and Zn 4s orbitals, as explained in Section 4.2.

Figure 4.5 illustrates the system we consider, which is infinite along \hat{x} and finite in the two other directions. Two of the surfaces are terminated at Bi/Sb sites and the remaining two at Zn. There are three inequivalent hinges: one results from the intersection of Zn planes, one from Bi (or Sb) planes and two from the intersection of a Bi (or Sb) plane with a Zn plane. The calculations were performed for a system of size 14×14 . To study the real-space distribution of the wavefunctions, we divide the system in three regions associated with the hinges (H), the surfaces (S) and the bulk (B), as depicted in Fig. 4.5. Accordingly, we introduce the weight functions $w_H(k_x, n)$, $w_S(k_x, n)$ and $w_B(k_x, n)$ which

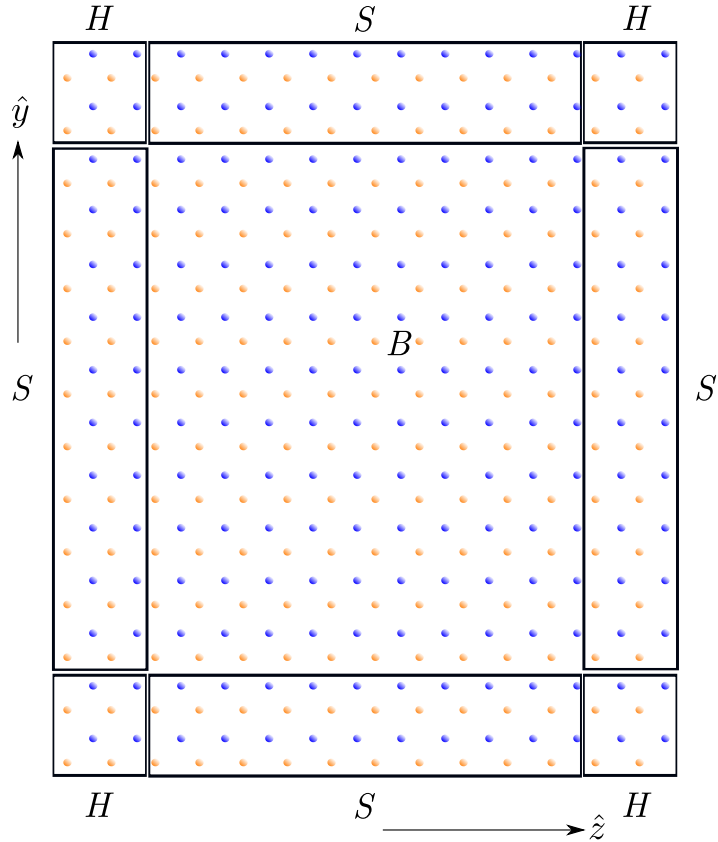


Fig. 4.5 Schematic diagram of the column geometry (top view). Blue circles correspond to Bi (or Sb) and orange circles correspond to Zn. Li is omitted for clarity. Bulk, surface and hinge regions are denoted by the boxes labelled with B, S and H respectively. Notice also that the downfolded Hamiltonian does not contain orbitals at the Li site.

measure in each region the probability amplitude of the Bloch wavefunctions. These are defined as

$$w_R(k_x, n) = \frac{1}{N} \sum_{\mathbf{r} \in R} |\langle \mathbf{r} | \psi_n(k_x, \mathbf{r}) \rangle|^2, \quad (4.2)$$

where R is one the three regions defined above, \mathbf{r} a vector in the yz plane, N is the number of sites in such plane, k_x the crystal momentum along \hat{x} and n a band index.

Figure 4.6(a) and (b) show the hinge band structure in the absence of strain for LiBiZn and LiSbZn, respectively. To highlight the electronic structure near the hinges, the points have larger size the larger $w_H(k_x, n)/w_B(k_x, n)$ is. In

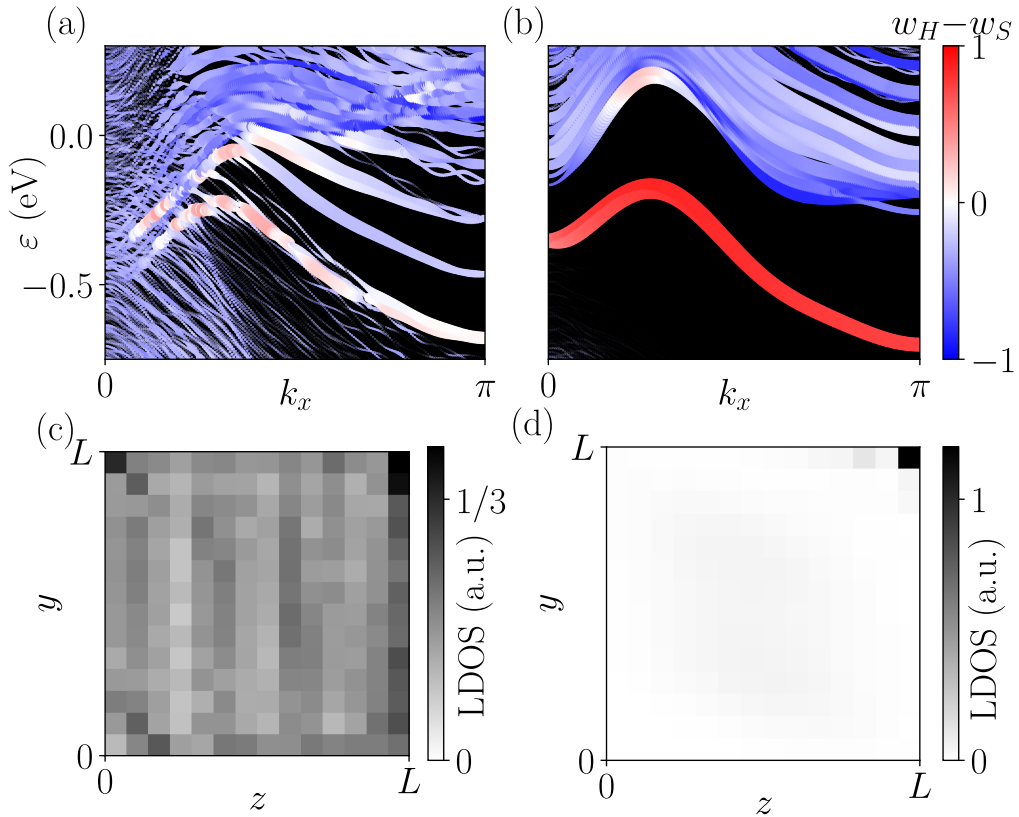


Fig. 4.6 Hinge band structure in the absence of strain for a system having 14×14 unit cells along the \hat{y} and \hat{z} directions and infinite along \hat{x} . (a),(b) Energy dispersion for LiBiZn and LiSbZn, respectively. Larger point sizes indicate larger amplitude of the wavefunction at the hinges. The color code compares the probability amplitude of the wavefunctions at the hinges and surfaces, such that pure red corresponds to a hinge mode, pure blue to a surface state, and white to a state with equal probability per site in both regions. (c),(d) Local density of states for LiBiZn and LiSbZn, respectively, at $\varepsilon = -0.35$ eV.

addition, the color code is taken proportional to $w_H - w_S$, in order to directly compare the probability amplitude of the Bloch wavefunctions at hinges and surfaces. For LiBiZn, the gap is closed near Γ , while states with relatively large amplitude at hinges can be observed near the Brillouin zone border. For these states, however, we obtain $w_H \sim w_S$, indicating a strong hybridization with surface modes. At similar energy and with rather similar k_x -dispersion, LiSbZn also exhibits states with large amplitude at the hinges. Importantly, for these states we find $w_H \gg w_S$.

Figures 4.6(c) and (d) present for both compounds the local density of states (LDOS) which could be measured, e.g., by scanning tunneling spectroscopy.

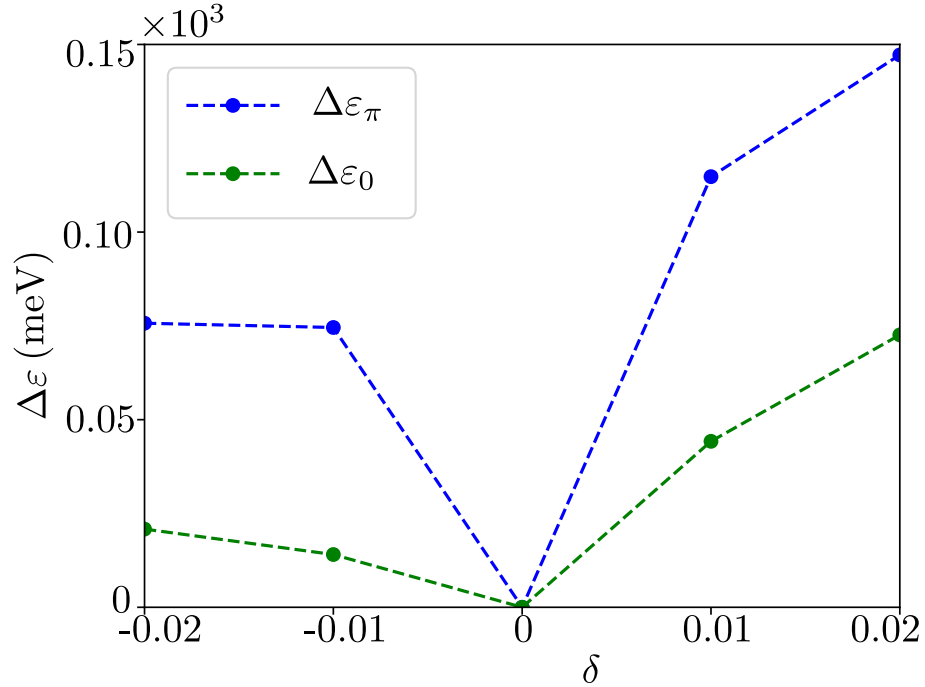


Fig. 4.7 Change in the energy of the hinge modes at $k_x = 0$ ($\Delta\varepsilon_0$) and $k_x = \pi$ ($\Delta\varepsilon_\pi$) as a function of uniaxial strain perpendicular to the hinge.

Fixing the energy at -0.35 eV, a relatively large LDOS at the Zn-Zn hinge can be observed in both compounds. In line with the results above, LiSbZn being both insulating in the bulk and at surface, the found hinge modes are exponentially localized at the hinge for all momenta and the LDOS accordingly decays very fast away from the hinge. On the other hand, a much larger spread of the hinge mode along the surface can be observed in LiBiZn. An analysis of the orbital composition indicates that hinge modes have a weight of 95% on the Zn-4s orbitals. Notice that the hinge do disperse along and have a bandwidth of ~ 0.5 eV.

Noteworthy, the hinge modes in LiSbZn do not close the bulk gap, as expected for a topologically trivial system. We find that uniaxial strain does not change this fact but it can affect the energy position of the hinge modes. Changes in the order of 10 meV are found for a 2% lattice deformation (Fig. 4.7).

4.6 Conclusions

Motivated by recent predictions of hinge modes in models for systems with biquadratic band crossings, we have analyzed based on accurate tight-binding

models the surface and hinge electronic structure of two half-Heusler compounds, LiBiZn and LiSbZn. These compounds should be representative of many others in the space group 216, the former having a band inversion and the latter being topologically trivial. Our calculations indicate the existence of topologically trivial hinge modes in both kinds of systems. In LiBiZn, topological surface states can naturally hybridize with these modes, which obscures their observation. On the contrary, the electronic structure of the topologically trivial LiSbZn is gapped both in the bulk and at the surfaces, and the hinge modes are exponentially localized for all momenta. Thus, our results indicate that topologically trivial members of the half-Heusler material class are prone to exhibit cleaner (free from hybridization with bulk or surface states) hinge modes than topological non-trivial compounds.

In addition, we have found that uniaxial strain reducing the cubic symmetry does not change the topology of the found hinge modes but can affect their energy. This might provide a controllable platform to experimentally study various problems involving electronic matter in one dimension. One relevant open question is the stability of the hinge modes with respect to possible surface reconstructions, known to be relevant for semiconductors within the same space group [202]. Experimental information of the actual hinges that naturally tend to exist in this broad material class would be of interest. Last, in view of their relatively small bandwidth, a second interesting question for future investigation is the fate of the found hinge modes in the presence of Coulomb interactions not considered in our tight-binding Hamiltonian description.

4.7 Appendix: Eight band tight-binding Hamiltonian

In this section, we provide a tight-binding model that describes the low-energy electronic structure of face-centered cubic half-Heuslers in space group 216. While the tight-binding Hamiltonian obtained from the Wannier functions construction naturally involves many long-range hopping parameters, we have found that a truncated Hamiltonian, which keeps only nearest neighbor terms provides an efficient low-energy description.

Notice that the calculations in the main text are based on the tight-binding models involving all of the *ab initio* obtained matrix elements. As explained in the main text, at least six orbitals must be considered to correctly describe the topological properties of the electronic structure of hHs. For simplicity in the DFT downfolding, we keep eight orbitals in the energy windows ($[-6, 2]$ eV). We use the basis $\{|s\uparrow\rangle, |s\downarrow\rangle, |p_y\uparrow\rangle, |p_y\downarrow\rangle, |p_z\uparrow\rangle, |p_z\downarrow\rangle, |p_x\uparrow\rangle, |p_x\downarrow\rangle\}$ where s corresponds to Zn-4s and p to either Bi-6p or Sb-5p. The lattice Bravais vectors $\vec{a}_1, \vec{a}_2, \vec{a}_3$ read

$$\begin{pmatrix} a_1 \\ a_2 \\ a_3 \end{pmatrix} \rightarrow \frac{a}{2} \begin{pmatrix} 0 & 1 & 1 \\ 1 & 0 & 1 \\ 1 & 1 & 0 \end{pmatrix} \begin{pmatrix} \hat{x} \\ \hat{y} \\ \hat{z} \end{pmatrix}, \quad (4.3)$$

where $\hat{x}, \hat{y}, \hat{z}$ are the cartesian vectors and $a = 8.79$ is the magnitude of the lattice Bravais vectors. The reciprocal lattice vectors $\vec{b}_1, \vec{b}_2, \vec{b}_3$ are expressed as $\vec{b}_1 = \frac{2\pi}{a}(\hat{x} - \hat{y} + \hat{z})$, $\vec{b}_2 = \frac{2\pi}{a}(\hat{x} + \hat{y} - \hat{z})$, $\vec{b}_3 = \frac{2\pi}{a}(-\hat{x} + \hat{y} + \hat{z})$.

[eV]	LiBiZn	LiSbZn
ε_s	-1.9	-1.4
ε_p	-2.1	-2.2
ν_{sp}	0.9	-0.9
λ_{soc}	-0.4	-0.1
t_s	0.1	0.2
$t_p^{(d)}$	0.1	0.1
$t_p^{(od)}$	0.1	0.1
t_{sp}	0.9	-0.9

Table 4.1 Tight-binding parameters for LiBiZn and LiSbZn.

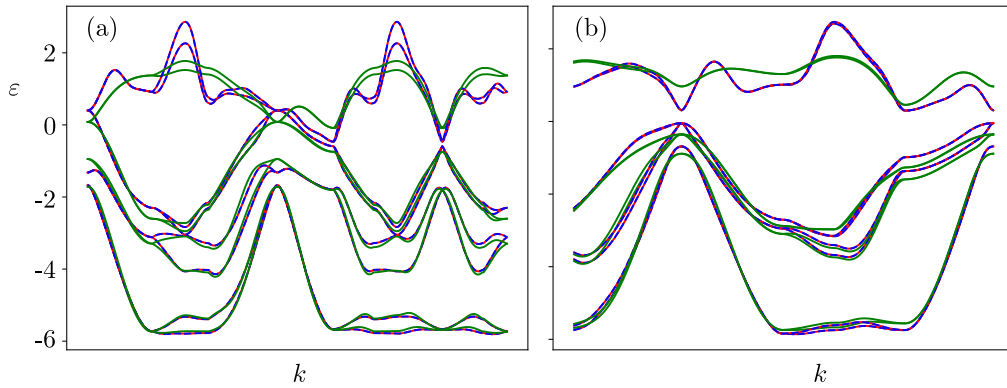


Fig. 4.8 band structure for (a) LiBiZn and (b) LiSbZn is shown. Red, blue and green colors indicate the band structures obtained from DFT, full wannier tight-binding, and truncated wannier tight-binding Hamiltonian respectively. The k -path is chosen as same in 4.1.

The resulting Hamiltonian involves diagonal energies for s (ε_s) and p orbitals (ε_p), a local spin-orbit coupling λ_{soc} in the p shell, hoppings between s orbitals (t_s), between identical ($t_p^{(d)}$) or different ($t_p^{(od)}$) p orbitals, and between s and p orbitals (t_{sp}) as well as a local hybridization between s and p orbitals (ν_{sp}). The values adopted by these parameters in LiBiZn and LiSbZn are presented in Table 4.1. The Hamiltonian in momentum space reads

$$\begin{aligned}
 \mathcal{H}(\mathbf{k}) = & \mathcal{H}_0 + \\
 & \left(t_{sp}h_{sp,001} + t_p^{(od)}h_{p,001}^{(od)} + t_s\mathbf{1}_s + t_p^{(d)}h_{p,001}^{(d)} \right) e^{i\frac{(k_x+k_y)}{2}} + \\
 & \left(t_{sp}h_{sp,010} + t_p^{(od)}h_{p,010}^{(od)} + t_s\mathbf{1}_s + t_p^{(d)}h_{p,010}^{(d)} \right) e^{i\frac{(k_x+k_z)}{2}} + \\
 & \left(t_{sp}h_{sp,100} + t_p^{(od)}h_{p,100}^{(od)} + t_s\mathbf{1}_s + t_p^{(d)}h_{p,100}^{(d)} \right) e^{i\frac{(k_y+k_z)}{2}} + \\
 & \left(t_p^{(od)}h_{p,1-10}^{(od)} + t_s\mathbf{1}_s + t_p^{(d)}h_{p,001}^{(d)} \right) e^{i\frac{(k_y-k_x)}{2}} + \\
 & \left(t_p^{(od)}h_{p,10-1}^{(od)} + t_s\mathbf{1}_s + t_p^{(d)}h_{p,010}^{(d)} \right) e^{i\frac{(k_z-k_x)}{2}} + \\
 & \left(t_p^{(od)}h_{p,01-1}^{(od)} + t_s\mathbf{1}_s + t_p^{(d)}h_{p,100}^{(d)} \right) e^{i\frac{(k_z-k_y)}{2}} + \\
 & + h.c.
 \end{aligned} \tag{4.4}$$

where

$$\mathcal{H}_0 = \varepsilon_s\mathbf{1}_s + \varepsilon_p\mathbf{1}_p + \nu_{sp}V_{sp} + \lambda_{soc}\Gamma \tag{4.5}$$

and matrices introduced are

$$\mathbf{1}_s = \begin{bmatrix} \mathbf{1}_{2 \times 2} & \mathbf{0}_{6 \times 6} \\ \mathbf{0}_{6 \times 6} & \mathbf{0}_{6 \times 6} \end{bmatrix}$$

$$\mathbf{1}_p = \begin{bmatrix} \mathbf{0}_{2 \times 2} & \mathbf{0}_{6 \times 6} \\ \mathbf{0}_{6 \times 6} & \mathbf{1}_{6 \times 6} \end{bmatrix}$$

$$V_{sp} = \begin{pmatrix} 0 & 0 & 1 & 0 & 1 & 0 & 1 & 0 \\ 0 & 0 & 0 & 1 & 0 & 1 & 0 & 1 \\ 1 & 0 & 0 & 0 & 0 & 0 & 0 & 0 \\ 0 & 1 & 0 & 0 & 0 & 0 & 0 & 0 \\ 1 & 0 & 0 & 0 & 0 & 0 & 0 & 0 \\ 0 & 1 & 0 & 0 & 0 & 0 & 0 & 0 \\ 1 & 0 & 0 & 0 & 0 & 0 & 0 & 0 \\ 0 & 1 & 0 & 0 & 0 & 0 & 0 & 0 \end{pmatrix} \quad (4.6)$$

$$\Gamma = \begin{pmatrix} 0 & 0 & 0 & 0 & 0 & 0 & 0 & 0 \\ 0 & 0 & 0 & 0 & 0 & 0 & 0 & 0 \\ 0 & 0 & 0 & 0 & 0 & i & -i & 0 \\ 0 & 0 & 0 & 0 & i & 0 & 0 & i \\ 0 & 0 & 0 & -i & 0 & 0 & 0 & 1 \\ 0 & 0 & -i & 0 & 0 & 0 & -1 & 0 \\ 0 & 0 & i & 0 & 0 & -1 & 0 & 0 \\ 0 & 0 & 0 & -i & 1 & 0 & 0 & 0 \end{pmatrix} \quad (4.7)$$

$$h_{sp,001} = \begin{pmatrix} 0 & 0 & 0 & 0 & 0 & 0 & 0 & 0 \\ 0 & 0 & 0 & 0 & 0 & 0 & 0 & 0 \\ 1 & 0 & 0 & 0 & 0 & 0 & 0 & 0 \\ 0 & 1 & 0 & 0 & 0 & 0 & 0 & 0 \\ -1 & 0 & 0 & 0 & 0 & 0 & 0 & 0 \\ 0 & -1 & 0 & 0 & 0 & 0 & 0 & 0 \\ 1 & 0 & 0 & 0 & 0 & 0 & 0 & 0 \\ 0 & 1 & 0 & 0 & 0 & 0 & 0 & 0 \end{pmatrix} \quad (4.8)$$

$$h_{p,001}^{(od)} = \begin{pmatrix} 0 & 0 & 0 & 0 & 0 & 0 & 0 & 0 \\ 0 & 0 & 0 & 0 & 0 & 0 & 0 & 0 \\ 0 & 0 & 0 & 0 & -1 & 0 & 2 & 0 \\ 0 & 0 & 0 & 0 & 0 & -1 & 0 & 2 \\ 0 & 0 & 1 & 0 & 0 & 0 & 1 & 0 \\ 0 & 0 & 0 & 1 & 0 & 0 & 0 & 1 \\ 0 & 0 & 2 & 0 & -1 & 0 & 0 & 0 \\ 0 & 0 & 0 & 2 & 0 & -1 & 0 & 0 \end{pmatrix} \quad (4.9)$$

$$h_{p,001}^{(d)} = \begin{pmatrix} 0 & 0 & 0 & 0 & 0 & 0 & 0 & 0 \\ 0 & 0 & 0 & 0 & 0 & 0 & 0 & 0 \\ 0 & 0 & 1 & 0 & 0 & 0 & 0 & 0 \\ 0 & 0 & 0 & 1 & 0 & 0 & 0 & 0 \\ 0 & 0 & 0 & 0 & 2 & 0 & 0 & 0 \\ 0 & 0 & 0 & 0 & 0 & 2 & 0 & 0 \\ 0 & 0 & 0 & 0 & 0 & 0 & 1 & 0 \\ 0 & 0 & 0 & 0 & 0 & 0 & 0 & 1 \end{pmatrix} \quad (4.10)$$

$$h_{p,1-10}^{(od)} = \begin{pmatrix} 0 & 0 & 0 & 0 & 0 & 0 & 0 & 0 \\ 0 & 0 & 0 & 0 & 0 & 0 & 0 & 0 \\ 0 & 0 & 0 & 0 & 1 & 0 & -2 & 0 \\ 0 & 0 & 0 & 0 & 0 & 1 & 0 & -2 \\ 0 & 0 & -1 & 0 & 0 & 0 & 1 & 0 \\ 0 & 0 & 0 & -1 & 0 & 0 & 0 & 1 \\ 0 & 0 & -2 & 0 & -1 & 0 & 0 & 0 \\ 0 & 0 & 0 & -2 & 0 & -1 & 0 & 0 \end{pmatrix} \quad (4.11)$$

Above, we have only shown the terms which arise from independent tight-binding parameters. The other hopping matrices can be connected by the symmetries of the Hamiltonian. For instance, $C_{3,111}h_{sp,001}C_{3,111}^{-1} = h_{sp,100}$, $C_{3,111}h_{p,001}^{(od)}C_{3,111}^{-1} = h_{p,100}^{(od)}$, $C_{3,111}h_{p,1-10}^{(od)}C_{3,111}^{-1} = h_{p,01-1}^{(od)}$, and so on.

We now explain the symmetries of this Hamiltonian. In the cubic phase, the system has two-fold rotational symmetries with respect to the cubic edges (e.g., C_{2z}), three-fold rotational symmetries with respect to the cubic diagonals ($C_{3,111}$), reflection symmetries (M_{xy}), fourfold rotoinversion symmetries ($C_{4z}I$), and time-reversal symmetry (\mathcal{T}). In cartesian form, the Hamiltonian

$\mathcal{H}(k_x, k_y, k_z)$ satisfies:

$$C_{2z}\mathcal{H}(k_x, k_y, k_z)C_{2z}^{-1} = \mathcal{H}(-k_x, -k_y, k_z) \quad (4.12)$$

$$C_{3,111}\mathcal{H}(k_x, k_y, k_z)C_{3,111}^{-1} = \mathcal{H}(k_z, k_x, k_y) \quad (4.13)$$

$$M_{xy}\mathcal{H}(k_x, k_y, k_z)M_{xy}^{-1} = \mathcal{H}(-k_y, -k_x, k_z) \quad (4.14)$$

$$(C_{4z}I)\mathcal{H}(k_x, k_y, k_z)(C_{4z}I)^{-1} = \mathcal{H}(k_y, -k_x, -k_z) \quad (4.15)$$

$$\mathcal{T}\mathcal{H}(k_x, k_y, k_z)\mathcal{T}^{-1} = \mathcal{H}(-k_x, -k_y, -k_z) \quad (4.16)$$

The above symmetry constraints translate to the following set of equations, if the momenta are written in the basis of the reciprocal lattice vectors, coordinates which we name (k_1, k_2, k_3) .

$$C_{2z}\mathcal{H}(k_1, k_2, k_3)C_{2z}^{-1} = \mathcal{H}(k_3, -k_1 - k_2 - k_3, k_1) \quad (4.17)$$

$$C_{3,111}\mathcal{H}(k_1, k_2, k_3)C_{3,111}^{-1} = \mathcal{H}(k_3, k_1, k_2) \quad (4.18)$$

$$M_{xy}\mathcal{H}(k_1, k_2, k_3)M_{xy}^{-1} = \mathcal{H}(k_1, -k_1 - k_2 - k_3, k_3) \quad (4.19)$$

$$(C_{4z}I)\mathcal{H}(k_1, k_2, k_3)(C_{4z}I)^{-1} = \mathcal{H}(-k_1 - k_2 - k_3, k_1, k_2) \quad (4.20)$$

$$\mathcal{T}\mathcal{H}(k_1, k_2, k_3)\mathcal{T}^{-1} = \mathcal{H}(-k_1, -k_2, -k_3), \quad (4.21)$$

where we have used the relations; $\hat{k}_x = \frac{a}{2\pi}(\frac{\vec{k}_1 + \vec{k}_2}{2})$, $\hat{k}_y = \frac{a}{2\pi}(\frac{\vec{k}_2 + \vec{k}_3}{2})$, $\hat{k}_z = \frac{a}{2\pi}(\frac{\vec{k}_3 + \vec{k}_1}{2})$.

Finally, the representation used for the time-reversal operator in the 8-dimensional Hilbert space is

$$\mathcal{T} = \begin{pmatrix} 0 & -1 & 0 & 0 & 0 & 0 & 0 & 0 \\ 1 & 0 & 0 & 0 & 0 & 0 & 0 & 0 \\ 0 & 0 & 0 & -1 & 0 & 0 & 0 & 0 \\ 0 & 0 & 1 & 0 & 0 & 0 & 0 & 0 \\ 0 & 0 & 0 & 0 & 0 & -1 & 0 & 0 \\ 0 & 0 & 0 & 0 & 1 & 0 & 0 & 0 \\ 0 & 0 & 0 & 0 & 0 & 0 & 0 & -1 \\ 0 & 0 & 0 & 0 & 0 & 0 & 1 & 0 \end{pmatrix} \mathcal{K} \quad (4.22)$$

where \mathcal{K} is the complex conjugation operator, while the representation of the unitary symmetries are

$$C_{3,111} = \frac{1}{2} \begin{pmatrix} \alpha & -\alpha^* & 0 & 0 & 0 & 0 & 0 & 0 \\ \alpha & \alpha^* & 0 & 0 & 0 & 0 & 0 & 0 \\ 0 & 0 & 0 & 0 & 0 & 0 & \alpha & -\alpha^* \\ 0 & 0 & 0 & 0 & 0 & 0 & \alpha & \alpha^* \\ 0 & 0 & \alpha & -\alpha^* & 0 & 0 & 0 & 0 \\ 0 & 0 & \alpha & \alpha^* & 0 & 0 & 0 & 0 \\ 0 & 0 & 0 & 0 & \alpha & -\alpha^* & 0 & 0 \\ 0 & 0 & 0 & 0 & \alpha & \alpha^* & 0 & 0 \end{pmatrix} \quad (4.23)$$

with $\alpha = 1 - i$,

$$C_{4z}I = \frac{1}{\sqrt{2}} \times \begin{pmatrix} \alpha^* & 0 & 0 & 0 & 0 & 0 & 0 & 0 \\ 0 & \alpha & 0 & 0 & 0 & 0 & 0 & 0 \\ 0 & 0 & 0 & 0 & 0 & 0 & \alpha^* \beta_{yz} & 0 \\ 0 & 0 & 0 & 0 & 0 & 0 & 0 & \alpha \beta_{yz} \\ 0 & 0 & 0 & 0 & -\alpha^* \beta_{yz} & 0 & 0 & 0 \\ 0 & 0 & 0 & 0 & 0 & -\alpha \beta_{yz} & 0 & 0 \\ 0 & 0 & -\alpha^* \beta_{yz} & 0 & 0 & 0 & 0 & 0 \\ 0 & 0 & 0 & -\alpha \beta_{yz} & 0 & 0 & 0 & 0 \end{pmatrix} \quad (4.24)$$

where $\beta_{yz} = e^{-i(ky+kz)}$,

$$C_{2z} = \begin{pmatrix} i & 0 & 0 & 0 & 0 & 0 & 0 & 0 \\ 0 & -i & 0 & 0 & 0 & 0 & 0 & 0 \\ 0 & 0 & -i \beta_{xy} & 0 & 0 & 0 & 0 & 0 \\ 0 & 0 & 0 & i \beta_{xy} & 0 & 0 & 0 & 0 \\ 0 & 0 & 0 & 0 & i \beta_{xy} & 0 & 0 & 0 \\ 0 & 0 & 0 & 0 & 0 & -i \beta_{xy} & 0 & 0 \\ 0 & 0 & 0 & 0 & 0 & 0 & -i \beta_{xy} & 0 \\ 0 & 0 & 0 & 0 & 0 & 0 & 0 & i \beta_{xy} \end{pmatrix} \quad (4.25)$$

where $\beta_{xy} = e^{-i(kx+ky)}$, and

$$M_{xy} = \frac{1}{\sqrt{2}} \times$$

$$\begin{pmatrix} 0 & -\alpha^* & 0 & 0 & 0 & 0 & 0 & 0 \\ \alpha & 0 & 0 & 0 & 0 & 0 & 0 & 0 \\ 0 & 0 & 0 & 0 & 0 & 0 & 0 & \alpha^* \beta_{xy} \\ 0 & 0 & 0 & 0 & 0 & 0 & -\alpha \beta_{xy} & 0 \\ 0 & 0 & 0 & 0 & 0 & -\alpha^* \beta_{xy} & 0 & 0 \\ 0 & 0 & 0 & 0 & \alpha \beta_{xy} & 0 & 0 & 0 \\ 0 & 0 & 0 & \alpha^* \beta_{xy} & 0 & 0 & 0 & 0 \\ 0 & 0 & -\alpha \beta_{xy} & 0 & 0 & 0 & 0 & 0 \end{pmatrix} \quad (4.26)$$

Chapter 5

Topological Magnus responses in two and three dimensional systems

5.1 Introduction

The family of Hall effects have revolutionized the solid state physics in the context of novel electronic states and electron dynamics [203, 204, 1]. Starting from the Lorentz force mediated classical Hall effect and quantum Hall effect, various new types of Hall effect such as anomalous Hall effect, spin Hall effect, thermal Hall effect etc. have been discovered over the years [203, 204, 1, 4, 205–211]. Among them, the Berry curvature (BC) induced Hall effects, taking place without external magnetic field, have drawn tremendous attention to both the theorists and experimentalists [4, 205–210, 20]. For time reversal symmetry (TRS) broken systems, the BC takes the form $\Omega(\mathbf{k}) \neq -\Omega(-\mathbf{k})$ leading to a finite total BC for the occupied states. By contrast, in TRS invariant systems, BC follows $\Omega(\mathbf{k}) = -\Omega(-\mathbf{k})$ giving rise to zero total BC [20], that further causes the intrinsic anomalous Hall effect to vanish. Interestingly, it has been theoretically proposed and experimentally verified that unlike the linear anomalous Hall effect, the nonlinear anomalous Hall effect can survive in TRS invariant systems with broken inversion symmetry [212–220]. Very recently, the same systems (TRS invariant but inversion broken) with a built-in electric field at zero magnetic field is found to exhibit a new type of a linear response namely, Magnus Hall effect (MHE) [221]. The MHE is originated from the Magnus velocity of electron that is perpendicular to the BC and the built-in electric field. Along with the prediction of MHE, it has also been proposed that the Magnus Nernst effect

(MNE) and Magnus thermal Hall effect can also appear in these systems in the presence of applied thermal gradiant [222].

It has been proposed that the two-dimensional (2D) transition metal dichalcogenides MX_2 ($\text{M}=\text{Mo, W}$ and $\text{X}=\text{S, Se, Te}$) [223–225, 213], monolayer (ML) graphene on hBN, bilayer (BL) graphene with applied perpendicular electric field [226–228], heterostructures [229] and surfaces of topological insulator (TI) [230] are the possible candidates to investigate the MHE and MNE for their TRS invariant and inversion broken nature. The MHE has been theoretically studied recently in graphene and transition metal dichalcogenides using the low-energy model without warping (except bilayer graphene where trigonal warping is considered) and strain [221, 222]. On the other hand, it has been shown that without spin-orbit coupling and tilting of Dirac cone, the BC dipole becomes substantially large in presence of strain and warping for graphene [228]. Motivated by the BC dipole induced nonlinear anomalous Hall effect in TRS invariant systems, our interest here is to investigate Magnus transport in the presence of strain and warping for the above proposed suitable candidates.

Turning to the field of three-dimensional (3D) topological systems such as, Weyl semimetals (WSMs), considered to be a 3D analogue of graphene, have been studied extensively for their intriguing properties and anomalous response functions. The gap closing points, guaranteed by some crystalline symmetries, in WSMs are referred to as Weyl nodes with topological charge $n = 1$ [231–237]. There exists two Weyl nodes of opposite chiralities for the TRS broken WSM, while inversion broken WSM exhibits at least four Weyl nodes [238, 239]. The WSMs can also be classified as type-I and type-II. In the case of type-I WSM, Fermi surface is always point like irrespective of the tilting of the node. On the other hand, in type-II WSM finite electron and hole pockets appear at the Fermi level as a result of finite tilting of the energy spectra[240–242]. Moreover, it has been recently found that $n > 1$ multi-WSM (mWSM) shows non-linear band touching [243, 244]. The WSMs are shown to exhibit many intriguing transport properties, originated by chiral anomaly, such as negative longitudinal magnetoresistance and planar Hall effect [245–258]. Tilting of energy dispersion and non-linearity of band touching further decorate the transport signatures [259–263]. This motivates us to extend our investigation of MHE to 3D topological systems considering a generic mWSM Hamiltonian.

In this work, we first capture intriguing Fermi surface phenomena in presence of strain and warping by examining MHE and MNE in ballistic regime for 2D

topological systems such as, ML, BL graphene and surface states of TIs. We find that in strained ML graphene without warping, the total valley integrated Magnus responses are zero as the contribution coming from individual valley exactly cancels each other. The valley polarized contribution thus leads to the Magnus valley Hall, Magnus valley Nernst effects. Interestingly, warping induces valley integrated finite Magnus responses as the asymmetries in Fermi surface and BC result in unequal valley polarized contributions. The magnitude of the Magnus responses enhance with increasing the warping parameter. The same is observed for the surface states of TI in presence of hexagonal warping. On the other hand, for BL graphene, the Magnus transport coefficients are substantially modified depending on the positive and negative values of strain while warping do not affect the Magnus transport. Finally, going beyond 2D systems, we study Magnus responses in 3D WSMs to examine the effect of tilt and anisotropic nonlinear dispersion. We find that the MHE is identically zero for each Weyl node without tilt. Remarkably, chiral (achiral) tilt causes finite MH and MN conductivities to generate from individual Weyl nodes resulting in Magnus (Magnus Valley) responses. Moreover, our study indicates that the topological charge associated with Weyl node imprints its effect on the Magnus transport properties.

The rest of the paper is organized as follows. In Sec. 5.2, we derive the general expressions of MH and MN conductivities in both ballistic and diffusive regimes. Following which, in sec. 5.3 we have calculated the Magnus transport responses in the presence of strain and warping (tilt and non-linearity) for different 2D (3D) topological systems, respectively. Finally, we summarize our results and discuss possible future directions in Sec. 5.4.

5.2 Formalism of Magnus transport

In this section, we derive the general expression for MH, MN conductivities in both diffusive and ballistic regimes using Boltzmann transport equation. To begin with, we consider mesoscopic systems of electronic transport in a Hall bar device without applying any external magnetic field. In this setup, the source and the drain are kept at different electrostatic potential energy with the gate voltages given by U_s and U_d , respectively. Their difference $\Delta U = U_s - U_d$ introduces a built-in electric field $\mathbf{E}_{\text{in}} = \nabla_{\mathbf{r}} U/e$ ($-e$ is the electronic charge) in the device

with a slowly varying electric potential energy $U(r)$ along the length of the sample.

Now in the presence of external electric field \mathbf{E} and temperature gradient ∇T applied between the source and drain, the charge current \mathbf{J} and thermal current \mathbf{Q} from linear response theory, can be written as

$$\begin{aligned} J_a &= \sigma_{ab}E_b + \alpha_{ab}(-\nabla_b T) \\ Q_a &= \bar{\alpha}_{ab}E_b + \kappa_{ab}(-\nabla_b T), \end{aligned} \quad (5.1)$$

where a and b are spatial indices running over x, y, z . Here σ , α and κ different conductivity tensors.

The phenomenological Boltzmann transport equation can be written as [264, 265]

$$\left(\frac{\partial}{\partial t} + \dot{\mathbf{r}} \cdot \nabla_{\mathbf{r}} + \dot{\mathbf{k}} \cdot \nabla_{\mathbf{k}} \right) f_{\mathbf{k}, \mathbf{r}, t} = I_{coll}\{f_{\mathbf{k}, \mathbf{r}, t}\}, \quad (5.2)$$

where the right side $I_{coll}\{f_{\mathbf{k}, \mathbf{r}, t}\}$ is the collision integral which incorporates the effects of electron correlations and impurity scattering. The electron distribution function is denoted by $f_{\mathbf{k}, \mathbf{r}, t}$. Now under the relaxation time approximation the steady-state Boltzmann equation can be written as

$$(\dot{\mathbf{r}} \cdot \nabla_{\mathbf{r}} + \dot{\mathbf{k}} \cdot \nabla_{\mathbf{k}}) f_{\mathbf{k}} = \frac{f_0 - f_{\mathbf{k}}}{\tau(\mathbf{k})}, \quad (5.3)$$

where $\tau(\mathbf{k})$ is the scattering time. Note that in this work, we ignore the momentum dependence of $\tau(\mathbf{k})$ for simplifying the calculations and assume it to be a constant. The equilibrium distribution function f_0 in absence of applied electric field \mathbf{E} and temperature gradient $\nabla_r T$ is given by the Fermi function,

$$f_0(\mathbf{k}, \mathbf{r}) = \frac{1}{1 + e^{\beta[\epsilon(\mathbf{k}, \mathbf{r}) - \mu]}}, \quad (5.4)$$

where $\beta = 1/(k_B T)$, $\epsilon(\mathbf{k}, \mathbf{r}) = \epsilon_{\mathbf{k}} + U(\mathbf{r})$, with $\epsilon_{\mathbf{k}}$ and μ are the energy dispersion and chemical potential, respectively. The motion of the wave packet inside the Hall bar is described by the semiclassical equations of motion [20, 266]

$$\dot{\mathbf{r}} = \nabla_{\mathbf{k}}\epsilon_{\mathbf{k}} + [\nabla_{\mathbf{r}}U + e\mathbf{E}] \times \boldsymbol{\Omega}, \quad (5.5)$$

$$\dot{\mathbf{k}} = -\nabla_{\mathbf{r}}U - e\mathbf{E}. \quad (5.6)$$

The first, second and third term in the right hand side of Eq. (5.5) respectively represent the band velocity, Magnus velocity $V_{\text{magnus}} = \nabla_{\mathbf{r}} U \times \boldsymbol{\Omega}$ and anomalous velocity $V_{\text{ano}} = \mathbf{E} \times \boldsymbol{\Omega}$. The Magnus velocity V_{magnus} can be thought of a quantum analog of the classical Magnus effect.

Now to calculate MH and MN conductivities, we apply the electric field and temperature gradient along x direction. Assuming the length of the sample is along x axis, we have $U(\mathbf{r}) = U(x)$, $\epsilon(\mathbf{k}, \mathbf{r}) = \epsilon_{\mathbf{k}} + U(x)$ and $\mathbf{E}_{\text{in}} = \frac{1}{e} \frac{\partial U(x)}{\partial x} \hat{x}$. Since we consider $U(x)$ is slowly varying, the electron wave packets traveling inside the sample still have well-defined momentum \mathbf{k} . Considering the velocity of an incident electron (v_x, v_y) , transit time through the electric field region becomes $t = L/v_x$ where L is device length along x -direction. For $v_y \neq 0$, the center of the wave packet receives a transverse shift (in y -direction), followed by Magnus velocity proportional to $\nabla_x U \Omega_z$, while traversing the junction due to the built-in electric field \mathbf{E}_{in} . Now the charge and thermal currents can be written as

$$\{\mathbf{J}(x), \mathbf{Q}(x)\} = \int d\mathbf{k} \dot{\mathbf{r}} \{-e, [\epsilon(\mathbf{k}, x) - \mu]\} f(\mathbf{k}, x) . \quad (5.7)$$

Combining Eqs. (5.3), (5.5), and (5.6) the non-equilibrium distribution function f up to linear order in the bias fields can be written as

$$f = f_0 + v_x \tau \left(e E_x + \frac{[\epsilon(\mathbf{k}, \mathbf{r}) - \mu]}{T} \nabla_x T \right) \partial_{\epsilon} f_0 . \quad (5.8)$$

Considering U as a slowly varying function of x , $\partial U / \partial x = \Delta U / L$, one can obtain f to be spatially independent. To be precise, using Eq. (5.8) into the Eq. (5.7) and comparing with Eq. (5.1), the MH conductivity σ is found to be [222]

$$\sigma = -\frac{e^2 \tau \Delta U}{L} \int d\mathbf{k} \Omega_z v_x \partial_{\epsilon} f_0 , \quad (5.9)$$

Similarly, the MN conductivity α is given by [222]

$$\alpha = \frac{e k_B \tau \Delta U}{L} \int d\mathbf{k} \Omega_z v_x \beta(\epsilon_k - \mu) \partial_{\epsilon} f_0 \quad (5.10)$$

where we have neglected the contributions coming from the band velocity. Interestingly, as discussed above these Magnus responses are dependent on the built-in electric field.

Considering the limit $\mu \gg \frac{1}{\beta}$ in Eq. (5.9)-(5.10), the Wiedemann-Franz law and Mott relation allow us to compute MN conductivity α and Magnus thermal Hall (MTH) conductivity κ alternatively [18, 267, 268]

$$\alpha = -\frac{\pi^2 k_B^2 T}{3e} \frac{\partial \sigma}{\partial \mu}, \quad \text{and} \quad \kappa = \frac{\pi^2 k_B^2 T}{3e^2} \sigma. \quad (5.11)$$

Having discussed above the diffusive limit, we shall now illustrate the Magnus responses in the ballistic regime. Since in this regime, the mean free time between two collisions is infinite $\tau \rightarrow \infty$ i.e., essentially no collision occur in the transport direction inside the length L along the x -direction of the Hall bar. Therefore, the right hand side of the Boltzmann transport equation given in Eq. (5.2) vanishes in the ballistic regime. In this setup, the carriers from the source with only positive velocity $v_x > 0$ are allowed in region $0 < x < L$. Now the ansatz for the non-equilibrium distribution function is the following

$$f(\mathbf{k}, \mathbf{r}) = \begin{cases} -\Delta \mu \partial_\epsilon f_0 - \frac{\epsilon(\mathbf{k}, \mathbf{r}) - \mu}{T} \Delta T \partial_\epsilon f_0 & \text{for } v_x > 0, \\ 0 & \text{for } v_x < 0. \end{cases} \quad (5.12)$$

Comparing the Eq. (5.8) and Eq. (5.12), one can identify the scattering length $v_x \tau$ with the device length L so that $-eLE_x = \Delta \mu$ and $\Delta T/L = -\nabla_x T$. The MH and MN coefficients in ballistic regime can be obtained as [221, 222]

$$\sigma = -\frac{e^2}{T} \Delta U \int_{v_x > 0} d\mathbf{k} \Omega_z \partial_\epsilon f_0, \quad (5.13)$$

$$\alpha = \frac{e}{T} \Delta U \int_{v_x > 0} d\mathbf{k} \Omega_z (\epsilon_k - \mu) \partial_\epsilon f_0. \quad (5.14)$$

Similar to the diffusive regime, the Magnus transport coefficients in the ballistic regime also obey the Mott relation and the Wiedemann-Franz law.

We would now like to add a few comments on Magnus responses. It is clear from the Eqs. (5.9)-(5.10) as well as Eqs. (5.13)-(5.14) that the MHE and MNE are purely determined by Fermi surface properties as they incorporate $\partial_\epsilon f_0$ factor. In order to obtain finite Magnus responses, the systems should have asymmetric Fermi surface. In addition, the system must possess finite BC. Moreover, the condition $v_x > 0$ happens to be very important while summing the BC over the Brillouin zone. Combining all these, the active momentum modes \mathbf{k}_v , over the Fermi surface $\epsilon_k = \mu$, for which $v_x > 0$ would contribute to Magnus

transport. The remaining momentum modes $\mathbf{k} - \mathbf{k}_v$ become inert in this ballistic transport and BC for these momentum modes do not determine the transport. These transports thus allow us to scan different Fermi surfaces by tuning μ and get the idea about angular distribution of BC within a given Fermi surface.

The Magnus responses can be regarded as an effective second order transport as the built-in electric field ΔU and external bias both come into calculation of currents. However, in terms of the external bias field, it is still a linear response phenomena. The BC dipole induced second order transport [212], given by $D_{ij} = \int d\mathbf{k} d_{ij} \delta(\epsilon_{\mathbf{k}} - \mu)$ with $d_{ij} = v_i(\mathbf{k}) \Omega_j(\mathbf{k})$, is primarily different from Magnus transport for which the tilting of Dirac cone is no longer important to obtain a finite response. Depending upon the mirror symmetries present in the systems, one can find symmetry permitted components of non-linear transport coefficients where d_{ij} becomes an even function of \mathbf{k} [269, 216, 270]. By contrast, quantized non-linear response namely, circular photo-galvanic effect can be observed for mirror symmetry broken non-centrosymmetric systems [271, 272].

Regarding the symmetry requirements to observe Magnus ballistic transport, we note that the presence of crystalline symmetries such as in-plane C_2 and out-of-plane mirror can generate clean MH responses, nullifying other trivial linear transverse signals [273]. Using these crystalline symmetries, it is also possible to categorize non-linear anomalous Hall and Magnus Hall effects in different classes of material, in which time-reversal symmetry is preserved but inversion is broken. To be more precise, the noncentrosymmetric point groups containing $\{C_{2z}, C_{4z}, C_{6z}, S_{4z}\}$ symmetry operations force the BC to become zero, and as a consequence both MH conductivity and non-linear Hall conductivity both vanish in these systems. Following the above analysis, crystallographic point groups $\{C_1, C_{1h}, C_{1v}, C_2, C_{2v}, C_3, C_{3h}, C_{3v}, D_{3h}, D_3\}$ (2D transition metal dichalcogenides such as, WTe₂, MoS₂) and $\{O, T, T_h\}$ (particularly for 3D) allowing non-zero local BC can lead to both MHE and non-linear Hall effect in general [212, 273].

We would also like to point out that at least one symmetry between TRS and inversion symmetry has to be broken in the system. Although the previous studies only concentrate on TR invariant and inversion symmetry broken systems, one can in principle get Magnus responses even in the absence of TRS as long as the active momentum modes over the Fermi surface have finite BC. This further motivates us to study TRS broken topological systems in addition to

the TRS invariant topological systems. Since the strain, warping, and tilt can modify the Fermi surface significantly as well as the BC distribution accordingly, the Magnus responses can show interesting behavior which we discuss in next section.

It is important to note that along with Magnus Hall current, there exists a trivial transverse current (regular Hall current) that arises from the transverse velocity anisotropy of the Fermi surface: $\int_{v_x > 0} d\mathbf{k} v_y(\mathbf{k}) \delta(\epsilon_{\mathbf{k}} - \mu)$. However, according to the symmetry analysis given above, in presence of certain mirror symmetry (specifically, mirror plane perpendicular to the current direction) combined with time reversal symmetry, the trivial transverse current can be shown to vanish leaving a finite MH current[221, 273]. In addition to the trivial Hall current, linear anomalous Hall current induced by the non-trivial BC can appear simultaneously with MHE in time-reversal broken systems. However, in contrast to MHE, linear anomalous Hall response is not a Fermi surface phenomenon and therefore, does not depend on the derivative of the Fermi function. These two effects can be distinguished by looking at their chemical potential dependencies in experiments. We will discuss these issues elaborately in Sec. 5.3.4.

5.3 Results

In this section, we discuss the effect of strain and warping on MH and MN conductivities in inversion symmetry broken but TRS invariant 2D topological systems, namely for ML, BL graphene and surface states of TI. We extend our analysis in 3D topological systems WSMs, breaking either TRS or inversion symmetry, to investigate the effect of tilt and non-linearity on MHE and MNE. At the outset, we note that we will often refer MH and MN conductivities together as MH responses.

5.3.1 Strained monolayer graphene

The graphene hosts gapless Dirac cones, located at the high symmetry points \mathbf{K} and \mathbf{K}' in the Brillouin zone, with vanishing BC. A finite BC is generated by breaking the inversion symmetry that can be engineered by placing the graphene sheet on hBN substrate[274, 275]. This actually reduces the point group of the system from C_{6v} to C_{3v} , and opens up a gap at the Dirac nodes. Upon

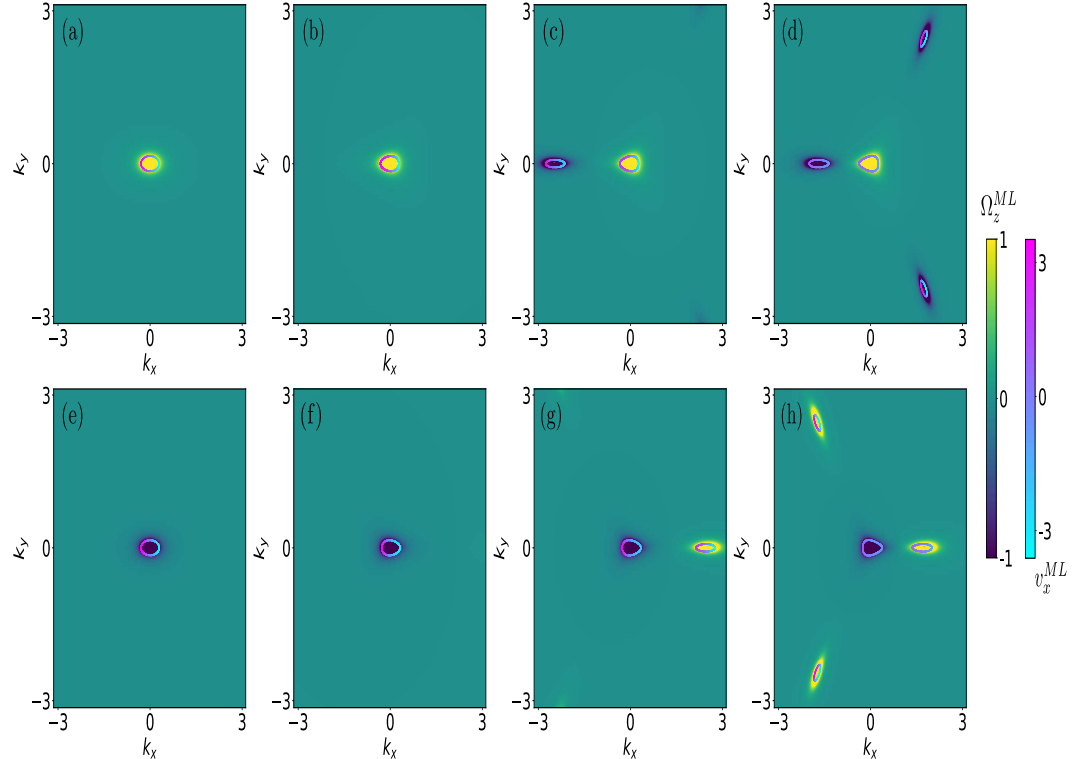


Fig. 5.1 The evolution of BC and Fermi surface in ML graphene (5.16) with warping $\lambda_1 = \lambda_2 = \lambda_3 = \lambda$ and strain $v_2 \neq v_1$. Top panel: The BC ($\Omega_z^{ML}(\mathbf{k}, \zeta = +1)$) and x component of the velocity ($v_x^{ML}(\mathbf{k}, \zeta = +1)$) over the Fermi surface are shown for (a) unstrained ML graphene without warping ($v_2 = v_1, \lambda = 0$), and strained ML graphene ($v_2 = 2v_1$) with C_3 symmetric warping of different strengths (b) $\lambda = 0.2$, (c) $\lambda = 0.35$, (d) $\lambda = 0.5 \text{ eV}\cdot\text{\AA}^2$. Bottom panel: (e)-(h) depict $\Omega_z^{ML}(\mathbf{k}, \zeta = -1)$ and $v_x^{ML}(\mathbf{k}, \zeta = -1)$. The strength of $\Omega_z^{ML}(\mathbf{k}, \zeta)$ and $v_x^{ML}(\mathbf{k}, \zeta)$ are represented in the color codes side by side. The parameters (in the units of energy eV) used in the calculations are $\Delta_g = 0.06 \text{ eV}$, $v_1 = 0.87 \text{ eV}\cdot\text{\AA}$. The Fermi surface is plotted for the constant energy $E = -0.28 \text{ eV}$.

applying a uniform uniaxial strain along one of the two main crystallographic directions in graphene, the massive Dirac nodes become shifted from the high symmetry points along the $k_y = 0$ line due to the combination of TRS and mirror symmetry. The application of the strain creates a difference between hopping amplitudes along the two main crystallographic directions and therefore, changes the corresponding Fermi velocities[276, 228].

Considering only first-order momentum-strain coupling, the low-energy Hamiltonian of the ML strained graphene can be written as [228]

$$\mathcal{H}_0^{ML}(\mathbf{k}) = \frac{\Delta_g}{2}\sigma_z + \zeta v_1 k_x \sigma_x + v_2 k_y \sigma_y, \quad (5.15)$$

where v_1 and $v_2 \neq v_1$ are two strain-dependent Fermi velocities along x and y directions respectively, Δ_g is the gap (also called Semenoff mass), ζ is the valley index and σ 's represent Pauli matrices incorporating sublattice degrees of freedom. To introduce the warping effect in the system, we add a trigonal warping terms, proportional to k^2 , in the Hamiltonian (5.15). Even though the magnitude of the warping term is smaller compared to the leading order term in k , it plays a crucial role in MH responses. Now the complete Hamiltonian for the ML graphene in the presence of both uniaxial strain and trigonal warping reads as [228];

$$\begin{aligned} \mathcal{H}^{ML}(\mathbf{k}) = & \frac{\Delta_g}{2}\sigma_z + \zeta v_1 k_x \sigma_x + v_2 k_y \sigma_y + 2\zeta \lambda_3 k_x k_y \sigma_y \\ & + (\lambda_1 k_y^2 - \lambda_2 k_x^2) \sigma_x = \mathbf{N}_k \cdot \boldsymbol{\sigma} \end{aligned} \quad (5.16)$$

with $\mathbf{N}_k = \{\mathbf{N}_{1k}, \mathbf{N}_{2k}, \mathbf{N}_{3k}\} = \{\zeta v_1 k_x + (\lambda_1 k_y^2 - \lambda_2 k_x^2), v_2 k_y + 2\zeta \lambda_3 k_x k_y, \frac{\Delta_g}{2}\}$ and $\boldsymbol{\sigma} = \{\sigma_1, \sigma_2, \sigma_3\}$. Here, λ_1 , λ_2 and λ_3 are the warping terms. The energy dispersion of the Hamiltonian for $\zeta = \pm 1$ valley is given by

$$E^{ML}(\mathbf{k}) = |\mathbf{N}_k| = \pm \sqrt{\mathbf{N}_{1k}^2 + \mathbf{N}_{2k}^2 + \mathbf{N}_{3k}^2} \quad (5.17)$$

where $+(-)$ represents conduction (valence) band. The warping results in non-linearity and strain causes anisotropy in the dispersion. The BC reads as

$$\Omega_a(\mathbf{k}) = \epsilon_{abc} \frac{\mathbf{N}_k \cdot (\frac{\partial \mathbf{N}_k}{\partial k_b} \times \frac{\partial \mathbf{N}_k}{\partial k_c})}{4|\mathbf{N}_k|^3} \quad (5.18)$$

where ϵ_{abc} is the usual Levi-Civita symbol.

Since ML graphene is a two-dimensional system, only z component of the BC is nonzero. Using Eq. (5.18), the BC for strained ML graphene ($\zeta = \pm 1$) given in Eq. (5.16) can be calculated as

$$\Omega_z^{ML}(\mathbf{k}, \zeta) = \pm \frac{\Delta_g [\zeta v_1 v_2 + 2k_x(\lambda_3 v_1 - \lambda_2 v_2) - 4\zeta \lambda_3 (\lambda_2 k_x^2 + \lambda_1 k_y^2)]}{4(E^{ML}(\mathbf{k}))^3} \quad (5.19)$$

where $+$ ($-$) represents conduction (valence) band. Now the x component of the velocity of ML graphene can be written as

$$v_x^{ML}(\mathbf{k}, \zeta) = \pm \frac{2\zeta \lambda_3 k_y \mathbf{N}_{2\mathbf{k}} + \mathbf{N}_{1\mathbf{k}}(\zeta v_1 - 2\lambda_2 k_x)}{E^{ML}(\mathbf{k})}. \quad (5.20)$$

We first consider strained ML graphene $v_1 \neq v_2$ without warping i.e., $\lambda_1 = \lambda_2 = \lambda_3 = 0$. It is then clear from the Eq. (5.19) that the BC at two different valleys ($\zeta = \pm 1$) become opposite of each other for both pristine as well as strained ML graphene i.e., $\Omega_z^{ML}(\mathbf{K}, \zeta = +1) = -\Omega_z^{ML}(\mathbf{K}', \zeta = -1)$. Moreover, the BC in this case is directly proportional to the bandgap of the system. On the other hand, $v_x^{ML}(\mathbf{K}, \zeta = +1) = v_x^{ML}(\mathbf{K}', \zeta = -1)$ as evident from Eq. (5.20).

The above discussion refers to the fact that there exists equal number of \mathbf{k} -modes for which $v_x^{ML} > 0$ with both signs of $\Omega(\mathbf{k})$ in each valley. Upon the momentum integration followed by Eqs. (5.13)-(5.14), the MH and MN conductivities for each valley in ballistic regime can be obtained as

$$\sigma_\zeta = \zeta \frac{\Delta_g e^2}{8\pi\mu^2} \Delta U, \quad \alpha_\zeta = \zeta \frac{\Delta_g \pi K_B^2 T e}{12\mu^3} \Delta U. \quad (5.21)$$

Interestingly, the above conductivities are independent of velocities v_1 and v_2 . This leads to the fact that the uniaxial strain does not affect the MH responses in ML graphene in absence of warping $\lambda_{1,2,3} = 0$. Moreover, it is also clear from Eq. (5.21) that the contributions of MH and MN conductivities for two valleys ($\zeta = \pm 1$) are equal and opposite. Therefore, summing over the valleys ($\zeta = \pm 1$), the total MH responses vanishes in the strained ML graphene without λ 's, similar to the case of pristine ML graphene. Instead the valley polarized transport can lead to Magnus valley Hall and Magnus valley Nernst effects where

the electrons with opposite valley index accumulate on the different edges of the sample [277–279]. To be precise, consider a ML graphene system (with $\lambda_{1,2,3} = 0$) with chemical potential $(\mu + \delta\mu/2)$, $(\mu - \delta\mu/2)$ at the $\zeta = \pm 1$ valleys respectively, the total Magnus valley Hall conductivity will be finite and takes the form $\sigma_{\text{valley}} = \sum_{\zeta} \sigma_{\zeta}(\mu + \zeta\delta\mu/2) \simeq \frac{\Delta_g e^2 \Delta U \delta\mu}{4\pi\mu^3}$. Similarly, Magnus valley Nernst conductivity is given by $\alpha_{\text{valley}} = \sum_{\zeta} \alpha_{\zeta}(\mu + \zeta\delta\mu/2) \simeq \frac{\Delta_g \pi K_B^2 T e \Delta U \delta\mu}{4\mu^4}$. We note that in order to observe the above valley polarized ballistic Magnus response, the dimension of the system has to be smaller or comparable to the mean free path.

We shall now discuss the effect of C_3 symmetric warping in MH responses by considering $\lambda_1 = \lambda_2 = \lambda_3 = \lambda \neq 0$. It is clear from the Eq. (5.19) and (5.20) that the BC and velocity of each valley are not equal and opposite compared to unwarped case. The evolution of BC and v_x^{ML} for different strength of λ are depicted in Fig. 5.1 (b)-(d) and Fig. 5.1 (f)-(h) for $\zeta = 1$ and $\zeta = -1$ valleys, respectively. The warping terms introduce satellite Dirac cones with $\theta \rightarrow \theta + 2n\pi/3$ (with $n = 1, 2, 3$) appearing around each Dirac points [280]; here $\theta = \pi$ (0) for valleys $\zeta = +1$ (-1). These additional satellite Dirac cones appear with opposite chirality as compared to that of the parent Dirac cone. The important point to note here is that the relative strength between v_1 and v_2 determines the distance of satellite Dirac points from the parent Dirac point. For example, $v_1 > v_2$ ($v_1 < v_2$) would cause the satellite Dirac points to move more (less) in k_x direction more (less) than k_y direction.

Following the above discussion, it is evident that each valley of ML strained graphene in the presence of warping does not contribute to MH and MN conductivities in an equal and opposite manner that we found for strained ML graphene. As a result, the non-zero MH responses are directly observed by summing over the contribution for both the valleys. The warping results in non-linear and anisotropic dispersion as shown in Eq. (5.17). As a result, BC becomes anisotropic and exhibits rich features over the Fermi surface (see Fig. 5.1). Since the expressions of BC and velocity of ML graphene in the presence of warping are quite complicated, it is very difficult to calculate MH and MN conductivities analytically. Therefore, below we have calculated Magnus responses numerically to investigate in detail.

The valley integrated MH and MN conductivities as a function of chemical potential (μ) are shown in Fig. 5.2 (a) and (b), respectively. We find that the magnitude of both transport coefficients enhances with the increase of warping

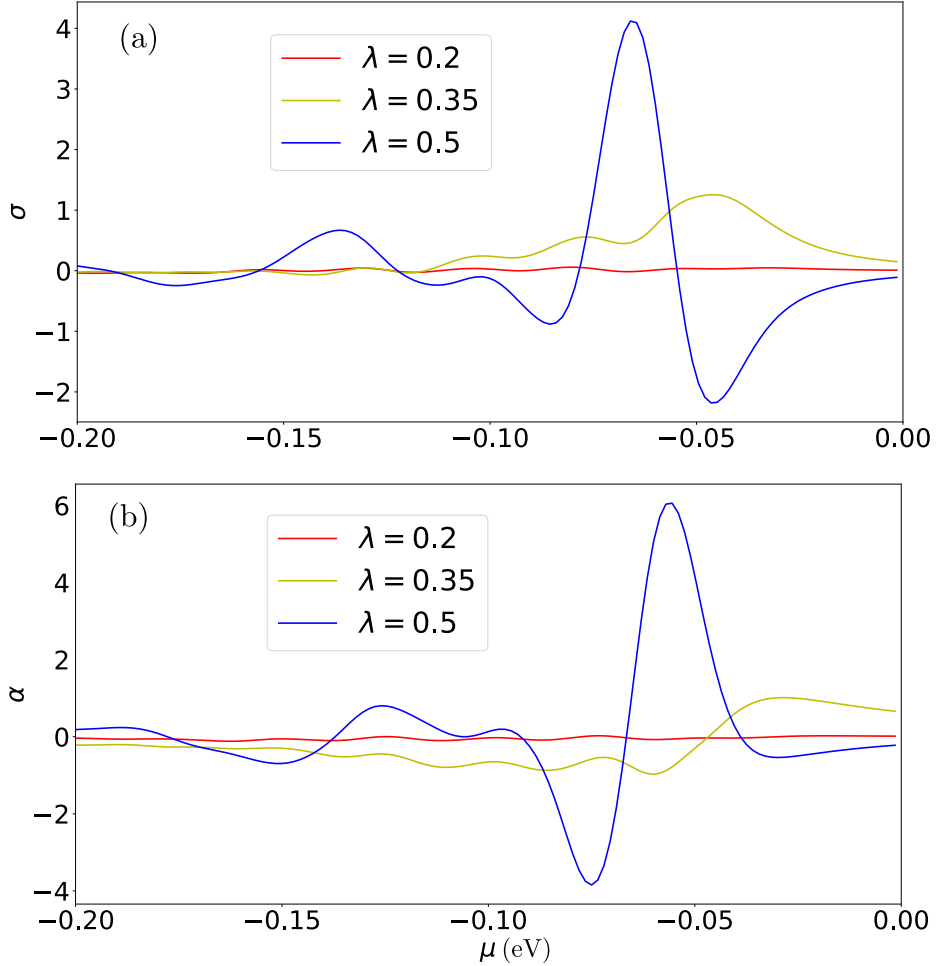


Fig. 5.2 The total valley summed contributions of (a) MH conductivity σ (in the unit of $10^{-3}e^2/$) and (b) MN conductivity α (in the unit of $10^{-5}ek_B/$) in the presence of strain ($v_2 = 2v_1$) for different warping strengths $\lambda = 0.2, 0.35$ and $0.5 \text{ eV}\cdot\text{\AA}^2$ are shown for ML graphene. Noticeably, the warping can enhance the responses even after valley sum is performed, as it generates asymmetric contributions between valleys. We consider $\Delta U = 0.01 \text{ eV}$ and $k_B T = 0.001 \text{ eV}$. All other parameters are kept same as that of in Fig. 5.1. The chemical potential μ is chosen in the unit of eV throughout the paper.

strength for a fixed strain. The window of activated momentum modes over the Fermi surface changes with warping strength. Moreover, band bending imprints its signature through the Fermi surface distribution. All these lead to the intriguing behavior of the response coefficients. We find that MH responses show significant different behaviors for $v_1 > v_2$ as compared to $v_2 > v_1$. This refers to fact that the strain becomes instrumental in controlling the response in presence of warping terms. We would like to point out that the MH and MN conductivities

can acquire both positive and negative values. This is due to the fact that the BC around the additional satellite Dirac points take opposite values as compared to that of the for the parent Dirac point. These are the markedly different responses while the warping terms are introduced in the ML strained graphene. Our study further supports that the Mott relation can successfully describe MN conductivity from MH conductivity even in the presence of warping.

In summary, for monolayer graphene without strain and warping, the MH and MN conductivities for two valleys are equal and opposite, and therefore, summing over the valleys, the total MH responses vanishes [222]. On the other hand, we show that each valley of monolayer strained graphene in the presence of warping does not contribute to MH and MN conductivities in an equal and opposite manner, and hence lead to a finite valley integrated MH response. This happens because the warping results in non-linear and anisotropic dispersion as shown in Eq. (5.17). As a result, BC becomes anisotropic and exhibits rich features over the Fermi surface.

5.3.2 Strained bilayer graphene

The BL graphene belongs to the D_{3d} point group symmetry. In order to study the BC mediated transport properties, one has to break the inversion symmetry by applying an external electric field perpendicular to the layers. This reduces the symmetry of the system from D_{3d} to C_{3v} , and creates a gap Δ_g as well as finite BC. The application of a uniaxial strain further reduces the symmetry of the point group to C_v . The low energy Hamiltonian for an inversion broken BL graphene in the presence of a uniaxial strain is expressed below as [228]

$$\mathcal{H}_0^{BL}(\mathbf{k}) = \frac{\Delta_g}{2}\sigma_z + \left(-\frac{1}{2m}(k_y^2 - k_x^2) + \zeta v k_x + \omega \right) \sigma_x - \left(\frac{1}{m}k_x k_y + \zeta v k_y \right) \sigma_y, \quad (5.22)$$

where v denotes the Fermi velocity related to the skew hopping between the layers, ζ is the valley index and m represents the effective mass dependent on the coupling between the layers. Here, the effect of strain is coming into the Hamiltonian via ω ($= A_3 - A_0$) where A_3 and A_0 are pseudogauge fields. Similar to the ML case, we add trigonal warping terms to the above Hamiltonian

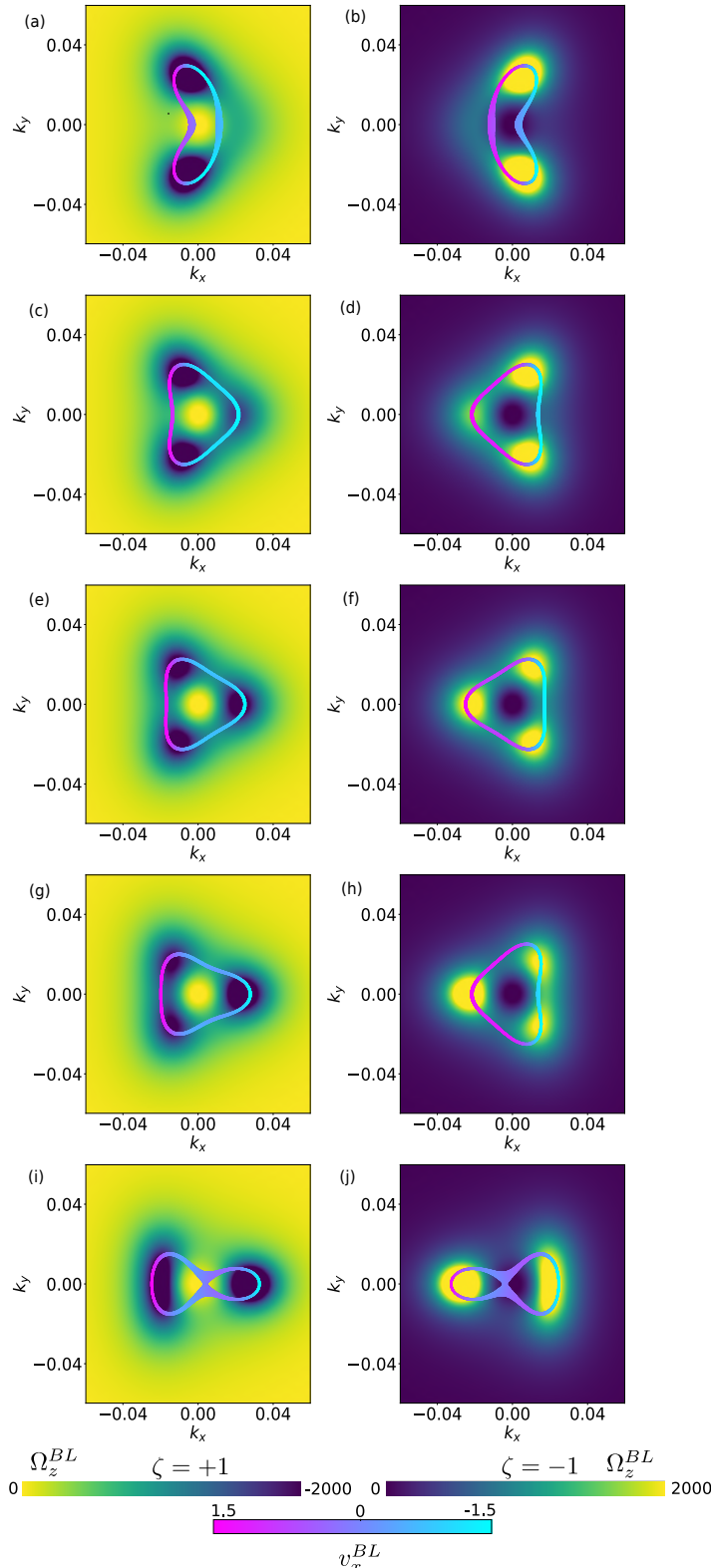


Fig. 5.3 The evolution of BC and Fermi surface in BL graphene (5.23) with strain w for warping $\lambda_1 = \lambda_2 = \lambda_3 = \lambda = 0.001\text{eV}\cdot\text{\AA}^2$. Left column: The BC $\Omega_z^{BL}(\mathbf{k}, \zeta = +1)$ and $v_x^{BL}(\mathbf{k}, \zeta = +1)$ over the Fermi surface of BL graphene (a) $w = -3m$, (c) $w = -m$, (e) $w = 0$, (g) $w = m$ and (i) $w = 3m$ are shown. Right column: We repeat the same set of calculations for $\zeta = -1$ valley. The parameters (in the units of eV) used are $\Delta_g = 0.06\text{eV}$, $m = 0.008\text{eV}\cdot\text{\AA}^2$, and $v = 0.5\text{eV}\cdot\text{\AA}$. The Fermi surface is plotted for the constant energy $E = -0.04\text{ eV}$.

to study its effect. The strained-warped BL graphene Hamiltonian takes the following form

$$\begin{aligned}\mathcal{H}^{BL}(\mathbf{k}) &= \frac{\Delta_g}{2}\sigma_z + \left(-\frac{1}{2m}(k_y^2 - k_x^2) + (\lambda_1 k_y^2 - \lambda_2 k_x^2) \right. \\ &\quad \left. + \zeta v k_x + \omega \right) \sigma_x - \left(\frac{1}{m} k_x k_y + \zeta v k_y - 2\zeta \lambda_3 k_x k_y \right) \sigma_y \\ &= \mathbf{N}_k \cdot \boldsymbol{\sigma}\end{aligned}\quad (5.23)$$

with $\mathbf{N}_k = \{\mathbf{N}_{1k}, \mathbf{N}_{2k}, \mathbf{N}_{3k}\} = \{(\lambda_1 - \frac{1}{2m})k_y^2 + (\frac{1}{2m} - \lambda_2)k_x^2 + \zeta v k_x + \omega, (2\zeta \lambda_3 - \frac{1}{m})k_x k_y - \zeta v k_y, \frac{\Delta_g}{2}\}$. The energy dispersion of the Hamiltonian given in Eq. (5.23) can be obtained as

$$E^{BL}(\mathbf{k}) = |\mathbf{N}_k| = \pm \sqrt{\mathbf{N}_{1k}^2 + \mathbf{N}_{2k}^2 + \mathbf{N}_{3k}^2}. \quad (5.24)$$

Note that in Eq. (5.23), the warping terms are quadratic in momentum, and hence could be absorbed in the already present quadratic momentum terms which indicate interlayer coupling. In this way, the effective masses associated with k_x^2 , k_y^2 and $k_x k_y$ terms are renormalized. Therefore, we can comment at the outset that addition of warping might not affect the system substantially as compared to strain in the ML graphene.

Considering C_3 symmetric warping ($\lambda_1 = \lambda_2 = \lambda_3 = \lambda \neq 0$), the BC for strained BL graphene given in Eq. (5.23) can be calculated as

$$\Omega_z^{BL}(\mathbf{k}, \zeta) = \mp \frac{\Delta_g \left[A(\lambda, k_x)A(\lambda\zeta, k_x) + B(\lambda, k_y)B(\lambda\zeta, k_y) \right]}{4(E^{BL}(\mathbf{k}))^3} \quad (5.25)$$

with $A(x, k_x) = \frac{k_x}{m} - 2xk_x + \zeta v$, $B(x, k_y) = \frac{k_y}{m} - 2xk_y$. where $- (+)$ represents conduction (valence) band. The velocity $v_x^{BL}(\mathbf{k}, \zeta)$ takes the form

$$v_x^{BL}(\mathbf{k}, \zeta) = \pm \frac{A(\lambda, k_x)\mathbf{N}_{1k} - B(\lambda\zeta, k_y)\mathbf{N}_{2k}}{E^{BL}(\mathbf{k})}. \quad (5.26)$$

A close inspection suggests that the strain factor w does not appear in the numerator of BC for BL graphene unlike the ML graphene where warping factors λ 's come as corrections over the strain factors $v_1 v_2$. The strain factor comes in the denominator of BC through the energy of the BL graphene. Therefore, the

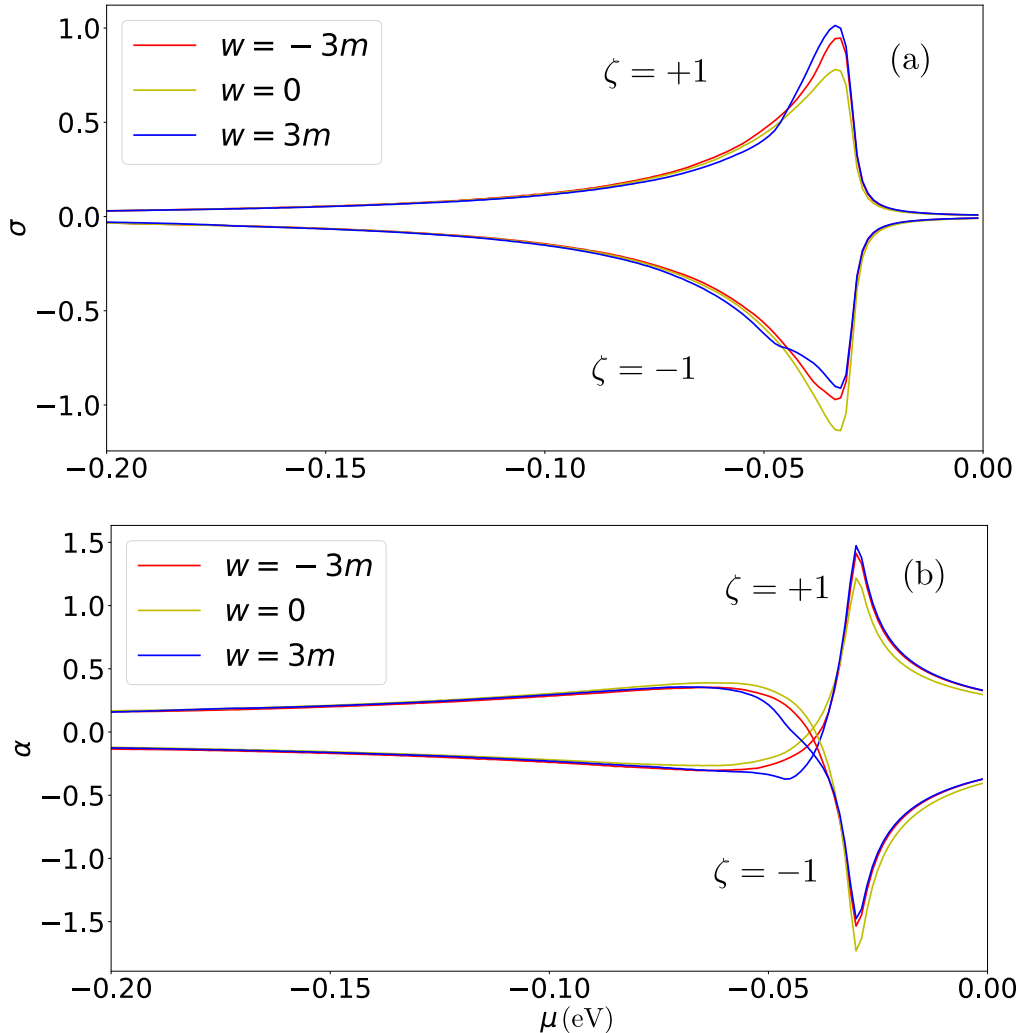


Fig. 5.4 Valley responses of (a) MH (in the unit of $10^2 e^2 /$), (b) MN (in the unit of $10^{-1} e k_B /$) conductivities in BL graphene with $\Delta U = 0.01$ eV, and $k_B T = 0.001$ eV for $w = -3m, 0, 3m$. All other parameters are kept same as that of in Fig. 5.3. The prominent and asymmetric valley responses in presence of strain for BL graphene are markedly different from the symmetric responses for ML graphene.

evolution of BC with strain for BL graphene will be significantly different from ML graphene.

The evolution of the $\Omega_z^{BL}(\mathbf{k}, \zeta)$, $v_x^{BL}(\mathbf{k}, \zeta)$ and Fermi surface under strain for valley $\zeta = +1$ and valley $\zeta = -1$ are shown in left and right column of Fig. 5.3, respectively. For $w = 0$, the three leg gapped Dirac cones (one along $k_y = 0$ and the other two symmetrically placed around $k_x = 0$ line) are observed at $\theta \rightarrow \theta + 2\pi/3$ with $\theta = 0$ following the C_3 symmetric warping [281]. The BC does not change its sign for the three leg gapped Dirac cones within a given valley. This structure of BC for BL graphene is very different from the ML graphene, where BC around satellite Dirac nodes reverses its sign as compared to the parent Dirac node within a given valley. For $w \leq -3m$, there exist two symmetrically placed Dirac cones around $k_y = 0$ line, while two cones appears on the $k_y = 0$ line for $w \geq 3m$. The threefold rotational symmetry is lost in the presence of uniaxial strain. Interestingly, the Fermi surface is also deformed for the strained case from its unstrained triangular distribution. To be precise, a singly connected Fermi surface for the unstrained case splits into disconnected ones for sufficiently large values of strain. The shape and orientation of the Fermi surfaces appear to be different for larger strain in opposite valleys, which leads to non-identical MH responses in these valleys.

We now investigate the MH and MN conductivities for the individual valleys as shown in Fig. 5.4 (a) and (b), respectively. The unstrained case leads to asymmetric response in the valleys which is markedly different from ML strained graphene without warping. Upon inclusion of strain, we find that the positive MH responses for the valley $\zeta = +1$ is more pronounced than the negative responses for the other valley $\zeta = -1$. This is due to the fact that activated momenta over the Fermi surface do not have exactly opposite BC in terms of their magnitudes and sign. Moreover, the peak or dip of MHC do not appear at the same chemical potential μ . The Fermi surface distribution strongly depends on valley as well as strain explaining the above observation for MH responses. Therefore, valley polarized transport can in principle be possible like ML strained graphene.

The total valley integrated Magnus responses for BL graphene are shown in Fig. 5.5 by varying strain parameter w . For negative values of strain parameter i.e., $w < 0$, MH conductivity always acquires negative values and a dip appears at a certain μ value. The height of the dip increases and its position moves toward $\mu \rightarrow 0$ with decreasing negative strain. On the other hand, by changing the sign of strain i.e., $w > 0$, the dip structure of MH conductivity gets bifurcated

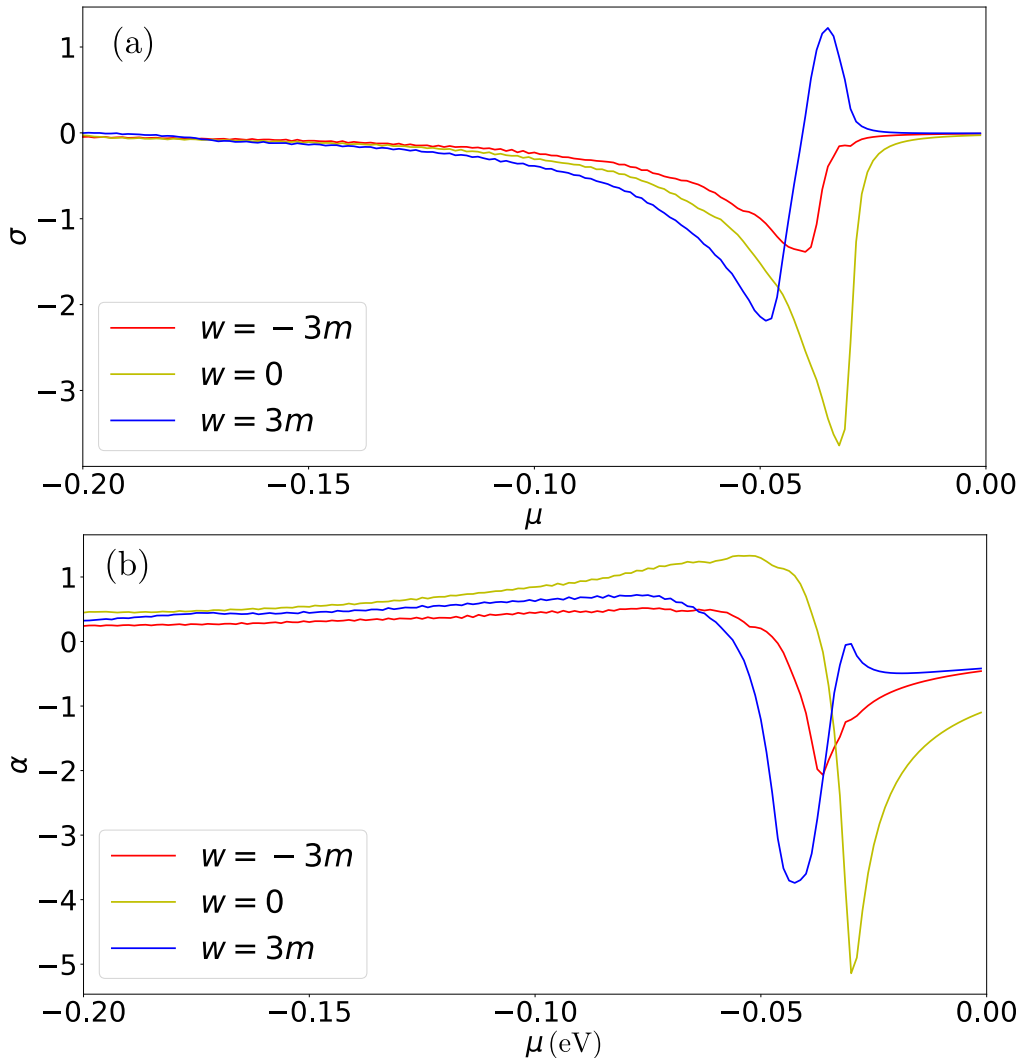


Fig. 5.5 Valley summed (a) MH (in the unit of $10e^2/$), (b) MN (in the unit of $10^{-2}ek_B/$) conductivities in BL graphene for $w = -3m, 0, 3m$. The transport behavior changes with strain substantially. We consider the same parameters as used in Fig. 5.4.

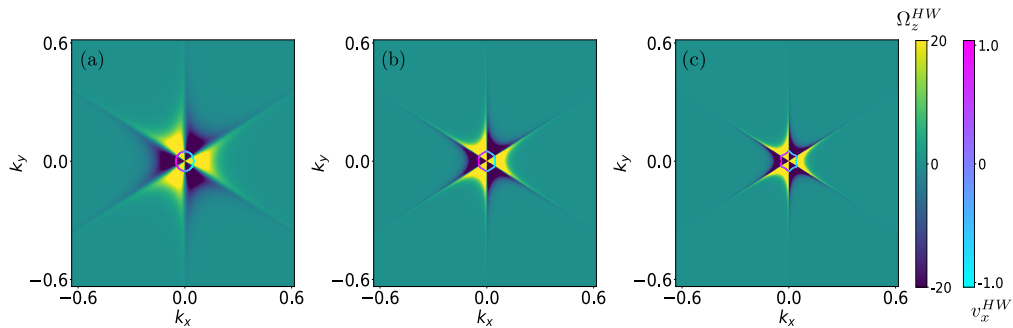


Fig. 5.6 Evolution of BC and Fermi surface, calculated from Eq. (5.27), with different warping strengths (a) $\lambda=50$ eV·Å³, (b) $\lambda=200$ eV·Å³ and (c) $\lambda=400$ eV·Å³ are shown. Fermi surface is plotted for $E=-0.05$ eV. We note that for $\lambda=50$ eV·Å³, the Fermi surface remains circular, which gradually evolves to hexagonal shape with increasing λ . We consider $v=1$ eV·Å and $E_0=0$ in our calculation.

into a dip and peak structure. The valley polarized structure of MH responses can explain these observations. We notice qualitatively similar response in MN conductivity.

In summary, for bilayer graphene, we find that strain enhances asymmetry between the valley polarized contribution, resulting in distinct transport signatures for positive and negative strain as compared to the unstrained bilayer graphene.

5.3.3 Hexagonal warped topological insulator

We consider the two-dimensional surface Hamiltonian of a TRS invariant TI namely, *Bi*₂*Te*₃, hosting a unique Fermi surface that encloses an odd number of Dirac cones in the surface Brillouin zone. The spin-orbit coupling that is the linear order term in k leads to the band inversion in this system. The minimal two band model contains cubic terms in k in addition to the linear terms in k . This warping can be considered as a counterpart of cubic Dresselhaus spin-orbit coupling term. We note that hexagonal warping incorporates one order higher momentum coupling than the trigonal warping terms. This further allows us to investigate the non-trivial effects of this term that are not captured by the trigonal warping terms.

Considering the threefold rotation C_3 around the z axis and mirror symmetry M : $x \rightarrow -x$, the low-energy model around the gapless Γ point thus reads [230]

$$H^{HW}(\mathbf{k}) = E_0(\mathbf{k}) + v(k_x\sigma_y - k_y\sigma_x) + \frac{\lambda}{2}(k_+^3 + k_-^3)\sigma_z, \quad (5.27)$$

with $E_0(\mathbf{k}) = \frac{k^2}{2m^*}$ causes the particle-hole asymmetry. Dirac velocity v can be considered k independent without loss of generality. Here $k_{\pm} = k_x \pm ik_y$ and λ is the strength of hexagonal warping.

The energy spectrum becomes

$$E^{HW}(\mathbf{k}) = E_0(\mathbf{k}) \pm \sqrt{v^2 k^2 + \lambda^2 k^6 \cos \phi}, \quad (5.28)$$

where $\phi = \arctan \frac{k_y}{k_x}$. Using Eq. (5.18), the BC and x -component of the velocity for the above Hamiltonian can be obtained as

$$\Omega_z^{HW}(\mathbf{k}) = \pm \frac{\lambda v^2 (3k_x k_y^2 - 2k_x^3)}{2(v^2 k^2 + \lambda^2 k^6 \cos \phi)^{\frac{3}{2}}} \quad (5.29)$$

$$v_x^{HW}(\mathbf{k}) = \frac{k_x}{m^*} \pm \frac{2v^2 k_x + \lambda^2 k^3 k_y^2 + 6\lambda^2 k^4 k_x \cos \phi}{2\sqrt{v^2 k^2 + \lambda^2 k^6 \cos \phi}}. \quad (5.30)$$

where $+(-)$ represents conduction (valence) band. The band structure is sixfold symmetric under $\phi \rightarrow \phi + 2\pi/6$. It is clear from the Eq. (5.29) that the BC is zero in the absence of warping. The band structure is sixfold symmetric under $\phi \rightarrow \phi + 2\pi/6$. The BC distribution with different strength of warping parameter is depicted in Fig. 5.6. The BC always shows a snowflake like distribution irrespective of the strength of warping. However, the BC acquires substantially large value around the Γ point with increasing λ as also suggested from Eq. (5.29). Moreover, it reverses sign between two subsequent interval $2n\pi/6 \rightarrow 2(n+1)\pi/6$. On the other hand, the shape of the Fermi surface changes with warping. Specifically, for small warping the Fermi surface takes circular shape. With increasing warping strength, it becomes non-circular with relatively sharp tips extending along high symmetry direction and curves inward in between. Such transformation of Fermi surface from circular to snowflake would initiate interesting transport behavior which we discuss below.

The MH and MN conductivities as a function of chemical potential for different strengths of warping parameter are shown in Fig. 5.7 (a) and (b), respectively. We find that the magnitude of the MH responses are increasing as well as become more pronounced and sharp with the increase of warping strength. In addition, the position of the dips (peaks) in MH (MN) conductivities moves toward $\mu = 0$ with increasing λ . Moreover, the negative sign of MH

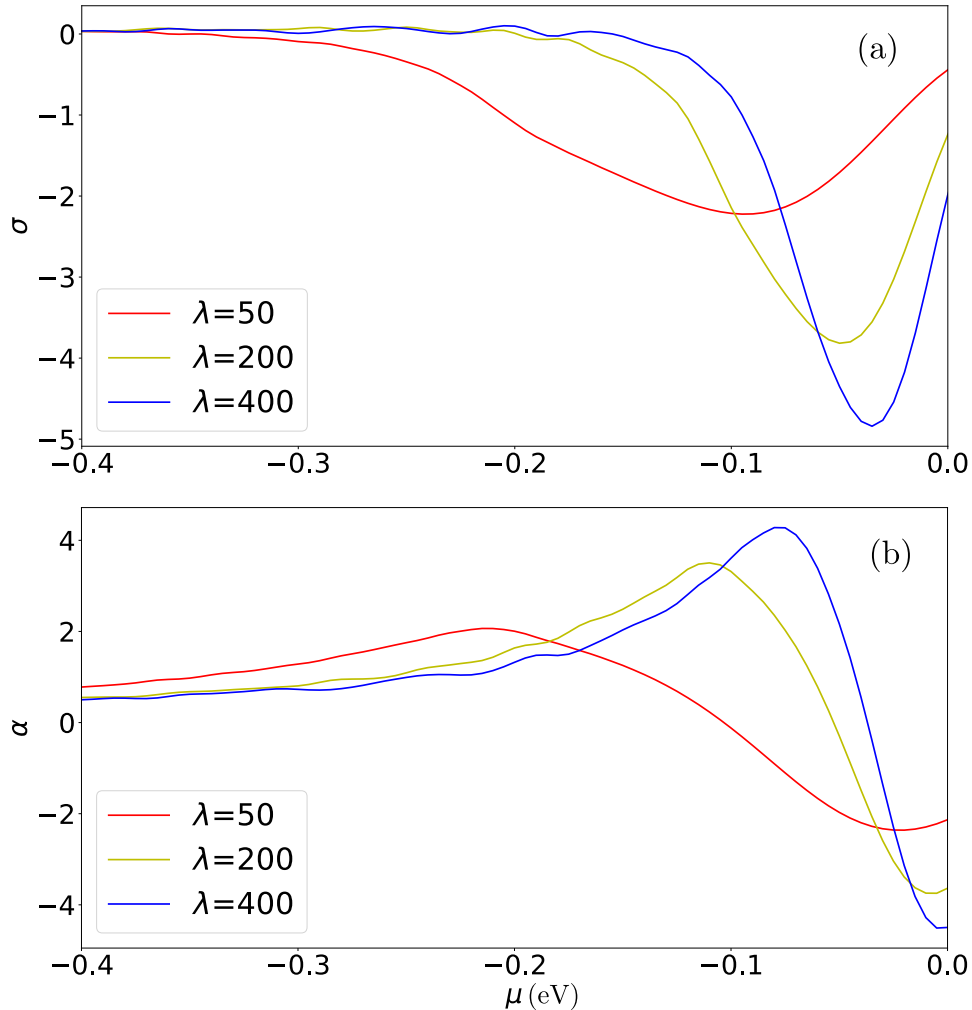


Fig. 5.7 (a) MH (in the unit of $10^{-2} e^2 / \Omega$) and (b) MN (in the unit of $10^{-4} e k_B / \Omega$) conductivities as a function of chemical potential for different warping strength $\lambda = 50, 200$ and 400 eV·Å³ are depicted. The parameters used are $v=1$ eV·Å, $\Delta U = 0.01$ eV, and $k_B T = 0.001$ eV.

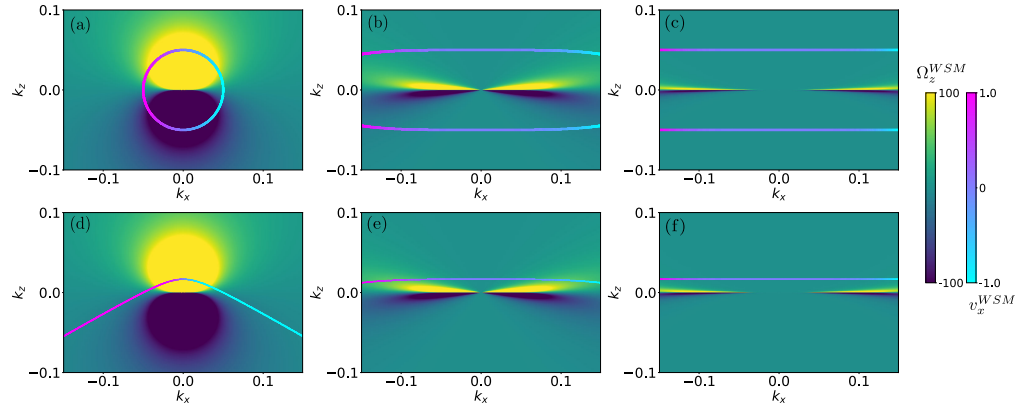


Fig. 5.8 The distribution of the BC and the Fermi surfaces, calculated from Eq. (5.31), in (a) [(d)] single Weyl node with $n = 1$, (b) [(e)] double Weyl node with $n = 2$ and (c) [(f)] triple Weyl node with $n = 3$ for untilted case i.e., $C_+ = 0$ [tilted case i.e., $C_+ = 2.0$] are shown. The Fermi surface is calculated for $E = -0.05$ eV with $v = 1$ eV·Å. The deformation of BC is clearly observed with increasing non-linearity and anisotropy in the WSM.

conductivity appears because of the majority of negative BC over the activated momentum modes in the Fermi surface.

5.3.4 Weyl semimetals

Going beyond the 2D systems, we will now calculate MH responses in 3D WSMs which can be thought of as a 3D analogue of graphene [282]. The low-energy effective Hamiltonian describing the Weyl node with topological charge n and chirality ζ is written as [243, 283–285]

$$H_{\mathbf{k}}^{\zeta} = C_{\zeta}(k_z - \zeta Q) + \zeta \alpha_n \boldsymbol{\sigma} \cdot (\mathbf{n}_{\mathbf{k}} - \zeta \mathbf{e}). \quad (5.31)$$

where $\zeta = \pm 1$, $k_{\perp} = \sqrt{k_x^2 + k_y^2}$, $\phi_k = \arctan(k_y/k_x)$ and $\mathbf{e} = (0, 0, Q)$. The Weyl nodes of opposite chirality are shifted by an amount $\pm Q$ in momentum space due to broken TRS. C_{ζ} indicates the tilt parameter associated with Weyl node with chirality ζ . Here, $\boldsymbol{\sigma} = \{\sigma_x, \sigma_y, \sigma_z\}$ and $\mathbf{n}_{\mathbf{k}} = \{\alpha_n k_{\perp}^n \cos(n\phi_k), \alpha_n k_{\perp}^n \sin(n\phi_k), v k_z\}$. The factor α_n bears the connection to the Fermi velocity. v is equivalent to the velocity associated with z -direction. For the sake of simplicity, we consider $Q = 0$ and take into account the Weyl nodes of opposite chirality separately. For $C_{\zeta} = 0$, electron and hole bands touch at the Weyl point leading to a point-like Fermi surface. When the magnitude of the tilt parameter is small enough i.e.,

$|C_\zeta|/v \ll 1$, the Fermi surface is still point-like, and is characterized as the type-I Weyl node. With the increase of C_ζ , electron and hole pockets now appear at the Fermi surface for $|C_\zeta|/v \gg 1$ leading to a distinct phase, which is designated as a type-II Weyl node. In this work, we consider two types of tilt configuration for the WSM: i) chiral tilt i.e., $C_+ = -C_-$, and ii) achiral tilt i.e., $C_+ = C_-$.

Now the energy dispersion of the multi-Weyl node with $\zeta = +1$ is given by

$$E^{WSM}(\mathbf{k}, \zeta) = C_\zeta k_z \pm \epsilon_{\mathbf{k}} \quad (5.32)$$

where $\epsilon_{\mathbf{k}} = \sqrt{\alpha_n^2 k_\perp^{2n} + v^2 k_z^2}$ and $+(-)$ represents conduction (valence) band. It is now clear that the dispersion around a Weyl node with $n = 1$ is isotropic in all momentum directions. On the other hand, for $n > 1$, we find that the dispersion around a double (triple) Weyl node becomes quadratic (cubic) along both k_x and k_y directions whereas varies linearly with k_z .

Using Eq. (5.18), the explicit form of z -component BC associated with the multi-Weyl node can be written as

$$\Omega_z^{WSM}(\mathbf{k}, \zeta) = \pm \frac{1}{2} \frac{\zeta n^2 v \alpha_n^2 k_\perp^{2n-2}}{\epsilon_{\mathbf{k}}^3} k_z. \quad (5.33)$$

It is clear from the Eq. (5.33) that, similar to energy dispersion, the BC is isotropic in all momentum directions for single WSM whereas it becomes anisotropic for WSMs with $n > 1$ i.e., for double WSM ($n = 2$) and triple WSM ($n = 3$) due to the presence of k_\perp^{2n-2} factor and topological charge n . Moreover, the BC reverses its sign, retaining the magnitude same, for Weyl nodes of opposite chiralities $\Omega_z^{WSM}(\mathbf{k}, \zeta = +1) = -\Omega_z^{WSM}(\mathbf{k}, \zeta = -1)$. The behavior of BC for both untilted ($C_\zeta = 0$) and tilted ($C_\zeta \neq 0$) multi-Weyl node with $\zeta = +1$ are shown in Fig. 5.8. With increasing the topological charge n , the single positive and negative lobe of BC gets divided into one pair of lobes. These lobes for $n = 2$ and 3 are deformed with respect to that of $n = 1$. The separation between these lobes increases over the $k_z = 0$ line. The BC changes sign with the chirality of the Weyl node for all WSMs as indicated in Eq. (5.33). However, the BC is identical in both tilted and untilted WSMs because the tilt does not effect BC. On the other hand, in contrast to BC, the Fermi surface drastically changes in tilted WSM compared to untilted WSM as shown in Fig. 5.8.

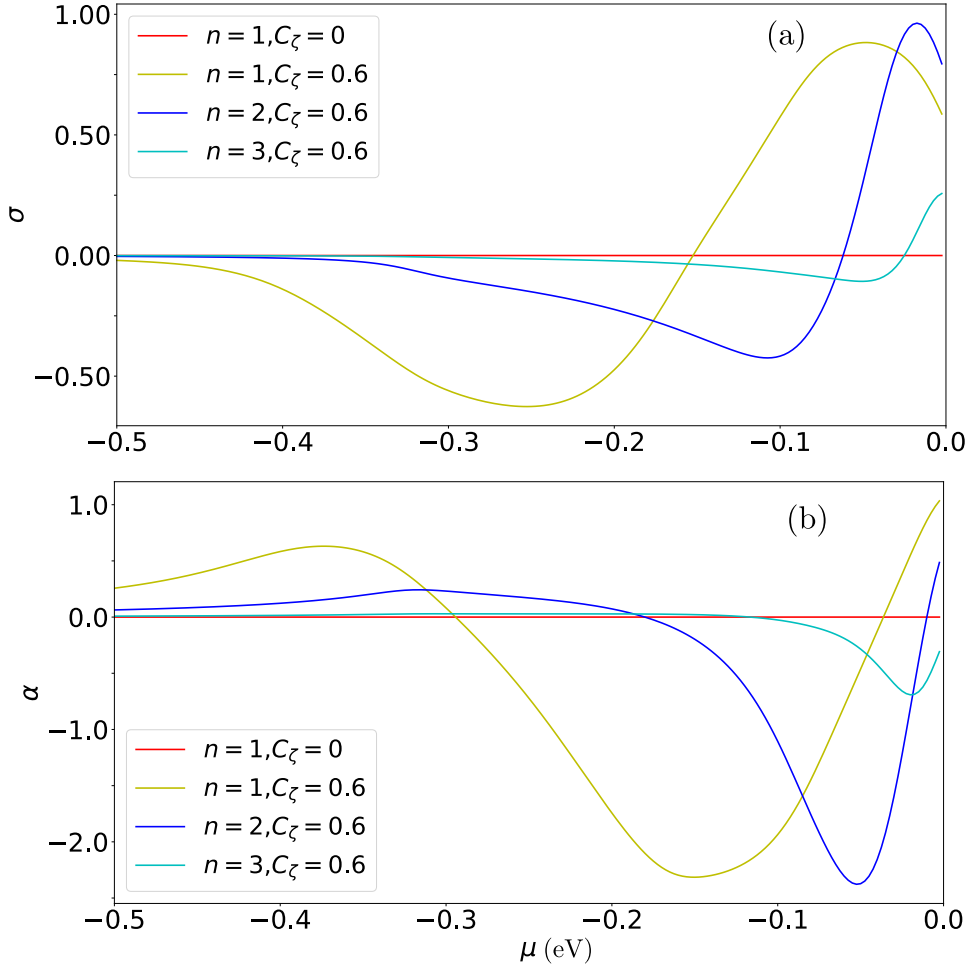


Fig. 5.9 (a) MH (in the unit of $10e^2/$) and (b) MN (in the unit of $ek_B/$) conductivities are shown for tilted and untilted Weyl nodes with $\zeta = +1$. We consider $v = 1$ eV·Å, $\Delta U = 0.01$ eV, and $k_B T = 0.001$ eV. We observe that the untilted Weyl node with $C_+ = 0$ (tilted Weyl node with $C_+ = 0.6$) results in null (substantial) Magnus responses. We note that MH and MN conductivities are exactly opposite at two opposite Weyl nodes with $\zeta = +1$ and -1 owing to the anti-symmetric nature of BC (Eq. (5.33)).

The x -component of the quasi-particle velocity associated with the multi-Weyl node is given by

$$v_x^{WSM}(\mathbf{k}, \zeta) = \frac{k_x n \alpha_n^2 k_\perp^{2n-2}}{\epsilon_{\mathbf{k}}}. \quad (5.34)$$

A close inspection suggests that x -component of the velocity is also independent of the tilt parameter C_ζ (chirality ζ) like (unlike) the BC. Therefore, the effect of the tilt is only incorporated by the Fermi surface properties. The Fermi

surface for $n = 1$ case is circular in shape that gets elongated along k_x direction with increasing n . In the $k_x - k_z$ plane, Fermi surface does not close that is in accordance with the non-point like nature of Fermi surface for tilted WSM. With increasing topological charge n , Fermi surface gets flattened. Therefore, tilt and non-linear dispersion imprint their signature in the transport through Fermi surface properties.

The numerically computed MH responses for single, double and triple Weyl node as a function of μ are shown in Fig. 5.9. Interestingly, we find that both MH and MN conductivities vanish identically for untilted Weyl node. This is due to the fact that, for a given untilted Weyl node, the positive and negative BC for the activated momentum modes over the Fermi surface are equal, which results in a complete cancellation. This situation remarkably changes in the presence of tilted Weyl node. In this case, the positive and negative BC for the activated momentum modes over the Fermi surface are unequal, and therefore, do not cancel each other completely.

The MH conductivity of a tilted WSM, considering the contribution from two opposite chirality nodes, is given by $\sigma = \sum_{\zeta} G(\mu) \zeta C_{\zeta}$, where $G(\mu)$ is μ dependent part of transport coefficient associated with individual Weyl node. For a pair of Weyl nodes at same energy E_0 such that $G(\mu = E_0) = G_0$, the MHE is only finite when relative sign of the tilt parameter between them is opposite, referring to the chiral tilt configuration ($C_+ = -C_-$). On the other hand, the MHE vanishes in the absence of tilt ($C_+ = C_- = 0$), and even in the presence of achiral tilt ($C_+ = C_-$) of the Weyl node. In other words, MH responses from opposite Weyl node add up (cancel each other) leading to a node integrated (polarized) Magnus (Magnus valley) response in presence of chiral (achiral) tilt. Two Weyl nodes of opposite chirality, residing at two different energies E_+ and E_- , can in principle lead to Magnus valley Hall effect while Weyl nodes exhibit achiral tilt such that $G(\mu = E_+) \neq G(\mu = E_-)$. The MNE follows the same behavior as MHE. This is because the sign of BC is opposite whereas the v_x^{WSM} has same sign for two different nodes of opposite chirality. To shed more light into the tilt mediated MH response, we show the systematic growth of MH conductivity while increasing the tilt strength in Fig. 5.10.

Therefore, the MH and MN conductivities can become useful probes in distinguishing tilted WSM from an untilted WSM in experiments. We also notice that the responses for $n = 1$ single WSM is found to be most prominent as compared to the WSMs with $n > 1$. This can be explained as the BC reduces

its value for the activated momentum modes over the Fermi surface. Moreover, the MH responses decrease as the Fermi surface becomes more flattened for mWSMs. Another interesting feature, coming out from Eq. (5.33) and (5.34), is that MH responses from two opposite nodes with chiral (achiral) tilt simply add up (cancel each other) leading to a finite node integrated (polarized) transport coefficients similar to the Magnus (Magnus valley) responses for ML graphene in presence (absence) of warping. From low energy model, it can be shown that the node integrated MH responses are proportional to that of a single tilted Weyl node. All these findings together refer to very interesting Magnus transport properties of WSM in general.

It is pertinent to discuss the anomalous Hall effect that will present alongside with the MHE for the TRS broken WSM as far as the first order responses are concerned. The anomalous Hall conductivity for type-I mWSM is found to be $\sigma' \propto n\Delta k$, where Δk is the separation between two Weyl nodes in momentum space of opposite chirality [286, 263]. On the other hand, the MHE in type-I mWSM ($|C_\zeta/v| \ll 1$) for a given chmeical potential can be analytically found as $\sigma \propto n\frac{\Delta U}{v}$. It is clear from the above expressions that the intrinsic AHE increases with increasing the k -space separation between Weyl nodes while remains insensitive to the tilt parameter. By contrast, the magnitude of MH conductivity increases with increasing the built-in electric field. Using the above expressions, one can in general find $\frac{\sigma}{\sigma'} \propto \frac{\Delta U}{v\Delta k}$ (in an arbitrary unit) for type-I WSM. Since this comparison is based on the low-energy model of mWSM, one should consider the lattice model to make a correct estimate of $\frac{\sigma}{\sigma'}$. In addition, we would like to point out that the intrinsic linear AHE can in principle be found to be quantized while MHE is not expected to exhibit quantized response [287].

5.4 Conclusions

In conclusion, we first investigate the effect of strain and warping on MHE and MNE in ballistic regime for 2D topological systems such as ML, BL graphene and surface states of TIs. We find that in strained ML graphene system without warping, the total Magnus responses are zero after summing over the valleys because the contribution from the each valley cancels with each other. One instead obtains Magnus valley Hall and Magnus valley Nernst effects from the valley polarized contribution. Interestingly, we find that the warping leads to finite total Magnus responses as BC contributions from each valley to Magnus

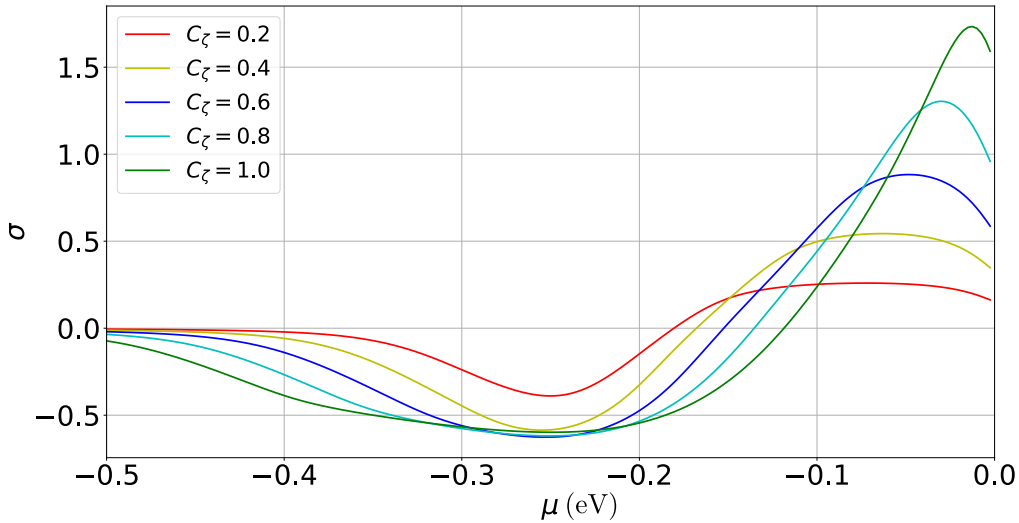


Fig. 5.10 (a) MH (in the unit of $10e^2/\text{\AA}$) conductivity is shown for different strengths of the tilting parameter (C_+) for fixed $n = 1$. Gradual increase in the response is observed with increasing tilt strength C_+ . All other parameters are kept same as mentioned in Fig. 5.9.

responses are unequal and do not cancel with each other for the asymmetric nature of Fermi surface shape. The magnitude of the total Magnus responses is found to increase with increasing the strength of warping parameter. For BL graphene, strain enhances asymmetry between the valley polarized contribution resulting in distinct transport signatures for positive and negative strain, while the effect of warping remains minimal. In the case of surface states of TI, we find that the magnitude of both MH and MN conductivities enhance with increasing the hexagonal warping strength.

Going beyond 2D, we study Magnus responses in ballistic regime for 3D Weyl semimetals using low-energy model to probe the effect of tilt and anisotropic nonlinear dispersion. In particular, we find that the MHE is identically zero for each Weyl node without tilt, whereas for tilted WSMs, Magnus responses coming from the nodes acquire finite values. Notably, MH responses from opposite Weyl node add up (cancel each other) leading to a node integrated (polarized) Magnus (Magnus valley) response in presence of chiral (achiral) tilt. The magnitude of both MH and MN conductivities increase with increasing the tilt parameter of the Weyl nodes. Moreover, with increasing the topological charge associated with Weyl node, the Magnus responses get suppressed. This key feature can be a useful probe in distinguishing untilted (type-I), tilted (type-I or type-II) WSM and the non-linearity in the dispersion through experiments.

Moreover, from the application point of view, such MH responses can pave the way for a new generation of current rectification devices where the alternating-current signal is converted into a direct-current signal. This is due to the fact that linear Hall effects, the transverse MH voltage (say in y -direction) is developed due to the Magnus velocity of the carriers having positive longitudinal velocity ($v_x > 0$) only.

Related to the experimental realization of MH response in 3D, we would like to first point out that the bulk quantum Hall effect has been realized earlier in quasi-2D systems [288–290]. Recently, 3D systems, such as ZrTe_5 , HfTe_5 , and Cd_3As_2 have been shown to exhibit quantum Hall effect in experiments [291–294]. Moreover, non-linear Hall effect has already been experimentally observed in bilayer non-magnetic quantum material WTe_2 [214], in few layer of WTe_2 [295], and in type-II WSM at room temperature [296]. In light of the above experiments, it is in principle possible to extend the non-linear Hall effect setup, fabricated in 2D, to 3D platforms, where MHE can be experimentally observed. For example, 2D systems can be stacked together in order to form quasi-2D / 3D structure over which multi-terminal Hall measurements can be performed. In the case of MHE, the choice of suitable gate potentials, causing the built-in electric field become very important to generate the appropriate transverse Hall voltage.

In contrast to the linearized model we use in this work, a real mWSM may contain Weyl nodes with different tilt with respect to one another as well as number of pair of nodes can be greater than one. One of the interesting extensions of this work would be to implement the MH responses calculation on a real mWSM material using DFT or at least on a lattice model in order to directly compare with the experiments. For this purpose, one can perform a four terminal Landauer-Büttiker conductance calculation [297] on a lattice. Following our theoretical analysis on mWSMs, we expect MH responses to be negligible for materials like NbAs , TaAs , which have symmetric untilted Weyl cones. On the other hand, type-II Weyl materials (MoTe_2 , WTe_2) can show substantial MH responses. Moreover, investigating MH responses in twisted BL graphene would be an interesting direction which we leave for future study.

Chapter 6

Conclusion and Outlook

Discovery of topological insulators has immensely impacted the transport properties in solid state systems. At the interface of a topological material and vacuum, one can find robust boundary states giving rise to dissipationless conductance. This motivates us to explore the possible material realizations for the use of practical purposes. In this dissertation, we have largely explored such realization of topological materials with the help of density functional theory (DFT) and tight-binding (TB) model calculations.

In chapter two, we discovered that multilayer graphene with alternatively doped spacer layer can realize topological crystalline insulating phase in presence of reflection symmetry. We investigated both scenario which arise depending on the chemical nature of the spacer layer. Firstly, in case the spacer layer, used for doping is made of light atoms, the stacked graphene system can show quantum Hall nature in presence of orbital magnetic field. In this regime, presence of reflection symmetry about a layer gives rise to Chern insulating -topological crystalline insulators (TCI). On the other hand, when the spacer layer consists of heavier atoms, it can substantially induce spin-orbit coupling in the graphene layers. This brings the system into the quantum spin-Hall insulators regime. In this limit as well, we prove the existence of gapless surface states in presence of reflection symmetry. Graphene being one of the most studied and easily synthesizable systems, this work motivates the realization of graphene based TCI in the lab.

Quantum spin Hall materials with large band gap are handful in numbers. Jacutingaite being one of them with considerably large band gap (0.5eV), in chapter three, we had set out to explore the topological phases of its multilayer structure. We found that multilayer system of Jacutingaite mineral can feature

dual topology, namely by showing both weak topological (WTI) and TCI phases. The WTI phase is protected by translational symmetry along the stacking direction of the two dimensional layers. This results in even number of Dirac cones on the side surfaces of the material. Interestingly, in addition to the side surfaces, we found that the top surfaces can even be gapless, and show mirror symmetry protected Dirac cones. On the top surface, three mirror planes in total give rise to six number of gapless Dirac cones. Following our theoretical work, these gapless Dirac cones were also found experimentally. Moreover, our work presented a new tight-binding model which captured the dual topology in real materials.

Following this, in chapter four, we focused on the topology of three dimensional (3D) cubic half-heusler (hH) materials falling under the space group 216. In literature, strain driven topological phases has been captured before in HgTe, and other materials which also belong to space group 216. Very recently, theoretically it has been proposed that a similar class of systems can show higher order topological phases, i.e. $(d - 2)$ dimensional states along the boundaries of the d dimensional system. So, we took two 3D hH materials, namely LiBiZn (band inverted) and LiSbZn (band trivial), and showed the existence of hinge modes. In case of LiBiZn, we found that presence of topological surface states obscure the realization of higher order hinge modes. Whereas for the latter material, as the surface is gapped, it showed cleaner hinge modes. From this we concluded that the band trivial hH features promising hinge modes for transport as opposed to the band inverted hH, as for the latter gapless surface states became the hinderers. This work also presented a general wannier based eight bands tight-binding model, which could be applied for the material class with space group 216.

In chapter five, we took a slightly different turn and ventured into the realm of a topological transport called Magnus Hall effect. Berry curvature (BC) mediated topological transport has been explored intensely in the literature. Recently, it has been shown that time reversal symmetric, but inversion broken systems with built-in electric field can show an interesting BC mediated non-trivial linear Hall like response, termed as Magnus Hall response. The response here is caused by the Magnus velocity of the electrons that is proportional to the built-in electric field. In this work, we investigated the effect of strain and warping in case of two dimensional monolayer and bi-layer graphene systems. Warping effect on the Magnus response for the surface of a topological insulator was also explored. And finally, in this work, we had extended the Magnus response to the three

dimensional Weyl semimetal (WSM), where we showed that tilt parameter is important to generate finite Magnus Hall response, as untilted WSMs give null Magnus Hall response.

Based on the work presented in this dissertation, there could be several directions which are worthy of pursuit. Firstly, in the context of TCIs, one can explore the robustness of the topological boundary states by incorporating the disorder into the system. In real life, materials are prone to have defects and impurities which may break the crystal symmetry responsible to protect the TCI phase. So, understanding the effect of disorder on TCIs could be an interesting direction to explore.

Search for the higher order topological materials is very active at the moment. Following the work done on hH materials, an interesting direction would be to search for higher order topological superconducting materials in this hH class. Materials like YPtBi, LuPtBi, LnPtBi are already known examples of superconducting hHs [298–302]. However, higher order topological nature is not yet well explored in these systems.

This dissertation touched upon Magnus Hall response in graphene and Weyl systems. Recently, twisted bilayer graphene systems have also gained enormous interests. A promising direction would be to study the Magnus Hall response in twisted Weyl materials, or twisted bilayer graphene systems in presence of strain. Strain induced nonlinear Hall effect has already been studied [303]. As strain has an immediate anisotropic effect on the Fermi surface of the material, it can also possibly lead to interesting Magnus Hall response.

Finally, this thesis dealt with the non-interacting time-independent topological systems. Topology for time-dependent systems is also very rich (known as *Floquet topological insulators*: FTI), and show properties which have no counterpart in static systems. What makes it more interesting is that FTIs can be easily manipulated in various setups such as in ultracold atoms, photonic waveguides etc [304–308]. It would be really interesting to combine the topology protected by crystalline symmetry with the Floquet topology, and pursue TCI nature in FTIs.

Publications

1. Sanjib Kumar Das, Binghai Yan, Jeroen van den Brink, and Ion Cosma Fulga “[Topological crystalline insulators from stacked graphene layers](#)” *Phys. Rev. B* **99**, 165418 (2019). The content of Chapter 2 has been published in this paper.
2. Jorge I. Facio, Sanjib Kumar Das, Yang Zhang, Klaus Koepernik, Jeroen van den Brink, and Ion Cosma Fulga, “[Dual topology in jacutingaite \$Pt_2HgSe_3\$](#) ” *Phys. Rev. Materials* **3**, 074202 (2019). The content of Chapter 3 has been published in this paper.
3. Sanjib Kumar Das, Ion Cosma Fulga, Rakshanda Dhawan, Hem C. Kandpal, Jeroen van den Brink, and Jorge I. Facio, “[Hinge electronic structure of strained half-Heuslers](#)”. The manuscript regarding the content of Chapter 4 is in preparation for submission.
4. Sanjib Kumar Das, Tanay Nag, and Snehasish Nandy “[Topological Magnus responses in two- and three-dimensional systems](#)” *Phys. Rev. B* **104**, 115420 (2021). The content of Chapter 5 has been published in this paper.
5. Balaganchi A. Bhargava, Sanjib Kumar Das, and Ion Cosma Fulga, “[Quantum phase transitions and disorder-based filter in a Floquet system](#)”, *arXiv:2111.01655* (2021).

Acknowledgements

It is hard for me to believe that four wonderful years have gone so fast, and with this dissertation it comes to an end. Firstly, I would like to express my sincere gratitude to my supervisors Prof. Jeroen van den Brink and Dr. Ion Cosma Fulga, who gave me the opportunity to carry out research in their group. During this journey, I have enjoyed working on multiple interesting problems with them. Their help and support for attending various schools and conferences helped me develop my knowledge and skills over the years. Discussions with Cosma were always stimulating and encouraging, be it physics related or on any other topic in general. He was always kind and patient to answer my doubts at all time. Also, I would like to thank him for giving me an opportunity to be a part of Anton Akhmerov's physics discussion channel, from where I learned so many useful things related to physics and science in general.

I am grateful to our close collaborator Dr. Jorge Facio. Working with him has given me ideas and experiences on dealing with real materials in topological systems. I am also thankful to my collaborators Dr. Snehasish Nandy and Dr. Tanay Nag.

I take this opportunity to warmly thank our ITF secretary Grit Rötzer for her help with the official paper works and other bureaucratic issues. During my stay at IFW, I could ask her for any help at anytime which made my stay smooth. I also want to mention Ulrike Nitzsche for the technical assistance with ITF clusters.

Now, it is time to thank my wonderful colleagues. First, I wish to thank my other group members Selma Franca, Hui Liu, Balaganchi A. Bhargava, Raghav Chaturvedi, Gabriele Naselli, Dr. Viktor Könye and Dr. Ali G. Moghaddam. Specifically, I would like to thank Selma for helping me on many occasions. I also want to thank my former and contemporary

ITF colleagues Dr. Cliò Efthimia Agrapidis, Dr. Ziba Zangeneh, Dr. Alexander Lau, Dr. Andrei Pavlov, Dennis Wawrzik, Marius Scholten, Mohamed Sabry Eldeeb. Sadly, I am going to miss the lunch time stories with Dr. Flavio Nogueira and others, and coffee time discussions with Dr. Rajyavardhan Ray. I will also be deprived of the cool discussions with Dennis Wawrzik on physics or on algorithms.

During my time in Dresden, I was fortunate enough to have friends like Ravi, Konstantinos, Ankush, Sanket, Nirdosh, with whom I have had lots of fun, and wonderful experiences. I would also like to mention my other close friends Anuj, Martik, Mushir, Anirudh, Prithwish, Pritam, Pratik, Vishnu, Maruthi, Shrinit, Gaurav, Vikash, who always supported me.

And finally, my deepest gratitude goes to my family. Their selfless love, support and sacrifice have made this journey possible for me. They have always put faith in whatever I aspire to achieve. So, thanks for everything!

Bibliography

- [1] K. v. Klitzing, G. Dorda, and M. Pepper. New method for high-accuracy determination of the fine-structure constant based on quantized hall resistance. *Phys. Rev. Lett.*, 45:494–497, Aug 1980.
- [2] Joel E. Moore. The birth of topological insulators. *Nature*, 464(7286):194–198, March 2010.
- [3] D. J. Thouless, M. Kohmoto, M. P. Nightingale, and M. den Nijs. Quantized hall conductance in a two-dimensional periodic potential. *Phys. Rev. Lett.*, 49:405–408, Aug 1982.
- [4] F. D. M. Haldane. Model for a quantum hall effect without landau levels: Condensed-matter realization of the "parity anomaly". *Phys. Rev. Lett.*, 61:2015–2018, Oct 1988.
- [5] M. Z. Hasan and C. L. Kane. Colloquium: Topological insulators. *Rev. Mod. Phys.*, 82:3045–3067, Nov 2010.
- [6] Xiao-Liang Qi and Shou-Cheng Zhang. Topological insulators and superconductors. *Rev. Mod. Phys.*, 83:1057–1110, Oct 2011.
- [7] Dmytro Pesin and Allan H. MacDonald. Spintronics and pseudospintronics in graphene and topological insulators. *Nature Materials*, 11(5):409–416, April 2012.
- [8] Takehito Yokoyama and Shuichi Murakami. Spintronics and spincaloritronics in topological insulators. *Physica E: Low-dimensional Systems and Nanostructures*, 55:1–8, 2014. Topological Objects.
- [9] Michael Freedman, Alexei Kitaev, Michael Larsen, and Zhenghan Wang. Topological quantum computation. *Bulletin of the American Mathematical Society*, 40(1):31–38, October 2002.
- [10] TQC topological quantum computation. http://reprints.gravitywaves.com/QuantumComputing/Sarma-2006_TopologicalQuantumComputation_UCSB-Q.pdf. Accessed: 2021-07-27.

- [11] Sankar Das Sarma, Michael Freedman, and Chetan Nayak. Majorana zero modes and topological quantum computation. *npj Quantum Information*, 1(1), October 2015.
- [12] Alexander Altland and Martin R. Zirnbauer. Nonstandard symmetry classes in mesoscopic normal-superconducting hybrid structures. *Phys. Rev. B*, 55:1142–1161, Jan 1997.
- [13] Alexei Kitaev, Vladimir Lebedev, and Mikhail Feigel'man. Periodic table for topological insulators and superconductors. In *AIP Conference Proceedings*. AIP, 2009.
- [14] Andreas P. Schnyder, Shinsei Ryu, Akira Furusaki, and Andreas W. W. Ludwig. Classification of topological insulators and superconductors in three spatial dimensions. *Phys. Rev. B*, 78:195125, Nov 2008.
- [15] Shinsei Ryu, Andreas P Schnyder, Akira Furusaki, and Andreas W W Ludwig. Topological insulators and superconductors: ten-fold way and dimensional hierarchy. *New Journal of Physics*, 12(6):065010, June 2010.
- [16] Ching-Kai Chiu, Jeffrey C. Y. Teo, Andreas P. Schnyder, and Shinsei Ryu. Classification of topological quantum matter with symmetries. *Rev. Mod. Phys.*, 88:035005, Aug 2016.
- [17] Felix Bloch. Über die quantenmechanik der elektronen in kristallgittern. *Zeitschrift für Physik*, 52(7-8):555–600, July 1929.
- [18] N. W. Ashcroft and N. D. Mermin. *Solid State Physics*. Holt-Saunders, 1976.
- [19] Quantal phase factors accompanying adiabatic changes. *Proceedings of the Royal Society of London. A. Mathematical and Physical Sciences*, 392(1802):45–57, March 1984.
- [20] Di Xiao, Ming-Che Chang, and Qian Niu. Berry phase effects on electronic properties. *Rev. Mod. Phys.*, 82:1959–2007, Jul 2010.
- [21] Alba Cazorla. Quantum hall effect — Wikipedia, the free encyclopedia, 2010. [Online; accessed 27-July-2021].
- [22] C.-Z. Chang, J. Zhang, X. Feng, J. Shen, Z. Zhang, M. Guo, K. Li, Y. Ou, P. Wei, L.-L. Wang, Z.-Q. Ji, Y. Feng, S. Ji, X. Chen, J. Jia, X. Dai, Z. Fang, S.-C. Zhang, K. He, Y. Wang, L. Lu, X.-C. Ma, and Q.-K. Xue. Experimental observation of the quantum anomalous hall effect in a magnetic topological insulator. *Science*, 340(6129):167–170, March 2013.
- [23] C. L. Kane and E. J. Mele. Quantum spin hall effect in graphene. *Phys. Rev. Lett.*, 95:226801, Nov 2005.

- [24] C. L. Kane and E. J. Mele. Z_2 topological order and the quantum spin hall effect. *Phys. Rev. Lett.*, 95:146802, Sep 2005.
- [25] B. A. Bernevig, T. L. Hughes, and S.-C. Zhang. Quantum spin hall effect and topological phase transition in HgTe quantum wells. *Science*, 314(5806):1757–1761, December 2006.
- [26] M. Konig, S. Wiedmann, C. Brune, A. Roth, H. Buhmann, L. W. Molenkamp, X.-L. Qi, and S.-C. Zhang. Quantum spin hall insulator state in HgTe quantum wells. *Science*, 318(5851):766–770, November 2007.
- [27] Markus König, Hartmut Buhmann, Laurens W. Molenkamp, Taylor Hughes, Chao-Xing Liu, Xiao-Liang Qi, and Shou-Cheng Zhang. The quantum spin hall effect: Theory and experiment. *Journal of the Physical Society of Japan*, 77(3):031007, March 2008.
- [28] Yong Xu, Binghai Yan, Hai-Jun Zhang, Jing Wang, Gang Xu, Peizhe Tang, Wenhui Duan, and Shou-Cheng Zhang. Large-gap quantum spin hall insulators in tin films. *Phys. Rev. Lett.*, 111:136804, Sep 2013.
- [29] Jin-Jian Zhou, Wanxiang Feng, Cheng-Cheng Liu, Shan Guan, and Yugui Yao. Large-gap quantum spin hall insulator in single layer bismuth monobromide bi_4br_4 . *Nano Letters*, 14(8):4767–4771, July 2014.
- [30] X. Qian, J. Liu, L. Fu, and J. Li. Quantum spin hall effect in two-dimensional transition metal dichalcogenides. *Science*, 346(6215):1344–1347, November 2014.
- [31] Yong Xu, Peizhe Tang, and Shou-Cheng Zhang. Large-gap quantum spin hall states in decorated stanene grown on a substrate. *Phys. Rev. B*, 92:081112, Aug 2015.
- [32] Sanfeng Wu, Valla Fatemi, Quinn D. Gibson, Kenji Watanabe, Takashi Taniguchi, Robert J. Cava, and Pablo Jarillo-Herrero. Observation of the quantum spin hall effect up to 100 kelvin in a monolayer crystal. *Science*, 359(6371):76–79, January 2018.
- [33] P. Chen, Woei Wu Pai, Y.-H. Chan, W.-L. Sun, C.-Z. Xu, D.-S. Lin, M. Y. Chou, A.-V. Fedorov, and T.-C. Chiang. Large quantum-spin-hall gap in single-layer 1t' WSe2. *Nature Communications*, 9(1), May 2018.
- [34] Antimo Marrazzo, Marco Gibertini, Davide Campi, Nicolas Mounet, and Nicola Marzari. Prediction of a large-gap and switchable kane-mele quantum spin hall insulator. *Phys. Rev. Lett.*, 120:117701, Mar 2018.

- [35] Liang Fu and C. L. Kane. Time reversal polarization and a Z_2 adiabatic spin pump. *Phys. Rev. B*, 74:195312, Nov 2006.
- [36] Liang Fu and C. L. Kane. Topological insulators with inversion symmetry. *Phys. Rev. B*, 76:045302, Jul 2007.
- [37] Liang Fu, C. L. Kane, and E. J. Mele. Topological insulators in three dimensions. *Phys. Rev. Lett.*, 98:106803, Mar 2007.
- [38] Ching-Kai Chiu, Hong Yao, and Shinsei Ryu. Classification of topological insulators and superconductors in the presence of reflection symmetry. *Phys. Rev. B*, 88:075142, Aug 2013.
- [39] Ken Shiozaki and Masatoshi Sato. Topology of crystalline insulators and superconductors. *Phys. Rev. B*, 90:165114, Oct 2014.
- [40] Liang Fu. Topological crystalline insulators. *Phys. Rev. Lett.*, 106:106802, Mar 2011.
- [41] Yoichi Ando and Liang Fu. Topological crystalline insulators and topological superconductors: From concepts to materials. *Annual Review of Condensed Matter Physics*, 6(1):361–381, March 2015.
- [42] Timothy H. Hsieh, Hsin Lin, Junwei Liu, Wenhui Duan, Arun Bansil, and Liang Fu. Topological crystalline insulators in the SnTe material class. *Nature Communications*, 3(1), January 2012.
- [43] Y. Tanaka, Zhi Ren, T. Sato, K. Nakayama, S. Souma, T. Takahashi, Kouji Segawa, and Yoichi Ando. Experimental realization of a topological crystalline insulator in SnTe. *Nature Physics*, 8(11):800–803, September 2012.
- [44] Titus Neupert and Frank Schindler. Topological crystalline insulators. In *Topological Matter*, pages 31–61. Springer International Publishing, 2018.
- [45] P. Dziawa, B. J. Kowalski, K. Dybko, R. Buczko, A. Szczerbakow, M. Szot, E. Łusakowska, T. Balasubramanian, B. M. Wojek, M. H. Berntsen, O. Tjernberg, and T. Story. Topological crystalline insulator states in pb_{1-x}Sn_xSe. *Nature Materials*, 11(12):1023–1027, September 2012.
- [46] Su-Yang Xu, Chang Liu, N. Alidoust, M. Neupane, D. Qian, I. Bełopolski, J.D. Denlinger, Y.J. Wang, H. Lin, L.A. Wray, G. Landolt, B. Slomski, J.H. Dil, A. Marcinkova, E. Morosan, Q. Gibson, R. Sankar, F.C. Chou, R.J. Cava, A. Bansil, and M.Z. Hasan. Observation of a topological crystalline insulator phase and topological phase transition in pb_{1-x}Sn_xTe. *Nature Communications*, 3(1), January 2012.

- [47] Zhijun Wang, A. Alexandradinata, R. J. Cava, and B. Andrei Bernevig. Hourglass fermions. *Nature*, 532(7598):189–194, April 2016.
- [48] Xiaoting Zhou, Chuang-Han Hsu, Tay-Rong Chang, Hung-Ju Tien, Qiong Ma, Pablo Jarillo-Herrero, Nuh Gedik, Arun Bansil, Vitor M. Pereira, Su-Yang Xu, Hsin Lin, and Liang Fu. Topological crystalline insulator states in the ca_2As family. *Phys. Rev. B*, 98:241104, Dec 2018.
- [49] Hoi Chun Po, Ashvin Vishwanath, and Haruki Watanabe. Symmetry-based indicators of band topology in the 230 space groups. *Nature Communications*, 8(1), June 2017.
- [50] Barry Bradlyn, L. Elcoro, Jennifer Cano, M. G. Vergniory, Zhijun Wang, C. Felser, M. I. Aroyo, and B. Andrei Bernevig. Topological quantum chemistry. *Nature*, 547(7663):298–305, July 2017.
- [51] Haruki Watanabe, Hoi Chun Po, and Ashvin Vishwanath. Structure and topology of band structures in the 1651 magnetic space groups. *Science Advances*, 4(8):eaat8685, August 2018.
- [52] Youngkuk Kim, C. L. Kane, E. J. Mele, and Andrew M. Rappe. Layered topological crystalline insulators. *Phys. Rev. Lett.*, 115:086802, Aug 2015.
- [53] I. C. Fulga, N. Avraham, H. Beidenkopf, and A. Stern. Coupled-layer description of topological crystalline insulators. *Phys. Rev. B*, 94:125405, Sep 2016.
- [54] Alexei Kitaev. Periodic table for topological insulators and superconductors. *AIP Conference Proceedings*, 1134(1):22–30, 2009.
- [55] Robert-Jan Slager, Andrej Mesaros, Vladimir Juricic, and Jan Zaanen. The space group classification of topological band-insulators. *Nat. Phys.*, 9:98, Dec 2012.
- [56] Takahiro Morimoto and Akira Furusaki. Topological classification with additional symmetries from clifford algebras. *Phys. Rev. B*, 88:125129, Sep 2013.
- [57] Priyamvada Jadaun, Di Xiao, Qian Niu, and Sanjay K. Banerjee. Topological classification of crystalline insulators with space group symmetry. *Phys. Rev. B*, 88:085110, Aug 2013.
- [58] Wladimir A. Benalcazar, Jeffrey C. Y. Teo, and Taylor L. Hughes. Classification of two-dimensional topological crystalline superconductors and majorana bound states at disclinations. *Phys. Rev. B*, 89:224503, Jun 2014.

- [59] Chen Fang and Liang Fu. New classes of three-dimensional topological crystalline insulators: Nonsymmorphic and magnetic. *Phys. Rev. B*, 91:161105, Apr 2015.
- [60] M Diez, D I Pikulin, I C Fulga, and J Tworzydo. Extended topological group structure due to average reflection symmetry. *New J. Phys.*, 17(4):043014, 2015.
- [61] Mehdi Kargarian and Gregory A. Fiete. Topological crystalline insulators in transition metal oxides. *Phys. Rev. Lett.*, 110:156403, Apr 2013.
- [62] Ernesto O. Wrasse and Tome M. Schmidt. Prediction of two-dimensional topological crystalline insulator in pbse monolayer. *Nano Lett.*, 14(10):5717–5720, 2014.
- [63] Takahiro Morimoto, Akira Furusaki, and Christopher Mudry. Anderson localization and the topology of classifying spaces. *Phys. Rev. B*, 91:235111, Jun 2015.
- [64] Luka Trifunovic, Daniel Loss, and Jelena Klinovaja. From coupled rashba electron- and hole-gas layers to three-dimensional topological insulators. *Phys. Rev. B*, 93(20):205406, may 2016.
- [65] Yanick Volpez, Daniel Loss, and Jelena Klinovaja. Three-dimensional fractional topological insulators in coupled rashba layers. *Phys. Rev. B*, 96(8):085422, aug 2017.
- [66] Roger S. K. Mong, Andrew M. Essin, and Joel E. Moore. Antiferromagnetic topological insulators. *Phys. Rev. B*, 81:245209, Jun 2010.
- [67] Heejae Kim and Shuichi Murakami. Emergent spinless weyl semimetals between the topological crystalline insulator and normal insulator phases with glide symmetry. *Phys. Rev. B*, 93:195138, May 2016.
- [68] Fuyan Lu, Bowen Shi, and Yuan-Ming Lu. Classification and surface anomaly of glide symmetry protected topological phases in three dimensions. *New J. Phys.*, 19(7):073002, 2017.
- [69] K. Ladovrechis and I. Cosma Fulga. Anomalous Floquet topological crystalline insulators. *arXiv:1806.10099*, June 2018.
- [70] Frank Schindler, Ashley M. Cook, Maia G. Vergniory, Zhijun Wang, Stuart S. P. Parkin, B. Andrei Bernevig, and Titus Neupert. Higher-order topological insulators. *Sci. Adv.*, 4(6):eaat0346, jun 2018.
- [71] Luka Trifunovic and Piet W. Brouwer. Higher-order bulk-boundary correspondence for topological crystalline phases. *Phys. Rev. X*, 9:011012, Jan 2019.

- [72] Eslam Khalaf. Higher-order topological insulators and superconductors protected by inversion symmetry. *Phys. Rev. B*, 97:205136, May 2018.
- [73] S. H. Kooi, G. van Miert, and C. Ortix. Inversion-symmetry protected chiral hinge states in stacks of doped quantum Hall layers. *arXiv:1807.01277*, July 2018.
- [74] Yuanbo Zhang, Yan-Wen Tan, Horst L. Stormer, and Philip Kim. Experimental observation of the quantum hall effect and berry's phase in graphene. *Nature*, 438:201, Nov 2005.
- [75] C. L. Kane and E. J. Mele. Quantum spin hall effect in graphene. *Phys. Rev. Lett.*, 95:226801, Nov 2005.
- [76] Christoph W Groth, Michael Wimmer, Anton R Akhmerov, and Xavier Waintal. Kwant: a software package for quantum transport. *New J. Phys.*, 16(6):063065, 2014.
- [77] *In the Supplemental Material we include the code used to generate all of our numerical results.*
- [78] Hongki Min, J. E. Hill, N. A. Sinitsyn, B. R. Sahu, Leonard Kleinman, and A. H. MacDonald. Intrinsic and rashba spin-orbit interactions in graphene sheets. *Phys. Rev. B*, 74:165310, Oct 2006.
- [79] Yugui Yao, Fei Ye, Xiao-Liang Qi, Shou-Cheng Zhang, and Zhong Fang. Spin-orbit gap of graphene: First-principles calculations. *Phys. Rev. B*, 75:041401, Jan 2007.
- [80] A. Avsar, J. Y. Tan, T. Taychatanapat, J. Balakrishnan, G. K. W. Koon, Y. Yeo, J. Lahiri, A. Carvalho, A. S. Rodin, E. C. T. O'Farrell, G. Eda, A. H. Castro Neto, and B. Özyilmaz. Spin-orbit proximity effect in graphene. *Nat. Commun.*, 5:4875, Sep 2014.
- [81] L. Kou, F. Hu, B. Yan, T. Wehling, C. Felser, T. Frauenheim, and C. Chen. Proximity enhanced quantum spin hall state in graphene. *Carbon*, 87:418, jun 2015.
- [82] Liangzhi Kou, Shu-Chun Wu, Claudia Felser, Thomas Frauenheim, Changfeng Chen, and Binghai Yan. Robust 2d topological insulators in van der waals heterostructures. *ACS Nano*, 8(10):10448–10454, 2014.
- [83] Junwei Liu, Timothy H. Hsieh, Peng Wei, Wenhui Duan, Jagadeesh Moodera, and Liang Fu. Spin-filtered edge states with an electrically tunable gap in a two-dimensional topological crystalline insulator. *Nat. Mater.*, 13(2):178, dec 2013.

- [84] Fernando Dominguez, Benedikt Scharf, Gang Li, Jg Scher, Ralph Claessen, Werner Hanke, Ronny Thomale, and Ewelina M. Hankiewicz. Testing topological protection of edge states in hexagonal quantum spin hall candidate materials. *Phys. Rev. B*, 98(16):161407, oct 2018.
- [85] A. V. Bune, V. M. Fridkin, Stephen Ducharme, L. M. Blinov, S. P. Palto, A. V. Sorokin, S. G. Yudin, and A. Zlatkin. Two-dimensional ferroelectric films. *Nature*, 391(6670):874, feb 1998.
- [86] B. Chu, Xin Zhou, Kailiang Ren, Bret Neese, Minren Lin, Qing Wang, F. Bauer, and Q. M. Zhang. A dielectric polymer with high electric energy density and fast discharge speed. *Science*, 313(5785):334, jul 2006.
- [87] A. K. Geim and I. V. Grigorieva. Van der waals heterostructures. *Nature*, 499(7459):419, jul 2013.
- [88] K. S. Novoselov, A. Mishchenko, A. Carvalho, and A. H. Castro Neto. 2d materials and van der waals heterostructures. *Science*, 353(6298):aac9439, jul 2016.
- [89] Yuan Liu, Nathan O. Weiss, Xidong Duan, Hung-Chieh Cheng, Yu Huang, and Xiangfeng Duan. Van der waals heterostructures and devices. *Nat. Rev. Mater.*, 1(9):16042, jul 2016.
- [90] Zohar Ringel, Yaakov E. Kraus, and Ady Stern. Strong side of weak topological insulators. *Phys. Rev. B*, 86(4):045102, jul 2012.
- [91] J. E. Moore and L. Balents. Topological invariants of time-reversal-invariant band structures. *Phys. Rev. B*, 75:121306, Mar 2007.
- [92] Rahul Roy. Topological phases and the quantum spin hall effect in three dimensions. *Phys. Rev. B*, 79:195322, May 2009.
- [93] Timothy H Hsieh, Hsin Lin, Junwei Liu, Wenhui Duan, Arun Bansil, and Liang Fu. Topological crystalline insulators in the SnTe material class. *Nature Communications*, 3:982, 2012.
- [94] Xiangang Wan, Ari M. Turner, Ashvin Vishwanath, and Sergey Y. Savrasov. Topological semimetal and Fermi-arc surface states in the electronic structure of pyrochlore iridates. *Phys. Rev. B*, 83:205101, May 2011.
- [95] Su-Yang Xu, Ilya Belopolski, Nasser Alidoust, Madhab Neupane, Guang Bian, Chenglong Zhang, Raman Sankar, Guoqing Chang, Zhujun Yuan, Chi-Cheng Lee, et al. Discovery of a Weyl fermion semimetal and topological Fermi arcs. *Science*, 349(6248):613–617, 2015.

- [96] BQ Lv, HM Weng, BB Fu, XP Wang, Hu Miao, Junzhang Ma, P Richard, XC Huang, LX Zhao, GF Chen, et al. Experimental discovery of Weyl semimetal TaAs. *Physical Review X*, 5(3):031013, 2015.
- [97] Alexey A Soluyanov, Dominik Gresch, Zhijun Wang, QuanSheng Wu, Matthias Troyer, Xi Dai, and B Andrei Bernevig. Type-II Weyl semimetals. *Nature*, 527(7579):495, 2015.
- [98] Wladimir A. Benalcazar, B. Andrei Bernevig, and Taylor L. Hughes. Quantized electric multipole insulators. *Science*, 357(6346):61, jul 2017.
- [99] Wladimir A. Benalcazar, B. Andrei Bernevig, and Taylor L. Hughes. Electric multipole moments, topological multipole moment pumping, and chiral hinge states in crystalline insulators. *Phys. Rev. B*, 96(24):245115, dec 2017.
- [100] Josias Langbehn, Yang Peng, Luka Trifunovic, Felix von Oppen, and Piet W. Brouwer. Reflection-symmetric second-order topological insulators and superconductors. *Phys. Rev. Lett.*, 119(24):246401, dec 2017.
- [101] Shin Hayashi. Topological invariants and corner states for hamiltonians on a three-dimensional lattice. *Commun. Math. Phys.*, 364(1):343, aug 2018.
- [102] Zhida Song, Zhong Fang, and Chen Fang. (d-2) -dimensional edge states of rotation symmetry protected topological states. *Phys. Rev. Lett.*, 119(24):246402, dec 2017.
- [103] Frank Schindler, Ashley M. Cook, Maia G. Vergniory, Zhijun Wang, Stuart S. P. Parkin, B. Andrei Bernevig, and Titus Neupert. Higher-order topological insulators. *Science Advances*, 4(6), 2018.
- [104] Frank Schindler, Zhijun Wang, Maia G Vergniory, Ashley M Cook, Anil Murani, Shamashis Sengupta, Alik Yu Kasumov, Richard Deblock, Sangjun Jeon, Ilya Drozdov, et al. Higher-order topology in Bismuth. *Nature Physics*, 14(9):918, 2018.
- [105] Yuxuan Wang, Mao Lin, and Taylor L. Hughes. Weak-pairing higher order topological superconductors. *Phys. Rev. B*, 98:165144, Oct 2018.
- [106] Motohiko Ezawa. Higher-order topological insulators and semimetals on the breathing Kagome and pyrochlore lattices. *Phys. Rev. Lett.*, 120(2):026801, jan 2018.
- [107] Motohiko Ezawa. Magnetic second-order topological insulators and semimetals. *Phys. Rev. B*, 97(15):155305, apr 2018.

- [108] Motohiko Ezawa. Strong and weak second-order topological insulators with hexagonal symmetry and \mathbb{Z}_3 index. *Phys. Rev. B*, 97:241402(R), Jun 2018.
- [109] Vatsal Dwivedi, Ciarán Hickey, Tim Eschmann, and Simon Trebst. Majorana corner modes in a second-order Kitaev spin liquid. *Phys. Rev. B*, 98(5):054432, aug 2018.
- [110] Guido van Miert and Carmine Ortix. Higher-order topological insulators protected by inversion and rotoinversion symmetries. *Phys. Rev. B*, 98:081110, Aug 2018.
- [111] Motohiko Ezawa. Minimal models for Wannier-type higher-order topological insulators and phosphorene. *Phys. Rev. B*, 98(4):045125, jul 2018.
- [112] Chen-Hsuan Hsu, Peter Stano, Jelena Klinovaja, and Daniel Loss. Majorana kramers pairs in higher-order topological insulators. *Phys. Rev. Lett.*, 121:196801, Nov 2018.
- [113] Zhongbo Yan, Fei Song, and Zhong Wang. Majorana corner modes in a high-temperature platform. *Phys. Rev. Lett.*, 121:096803, Aug 2018.
- [114] Qiyue Wang, Cheng-Cheng Liu, Yuan-Ming Lu, and Fan Zhang. High-temperature majorana corner states. *Phys. Rev. Lett.*, 121:186801, Oct 2018.
- [115] Max Geier, Luka Trifunovic, Max Hoskam, and Piet W. Brouwer. Second-order topological insulators and superconductors with an order-two crystalline symmetry. *Phys. Rev. B*, 97(20):205135, may 2018.
- [116] Tao Liu, James Jun He, and Franco Nori. Majorana corner states in a two-dimensional magnetic topological insulator on a high-temperature superconductor. *Phys. Rev. B*, 98:245413, Dec 2018.
- [117] Marc Serra-Garcia, Roman Süsstrunk, and Sebastian D. Huber. Observation of quadrupole transitions and edge mode topology in an LC circuit network. *Phys. Rev. B*, 99:020304, Jan 2019.
- [118] Marc Serra-Garcia, Valerio Peri, Roman Süsstrunk, Osama R. Bilal, Tom Larsen, Luis Guillermo Villanueva, and Sebastian D. Huber. Observation of a phononic quadrupole topological insulator. *Nature*, 555(7696):342–345, jan 2018.
- [119] Christopher W. Peterson, Wladimir A. Benalcazar, Taylor L. Hughes, and Gaurav Bahl. A quantized microwave quadrupole insulator with topologically protected corner states. *Nature*, 555(7696):346–350, mar 2018.

- [120] Xiujuan Zhang, Hai-Xiao Wang, Zhi-Kang Lin, Yuan Tian, Biye Xie, Ming-Hui Lu, Yan-Feng Chen, and Jian-Hua Jiang. Observation of second-order topological insulators in sonic crystals. *arXiv*:, 1806.10028, 2018.
- [121] Stefan Imhof, Christian Berger, Florian Bayer, Johannes Brehm, Laurens W. Molenkamp, Tobias Kiessling, Frank Schindler, Ching Hua Lee, Martin Greiter, Titus Neupert, and Ronny Thomale. Topoelectrical-circuit realization of topological corner modes. *Nature Phys.*, 14(9):925, sep 2018.
- [122] Anna Vymazalová, František Laufek, Milan Drábek, Alexandre Raphael Cabral, Jakub Haloda, Tamara Sidorinová, Bernd Lehmann, Henry Francisco Galbiatti, and Jan Drahokoupil. Jacutingaite, Pt_2HgSe_3 , a new platinum-group mineral species from the Cauê iron-ore deposit, Itabira district, Minas Gerais, Brazil. *The Canadian Mineralogist*, 50(2):431–440, 2012.
- [123] Antimo Marrazzo, Marco Gibertini, Davide Campi, Nicolas Mounet, and Nicola Marzari. Prediction of a large-gap and switchable Kane-Mele quantum spin Hall insulator. *Phys. Rev. Lett.*, 120:117701, Mar 2018.
- [124] K. Kandari, G. Kukucska, Vancsó P., J. Koltai, G. Baranka, Z.E. Horvóth, Hoffmann, A.A. Vymazalová, L. Tapasztó, and P. Nemes-Incze. Evidence for room temperature quantum spin Hall state in the layered mineral Jacutingaite. *arXiv preprint arXiv:1903.02458*, 2019.
- [125] Xianxin Wu, Mario Fink, Werner Hanke, Ronny Thomale, and Domenico Di Sante. Unconventional superconductivity in a doped quantum spin hall insulator. *arXiv preprint arXiv:1811.01746*, 2018.
- [126] IP Rusinov, TV Menshchikova, A Isaeva, SV Eremeev, Yu M Koroteev, MG Vergniory, PM Echenique, and Evgueni V Chulkov. Mirror-symmetry protected non-TRIM surface state in the weak topological insulator Bi_2TeI . *Scientific reports*, 6:20734, 2016.
- [127] Nurit Avraham, Andrew Norris, Yan Sun, Yanpeng Qi, Lin Pan, Anna Isaeva, Alexander Zeugner, Claudia Felser, Binghai Yan, and Haim Beidenkopf. Coexisting surface states in the weak and crystalline topological insulator Bi_2TeI . *arXiv preprint arXiv:1708.09062*, 2017.
- [128] Alexander Zeugner, Johannes Teichert, Martin Kaiser, Tatiana V Menshchikova, Igor P Rusinov, Anton V Markelov, Evgueni V Chulkov, Thomas Doert, Michael Ruck, and Anna Isaeva. Synthesis, crystal and topological electronic structures of new bismuth tellurohalides Bi_2TeBr and Bi_3TeBr . *Chemistry of Materials*, 30(15):5272–5284, 2018.

- [129] Markus Eschbach, Martin Lanius, Chengwang Niu, Ewa Młyńczak, Pika Gospodarič, Jens Kellner, Peter Schüffelgen, Mathias Gehlmann, Sven Döring, Elmar Neumann, et al. *Bi₁Te₁* is a dual topological insulator. *Nature Communications*, 8:14976, 2017.
- [130] F Laufek, A Vymazalová, and M Drábek. Powder diffraction study of Pd₂HgSe₃. *Powder Diffraction*, 32(4):244–248, 2017.
- [131] Klaus Koepernik and Helmut Eschrig. Full-potential nonorthogonal local-orbital minimum-basis band-structure scheme. *Physical Review B*, 59(3):1743, 1999.
- [132] Liang Fu, C. L. Kane, and E. J. Mele. Topological insulators in three dimensions. *Phys. Rev. Lett.*, 98:106803, Mar 2007.
- [133] Binghai Yan, Lukas Mückler, and Claudia Felser. Prediction of weak topological insulators in layered semiconductors. *Phys. Rev. Lett.*, 109:116406, Sep 2012.
- [134] Kunjalata Majhi, Koushik Pal, Himanshu Lohani, Abhishek Banerjee, Pramita Mishra, Anil K Yadav, R Ganesan, BR Sekhar, Umesh V Waghmare, and PS Anil Kumar. Emergence of a weak topological insulator from the Bi_xSe_y family. *Applied Physics Letters*, 110(16):162102, 2017.
- [135] Bertold Rasche, Anna Isaeva, Michael Ruck, Sergey Borisenko, Volodymyr Zabolotnyy, Bernd Büchner, Klaus Koepernik, Carmine Ortix, Manuel Richter, and Jeroen Van Den Brink. Stacked topological insulator built from bismuth-based graphene sheet analogues. *Nature Materials*, 12(5):422, 2013.
- [136] F. Reis, G. Li, L. Dudy, M. Bauernfeind, S. Glass, W. Hanke, R. Thomale, J. Schäfer, and R. Claessen. Bismuthene on a SiC substrate: A candidate for a high-temperature quantum spin hall material. *Science*, 357(6348):287–290, jun 2017.
- [137] G. Kresse and D. Joubert. From ultrasoft pseudopotentials to the projector augmented-wave method. *Phys. Rev. B*, 59:1758–1775, Jan 1999.
- [138] Jürgen Hafner. Ab-initio simulations of materials using VASP: Density-functional theory and beyond. *Journal of Computational Chemistry*, 29(13):2044–2078, 2008.
- [139] Jeffrey CY Teo, Liang Fu, and CL Kane. Surface states and topological invariants in three-dimensional topological insulators: Application to Bi_{1-x}Sb_x. *Physical Review B*, 78(4):045426, 2008.
- [140] Barry Bradlyn, L Elcoro, Jennifer Cano, MG Vergniory, Zhijun Wang, C Felser, MI Aroyo, and B Andrei Bernevig. Topological quantum chemistry. *Nature*, 547(7663):298, 2017.

- [141] MG Vergniory, L Elcoro, Claudia Felser, Nicolas Regnault, B Andrei Bernevig, and Zhijun Wang. A complete catalogue of high-quality topological materials. *Nature*, 566(7745):480, 2019.
- [142] Zhijun Wang, Benjamin J Wieder, Jian Li, Binghai Yan, and B Andrei Bernevig. Higher-order topology, monopole nodal lines, and the origin of large Fermi arcs in transition metal dichalcogenides XTe_2 ($X = Mo, W$). *arXiv preprint arXiv:1806.11116*, 2018.
- [143] Raquel Queiroz, Ion Cosma Fulga, Nurit Avraham, Haim Beidenkopf, and Jennifer Cano. Partial lattice defects in higher order topological insulators. *arXiv preprint arXiv:1809.03518*, 2018.
- [144] Yuval Baum, Thore Posske, Ion Cosma Fulga, Björn Trauzettel, and Ady Stern. Coexisting edge states and gapless bulk in topological states of matter. *Phys. Rev. Lett.*, 114(13):136801, mar 2015.
- [145] Yuval Baum, Thore Posske, Ion Cosma Fulga, Björn Trauzettel, and Ady Stern. Gapless topological superconductors: Model hamiltonian and realization. *Phys. Rev. B*, 92(4):045128, jul 2015.
- [146] Wladimir A. Benalcazar, B. Andrei Bernevig, and Taylor L. Hughes. Quantized electric multipole insulators. *Science*, 357(6346):61–66, July 2017.
- [147] Wladimir A. Benalcazar, B. Andrei Bernevig, and Taylor L. Hughes. Electric multipole moments, topological multipole moment pumping, and chiral hinge states in crystalline insulators. *Phys. Rev. B*, 96:245115, Dec 2017.
- [148] Mao Lin and Taylor L. Hughes. Topological quadrupolar semimetals. *Phys. Rev. B*, 98:241103, Dec 2018.
- [149] Zhida Song, Zhong Fang, and Chen Fang. $(d - 2)$ -dimensional edge states of rotation symmetry protected topological states. *Phys. Rev. Lett.*, 119:246402, Dec 2017.
- [150] Josias Langbehn, Yang Peng, Luka Trifunovic, Felix von Oppen, and Piet W. Brouwer. Reflection-symmetric second-order topological insulators and superconductors. *Phys. Rev. Lett.*, 119:246401, Dec 2017.
- [151] Frank Schindler, Ashley M. Cook, Maia G. Vergniory, Zhijun Wang, Stuart S. P. Parkin, B. Andrei Bernevig, and Titus Neupert. Higher-order topological insulators. *Sci. Adv.*, 4(6):eaat0346, June 2018.
- [152] Motohiko Ezawa. Higher-order topological insulators and semimetals on the breathing kagome and pyrochlore lattices. *Phys. Rev. Lett.*, 120:026801, Jan 2018.

- [153] Shin Hayashi. Topological invariants and corner states for hamiltonians on a three-dimensional lattice. *Communications in Mathematical Physics*, 364(1):343–356, August 2018.
- [154] Abhay Kumar Nayak, Jonathan Reiner, Raquel Queiroz, Huixia Fu, Chandra Shekhar, Binghai Yan, Claudia Felser, Nurit Avraham, and Haim Beidenkopf. Resolving the topological classification of bismuth with topological defects. *Sci. Adv.*, 5(11):eaax6996, November 2019.
- [155] Dániel Varjas, Alexander Lau, Kim Pöyhönen, Anton R. Akhmerov, Dmitry I. Pikulin, and Ion Cosma Fulga. Topological phases without crystalline counterparts. *Phys. Rev. Lett.*, 123:196401, Nov 2019.
- [156] Raquel Queiroz, Ion Cosma Fulga, Nurit Avraham, Haim Beidenkopf, and Jennifer Cano. Partial lattice defects in higher-order topological insulators. *Phys. Rev. Lett.*, 123:266802, Dec 2019.
- [157] Max Geier, Ion Cosma Fulga, and Alexander Lau. Bulk-boundary-defect correspondence at disclinations in rotation-symmetric topological insulators and superconductors. *SciPost Physics*, 10(4), April 2021.
- [158] Sophia Simon, Max Geier, and Piet W. Brouwer. Higher-order topological semimetals and nodal superconductors with an order-two crystalline symmetry, arXiv:2109.02664, 2021.
- [159] S. Franca, J. van den Brink, and I. C. Fulga. An anomalous higher-order topological insulator. *Phys. Rev. B*, 98:201114, Nov 2018.
- [160] Hui Liu, Selma Franca, Ali G. Moghaddam, Fabian Hassler, and Ion Cosma Fulga. Network model for higher-order topological phases. *Phys. Rev. B*, 103:115428, Mar 2021.
- [161] W. B. Rui, Song-Bo Zhang, Moritz M. Hirschmann, Zhen Zheng, Andreas P. Schnyder, Björn Trauzettel, and Z. D. Wang. Higher-order weyl superconductors with anisotropic weyl-point connectivity. *Phys. Rev. B*, 103:184510, May 2021.
- [162] Y. X. Zhao, Y. Lu, and Shengyuan A. Yang. Topological second-order spin-3/2 liquids with hinge fermi arcs, arXiv:2005.14500, 2020.
- [163] Yuan Fang and Jennifer Cano. When do dirac points have higher order fermi arcs? arXiv:2109.01670, 2021.
- [164] Sayed Ali Akbar Ghorashi, Tianhe Li, and Taylor L. Hughes. Higher-order weyl semimetals. *Phys. Rev. Lett.*, 125:266804, Dec 2020.

- [165] Hai-Xiao Wang, Zhi-Kang Lin, Bin Jiang, Guang-Yu Guo, and Jian-Hua Jiang. Higher-order weyl semimetals. *Phys. Rev. Lett.*, 125:146401, Sep 2020.
- [166] Benjamin J. Wieder, Zhijun Wang, Jennifer Cano, Xi Dai, Leslie M. Schoop, Barry Bradlyn, and B. Andrei Bernevig. Strong and fragile topological dirac semimetals with higher-order fermi arcs. *Nat. Commun.*, 11(1):627, Jan 2020.
- [167] Yuan Fang and Jennifer Cano. Higher-order topological insulators in antiperovskites. *Phys. Rev. B*, 101:245110, Jun 2020.
- [168] Zhijun Wang, Benjamin J. Wieder, Jian Li, Binghai Yan, and B. Andrei Bernevig. Higher-order topology, monopole nodal lines, and the origin of large fermi arcs in transition metal dichalcogenides $x\text{Te}_2$ ($x = \text{Mo, W}$). *Phys. Rev. Lett.*, 123:186401, Oct 2019.
- [169] Yong-Bin Choi, Yingming Xie, Chui-Zhen Chen, Jinho Park, Su-Beom Song, Jiho Yoon, B. J. Kim, Takashi Taniguchi, Kenji Watanabe, Jonghwan Kim, Kin Chung Fong, Mazhar N. Ali, Kam Tuen Law, and Gil-Ho Lee. Evidence of higher-order topology in multilayer WTe₂ from josephson coupling through anisotropic hinge states. *Nature Materials*, 19(9):974–979, July 2020.
- [170] András L. Szabó, Roderich Moessner, and Bitan Roy. Strain-engineered higher-order topological phases for spin- $\frac{3}{2}$ Luttinger fermions. *Phys. Rev. B*, 101:121301, Mar 2020.
- [171] Stanislav Chadov, Xiaoliang Qi, Jürgen Kübler, Gerhard H Fecher, Claudia Felser, and Shou Cheng Zhang. Tunable multifunctional topological insulators in ternary Heusler compounds. *Nat. Mater.*, 9(7):541–545, 2010.
- [172] Hsin Lin, L Andrew Wray, Yuqi Xia, Suyang Xu, Shuang Jia, Robert J Cava, Arun Bansil, and M Zahid Hasan. Half-Heusler ternary compounds as new multifunctional experimental platforms for topological quantum phenomena. *Nat. Mater.*, 9(7):546–549, 2010.
- [173] Di Xiao, Yugui Yao, Wanxiang Feng, Jun Wen, Wenguang Zhu, Xing-Qiu Chen, G. Malcolm Stocks, and Zhenyu Zhang. Half-Heusler Compounds as a New Class of Three-Dimensional Topological Insulators. *Phys. Rev. Lett.*, 105:096404, Aug 2010.
- [174] Liang Fu and C. L. Kane. Topological insulators with inversion symmetry. *Phys. Rev. B*, 76:045302, Jul 2007.
- [175] Markus König, Steffen Wiedmann, Christoph Brüne, Andreas Roth, Hartmut Buhmann, Laurens W. Molenkamp, Xiao-Liang Qi, and Shou-Cheng Zhang. Quantum spin hall insulator state in hgte quantum wells. *Science*, 318(5851):766–770, 2007.

- [176] C. Brüne, C. X. Liu, E. G. Novik, E. M. Hankiewicz, H. Buhmann, Y. L. Chen, X. L. Qi, Z. X. Shen, S. C. Zhang, and L. W. Molenkamp. Quantum Hall Effect from the Topological Surface States of Strained Bulk HgTe. *Phys. Rev. Lett.*, 106:126803, Mar 2011.
- [177] Alexander Khaetskii, Vitaly Golovach, and Arnold Kiefer. Revisiting the physical origin and nature of surface states in inverted-band semiconductors, arXiv:2107.04704, 2021.
- [178] Tanja Graf, Claudia Felser, and Stuart SP Parkin. Simple rules for the understanding of Heusler compounds. *Prog. Solid. State Ch.*, 39(1):1–50, 2011.
- [179] W. Al-Sawai, Hsin Lin, R. S. Markiewicz, L. A. Wray, Y. Xia, S.-Y. Xu, M. Z. Hasan, and A. Bansil. Topological electronic structure in half-Heusler topological insulators. *Phys. Rev. B*, 82:125208, Sep 2010.
- [180] Julien Vidal, Xiuwen Zhang, Vladan Stevanović, Jun-Wei Luo, and Alex Zunger. Large insulating gap in topological insulators induced by negative spin-orbit splitting. *Phys. Rev. B*, 86:075316, Aug 2012.
- [181] Shi-Yuan Lin, Ming Chen, Xiao-Bao Yang, Yu-Jun Zhao, Shu-Chun Wu, Claudia Felser, and Binghai Yan. Theoretical search for half-Heusler topological insulators. *Phys. Rev. B*, 91:094107, Mar 2015.
- [182] J. A. Logan, S. J. Patel, S. D. Harrington, C. M. Polley, B. D. Schultz, T. Balasubramanian, A. Janotti, A. Mikkelsen, and C. J. Palmstrom. Observation of a topologically non-trivial surface state in half-heusler PtLuSb (001) thin films. *Nat. Commun.*, 7(1), June 2016.
- [183] ZK Liu, LX Yang, S-C Wu, Chandra Shekhar, Juan Jiang, HF Yang, Yi Zhang, S-K Mo, Zahid Hussain, Binghai Yan, et al. Observation of unusual topological surface states in half-Heusler compounds LnPtBi (Ln= Lu, Y). *Nat. Commun.*, 7(1):1–7, 2016.
- [184] Jennifer Cano, Barry Bradlyn, Zhijun Wang, Max Hirschberger, N. P. Ong, and B. A. Bernevig. Chiral anomaly factory: Creating Weyl fermions with a magnetic field. *Phys. Rev. B*, 95:161306, Apr 2017.
- [185] T Suzuki, R Chisnell, A Devarakonda, Y-T Liu, W Feng, D Xiao, Jeffrey W Lynn, and JG Checkelsky. Large anomalous Hall effect in a half-Heusler antiferromagnet. *Nat. Phys.*, 12(12):1119–1123, 2016.

- [186] Max Hirschberger, Satya Kushwaha, Zhijun Wang, Quinn Gibson, Sihang Liang, Carina A Belvin, Bogdan Andrei Bernevig, Robert Joseph Cava, and Nai Phuan Ong. The chiral anomaly and thermopower of Weyl fermions in the half-Heusler GdPtBi. *Nat. Mater.*, 15(11):1161–1165, 2016.
- [187] Jiawei Ruan, Shao-Kai Jian, Hong Yao, Haijun Zhang, Shou-Cheng Zhang, and Dingyu Xing. Symmetry-protected ideal Weyl semimetal in HgTe-class materials. *Nat. Commun.*, 7(1):1–6, 2016.
- [188] Barry Bradlyn, Jennifer Cano, Zhijun Wang, M. G. Vergniory, C. Felser, R. J. Cava, and B. Andrei Bernevig. Beyond dirac and weyl fermions: Unconventional quasiparticles in conventional crystals. *Science*, 353(6299):aaf5037, July 2016.
- [189] Klaus Koepernik and Helmut Eschrig. Full-potential nonorthogonal local-orbital minimum-basis band-structure scheme. *Phys. Rev. B*, 59:1743–1757, Jan 1999.
- [190] Wendong Cao, Peizhe Tang, Yong Xu, Jian Wu, Bing-Lin Gu, and Wenhui Duan. Dirac semimetal phase in hexagonal LiZnBi. *Phys. Rev. B*, 96:115203, Sep 2017.
- [191] Heng Gao, Jeremy Strockoz, Mario Frakulla, Jörn W. F. Venderbos, and Hongming Weng. Noncentrosymmetric topological dirac semimetals in three dimensions. *Phys. Rev. B*, 103:205151, May 2021.
- [192] Miles A White, Gordon J Miller, and Javier Vela. Polytypism and unique site preference in LiZnSb: a superior thermoelectric reveals its true colors. *J. Am. Chem. Soc.*, 138(44):14574–14577, 2016.
- [193] Uday Chopra, Mohd Zeeshan, Shambhawi Pandey, Rakshanda Dhawan, Harish K Singh, Jeroen van den Brink, and Hem C Kandpal. First-principles study of thermoelectric properties of Li-based Nowotony–Juza phases. *J. Phys. Condens. Matter*, 31(50):505504, 2019.
- [194] J. M. Luttinger. Quantum Theory of Cyclotron Resonance in Semiconductors: General Theory. *Phys. Rev.*, 102:1030–1041, May 1956.
- [195] Shuichi Murakami, Naoto Nagosa, and Shou-Cheng Zhang. SU(2) non-Abelian holonomy and dissipationless spin current in semiconductors. *Phys. Rev. B*, 69:235206, Jun 2004.
- [196] Eun-Gook Moon, Cenke Xu, Yong Baek Kim, and Leon Balents. Non-Fermi-Liquid and Topological States with Strong Spin-Orbit Coupling. *Phys. Rev. Lett.*, 111:206401, Nov 2013.

- [197] Sayed Ali Akbar Ghorashi, Pavan Hosur, and Chin-Sen Ting. Irradiated three-dimensional Luttinger semimetal: A factory for engineering Weyl semimetals. *Phys. Rev. B*, 97:205402, May 2018.
- [198] Lucile Savary, Jonathan Ruhman, Jörn W. F. Venderbos, Liang Fu, and Patrick A. Lee. Superconductivity in three-dimensional spin-orbit coupled semimetals. *Phys. Rev. B*, 96:214514, Dec 2017.
- [199] Bitan Roy, Sayed Ali Akbar Ghorashi, Matthew S. Foster, and Andriy H. Nevidomskyy. Topological superconductivity of spin-3/2 carriers in a three-dimensional doped Luttinger semimetal. *Phys. Rev. B*, 99:054505, Feb 2019.
- [200] Xi Dai, Taylor L. Hughes, Xiao-Liang Qi, Zhong Fang, and Shou-Cheng Zhang. Helical edge and surface states in HgTe quantum wells and bulk insulators. *Phys. Rev. B*, 77:125319, Mar 2008.
- [201] Jiabin Yu, Binghai Yan, and Chao-Xing Liu. Model Hamiltonian and time reversal breaking topological phases of antiferromagnetic half-Heusler materials. *Phys. Rev. B*, 95:235158, Jun 2017.
- [202] Antoine Kahn. Semiconductor surface structures. *Surface science reports*, 3(4-5):193–300, 1983.
- [203] E. H. Hall. On a new action of the magnet on electric currents. *Am. J. Math.*, 2(3):287–292, 1879.
- [204] Robert Karplus and J. M. Luttinger. Hall effect in ferromagnetics. *Phys. Rev.*, 95:1154–1160, Sep 1954.
- [205] N A Sinitsyn. Semiclassical theories of the anomalous hall effect. *J. Phys. Condens. Matter*, 20(2):023201, dec 2007.
- [206] Naoto Nagaosa, Jairo Sinova, Shigeki Onoda, A. H. MacDonald, and N. P. Ong. Anomalous hall effect. *Rev. Mod. Phys.*, 82:1539–1592, May 2010.
- [207] Cui-Zu Chang, Jinsong Zhang, Xiao Feng, Jie Shen, Zuocheng Zhang, Minghua Guo, Kang Li, Yunbo Ou, Pang Wei, Li-Li Wang, Zhong-Qing Ji, Yang Feng, Shuaihua Ji, Xi Chen, Jinfeng Jia, Xi Dai, Zhong Fang, Shou-Cheng Zhang, Ke He, Yayu Wang, Li Lu, Xu-Cun Ma, and Qi-Kun Xue. Experimental observation of the quantum anomalous hall effect in a magnetic topological insulator. *Science*, 340(6129):167–170, 2013.
- [208] Chao-Xing Liu, Shou-Cheng Zhang, and Xiao-Liang Qi. The quantum anomalous hall effect: Theory and experiment. *Annu. Rev. Condens. Matter Phys.*, 7(1):301–321, 2016.
- [209] Ke He, Yayu Wang, and Qi-Kun Xue. Topological materials: Quantum anomalous hall system. *Annu. Rev. Condens. Matter Phys.*, 9(1):329–344, 2018.

- [210] C. L. Kane and E. J. Mele. Quantum spin hall effect in graphene. *Phys. Rev. Lett.*, 95:226801, Nov 2005.
- [211] Jairo Sinova, Sergio O. Valenzuela, J. Wunderlich, C. H. Back, and T. Jungwirth. Spin hall effects. *Rev. Mod. Phys.*, 87:1213–1260, Oct 2015.
- [212] Inti Sodemann and Liang Fu. Quantum nonlinear hall effect induced by berry curvature dipole in time-reversal invariant materials. *Phys. Rev. Lett.*, 115:216806, Nov 2015.
- [213] Su-Yang Xu, Qiong Ma, Huitao Shen, Valla Fatemi, Sanfeng Wu, Tay-Rong Chang, Guoqing Chang, Andrés M. Mier Valdivia, Ching-Kit Chan, Quinn D. Gibson, Jiadong Zhou, Zheng Liu, Kenji Watanabe, Takashi Taniguchi, Hsin Lin, Robert J. Cava, Liang Fu, Nuh Gedik, and Pablo Jarillo-Herrero. Electrically switchable berry curvature dipole in the monolayer topological insulator WTe2. *Nat. Phys.*, 14(9):900–906, July 2018.
- [214] Qiong Ma, Su-Yang Xu, Huitao Shen, David MacNeill, Valla Fatemi, Tay-Rong Chang, Andrés M. Mier Valdivia, Sanfeng Wu, Zongzheng Du, Chuang-Han Hsu, Shiang Fang, Quinn D. Gibson, Kenji Watanabe, Takashi Taniguchi, Robert J. Cava, Efthimios Kaxiras, Hai-Zhou Lu, Hsin Lin, Liang Fu, Nuh Gedik, and Pablo Jarillo-Herrero. Observation of the nonlinear hall effect under time-reversal-symmetric conditions. *Nature*, 565(7739):337–342, December 2018.
- [215] Jorge I. Facio, Dmitri Efremov, Klaus Koepernik, Jhih-Shih You, Inti Sodemann, and Jeroen van den Brink. Strongly enhanced berry dipole at topological phase transitions in bitei. *Phys. Rev. Lett.*, 121:246403, Dec 2018.
- [216] Xiao-Qin Yu, Zhen-Gang Zhu, Jhih-Shih You, Tony Low, and Gang Su. Topological nonlinear anomalous nernst effect in strained transition metal dichalcogenides. *Phys. Rev. B*, 99:201410, May 2019.
- [217] Z. Z. Du, C. M. Wang, Hai-Zhou Lu, and X. C. Xie. Band signatures for strong nonlinear hall effect in bilayer wte2. *Phys. Rev. Lett.*, 121:266601, Dec 2018.
- [218] Z. Z. Du, C. M. Wang, Shuai Li, Hai-Zhou Lu, and X. C. Xie. Disorder-induced nonlinear hall effect with time-reversal symmetry. *Nat. Commun.*, 10(1), July 2019.
- [219] Z. Z. Du, Hai-Zhou Lu, and X. C. Xie. Perspective: Nonlinear hall effects, arXiv:2105.10940, 2021.

- [220] Carmine Ortix. Nonlinear hall effect with time-reversal symmetry: Theory and material realizations. *Adv. Quantum Technol.*, page 2100056, July 2021.
- [221] Michał Papaj and Liang Fu. Magnus hall effect. *Phys. Rev. Lett.*, 123:216802, Nov 2019.
- [222] Debottam Mandal, Kamal Das, and Amit Agarwal. Magnus nernst and thermal hall effect. *Phys. Rev. B*, 102:205414, Nov 2020.
- [223] Xiaofeng Qian, Junwei Liu, Liang Fu, and Ju Li. Quantum spin hall effect in two-dimensional transition metal dichalcogenides. *Science*, 346(6215):1344–1347, 2014.
- [224] Di Xiao, Gui-Bin Liu, Wanxiang Feng, Xiaodong Xu, and Wang Yao. Coupled spin and valley physics in monolayers of mos_2 and other group-vi dichalcogenides. *Phys. Rev. Lett.*, 108:196802, May 2012.
- [225] Jhih-Shih You, Shiang Fang, Su-Yang Xu, Efthimios Kaxiras, and Tony Low. Berry curvature dipole current in the transition metal dichalcogenides family. *Phys. Rev. B*, 98:121109, Sep 2018.
- [226] Edward McCann and Mikito Koshino. The electronic properties of bilayer graphene. *Rep. Prog. Phys.*, 76(5):056503, apr 2013.
- [227] A.V. Rozhkov, A.O. Sboychakov, A.L. Rakhmanov, and Franco Nori. Electronic properties of graphene-based bilayer systems. *Phys. Rep.*, 648:1–104, 2016. Electronic properties of graphene-based bilayer systems.
- [228] Raffaele Battilomo, Niccoló Scopigno, and Carmine Ortix. Berry curvature dipole in strained graphene: A fermi surface warping effect. *Phys. Rev. Lett.*, 123:196403, Nov 2019.
- [229] Matthew Yankowitz, Jiamin Xue, Daniel Cormode, Javier D. Sanchez-Yamagishi, K. Watanabe, T. Taniguchi, Pablo Jarillo-Herrero, Philippe Jacquod, and Brian J. LeRoy. Emergence of superlattice dirac points in graphene on hexagonal boron nitride. *Nat. Phys.*, 8(5):382–386, March 2012.
- [230] Liang Fu. Hexagonal warping effects in the surface states of the topological insulator bi_2te_3 . *Phys. Rev. Lett.*, 103:266801, Dec 2009.
- [231] Kai-Yu Yang, Yuan-Ming Lu, and Ying Ran. Quantum hall effects in a weyl semimetal: Possible application in pyrochlore iridates. *Phys. Rev. B*, 84:075129, Aug 2011.
- [232] A. A. Burkov, M. D. Hook, and Leon Balents. Topological nodal semimetals. *Phys. Rev. B*, 84:235126, Dec 2011.

- [233] Shuichi Murakami, Satoshi Iso, Yshai Avishai, Masaru Onoda, and Naoto Nagaosa. Tuning phase transition between quantum spin hall and ordinary insulating phases. *Phys. Rev. B*, 76:205304, Nov 2007.
- [234] Shuichi Murakami. Phase transition between the quantum spin hall and insulator phases in 3d: emergence of a topological gapless phase. *New J. Phys.*, 9(9):356–356, sep 2007.
- [235] A. A. Burkov and Leon Balents. Weyl semimetal in a topological insulator multilayer. *Phys. Rev. Lett.*, 107:127205, Sep 2011.
- [236] Xiangang Wan, Ari M. Turner, Ashvin Vishwanath, and Sergey Y. Savrasov. Topological semimetal and fermi-arc surface states in the electronic structure of pyrochlore iridates. *Phys. Rev. B*, 83:205101, May 2011.
- [237] N. P. Armitage, E. J. Mele, and Ashvin Vishwanath. Weyl and dirac semimetals in three-dimensional solids. *Rev. Mod. Phys.*, 90:015001, Jan 2018.
- [238] A. A. Zyuzin, Si Wu, and A. A. Burkov. Weyl semimetal with broken time reversal and inversion symmetries. *Phys. Rev. B*, 85:165110, Apr 2012.
- [239] Timothy M. McCormick, Itamar Kimchi, and Nandini Trivedi. Minimal models for topological weyl semimetals. *Phys. Rev. B*, 95:075133, Feb 2017.
- [240] G.E. Volovik and M.A. Zubkov. Emergent weyl spinors in multi-fermion systems. *Nucl. Phys. B*, 881:514–538, 2014.
- [241] Yong Xu, Fan Zhang, and Chuanwei Zhang. Structured weyl points in spin-orbit coupled fermionic superfluids. *Phys. Rev. Lett.*, 115:265304, Dec 2015.
- [242] Alexey A. Soluyanov, Dominik Gresch, Zhijun Wang, QuanSheng Wu, Matthias Troyer, Xi Dai, and B. Andrei Bernevig. Type-II weyl semimetals. *Nature*, 527(7579):495–498, November 2015.
- [243] Gang Xu, Hongming Weng, Zhijun Wang, Xi Dai, and Zhong Fang. Chern semimetal and the quantized anomalous hall effect in hgcr₂se₄. *Phys. Rev. Lett.*, 107:186806, Oct 2011.
- [244] Chen Fang, Matthew J. Gilbert, Xi Dai, and B. Andrei Bernevig. Multi-weyl topological semimetals stabilized by point group symmetry. *Phys. Rev. Lett.*, 108:266802, Jun 2012.
- [245] Ki-Seok Kim, Heon-Jung Kim, and M. Sasaki. Boltzmann equation approach to anomalous transport in a weyl metal. *Phys. Rev. B*, 89:195137, May 2014.

- [246] Pavan Hosur and Xiaoliang Qi. Recent developments in transport phenomena in weyl semimetals. *C. R. Phys.*, 14(9):857–870, 2013.
- [247] Xiaochun Huang, Lingxiao Zhao, Yujia Long, Peipei Wang, Dong Chen, Zhanhai Yang, Hui Liang, Mianqi Xue, Hongming Weng, Zhong Fang, Xi Dai, and Genfu Chen. Observation of the chiral-anomaly-induced negative magnetoresistance in 3d weyl semimetal taas. *Phys. Rev. X*, 5:031023, Aug 2015.
- [248] Vladimir A. Zyuzin. Magnetotransport of weyl semimetals due to the chiral anomaly. *Phys. Rev. B*, 95:245128, Jun 2017.
- [249] D. T. Son and B. Z. Spivak. Chiral anomaly and classical negative magnetoresistance of weyl metals. *Phys. Rev. B*, 88:104412, Sep 2013.
- [250] A. A. Burkov. Giant planar hall effect in topological metals. *Phys. Rev. B*, 96:041110, Jul 2017.
- [251] A A Burkov. Chiral anomaly and transport in weyl metals. *J. Phys. Condens. Matter*, 27(11):113201, feb 2015.
- [252] Yaojia Wang, Erfu Liu, Huimei Liu, Yiming Pan, Longqiang Zhang, Junwen Zeng, Yajun Fu, Miao Wang, Kang Xu, Zhong Huang, Zhenlin Wang, Hai-Zhou Lu, Dingyu Xing, Baigeng Wang, Xiangang Wan, and Feng Miao. Gate-tunable negative longitudinal magnetoresistance in the predicted type-ii weyl semimetal wte2. *Nat. Commun.*, 7(1):13142, Oct 2016.
- [253] Cheng-Long Zhang, Su-Yang Xu, Ilya Belopolski, Zhujun Yuan, Ziquan Lin, Bingbing Tong, Guang Bian, Nasser Alidoust, Chi-Cheng Lee, Shin-Ming Huang, Tay-Rong Chang, Guoqing Chang, Chuang-Han Hsu, Horng-Tay Jeng, Madhab Neupane, Daniel S. Sanchez, Hao Zheng, Junfeng Wang, Hsin Lin, Chi Zhang, Hai-Zhou Lu, Shun-Qing Shen, Titus Neupert, M. Zahid Hasan, and Shuang Jia. Signatures of the adler–bell–jackiw chiral anomaly in a weyl fermion semimetal. *Nat. Commun.*, 7(1):10735, February 2016.
- [254] S. Nandy, Girish Sharma, A. Taraphder, and Sumanta Tewari. Chiral anomaly as the origin of the planar hall effect in weyl semimetals. *Phys. Rev. Lett.*, 119:176804, Oct 2017.
- [255] F. C. Chen, X. Luo, J. Yan, Y. Sun, H. Y. Lv, W. J. Lu, C. Y. Xi, P. Tong, Z. G. Sheng, X. B. Zhu, W. H. Song, and Y. P. Sun. Planar hall effect in the type-ii weyl semimetal T_d –MoTe₂. *Phys. Rev. B*, 98:041114, Jul 2018.
- [256] Ratnadwip Singha, Shubhankar Roy, Arnab Pariari, Biswarup Satter, and Prabhat Mandal. Planar hall effect in the type-ii dirac semimetal val₃. *Phys. Rev. B*, 98:081103, Aug 2018.

- [257] Suvendu Ghosh, Debabrata Sinha, Snehasish Nandy, and A. Taraphder. Chirality-dependent planar hall effect in inhomogeneous weyl semimetals. *Phys. Rev. B*, 102:121105, Sep 2020.
- [258] Nitesh Kumar, Satya N. Guin, Claudia Felser, and Chandra Shekhar. Planar hall effect in the weyl semimetal gdptbi. *Phys. Rev. B*, 98:041103, Jul 2018.
- [259] M. Udagawa and E. J. Bergholtz. Field-selective anomaly and chiral mode reversal in type-ii weyl materials. *Phys. Rev. Lett.*, 117:086401, Aug 2016.
- [260] Fucong Fei, Xiangyan Bo, Rui Wang, Bin Wu, Juan Jiang, Dongzhi Fu, Ming Gao, Hao Zheng, Yulin Chen, Xuefeng Wang, Haijun Bu, Fengqi Song, Xiangang Wan, Baigeng Wang, and Guanghou Wang. Nontrivial berry phase and type-ii dirac transport in the layered material PdTe₂. *Phys. Rev. B*, 96:041201, Jul 2017.
- [261] Renato M. A. Dantas, Francisco Peña-Benitez, Bitan Roy, and Piotr Surówka. Magnetotransport in multi-weyl semimetals: a kinetic theory approach. *J. High Energy Phys.*, 2018(12), dec 2018.
- [262] Tanay Nag and Snehasish Nandy. Magneto-transport phenomena of type-i multi-weyl semimetals in co-planar setups. *J. Phys. Condens. Matter*, 33(7):075504, dec 2020.
- [263] Tanay Nag, Anirudha Menon, and Banasri Basu. Thermoelectric transport properties of floquet multi-weyl semimetals. *Phys. Rev. B*, 102:014307, Jul 2020.
- [264] Neil W Ashcroft and N David Mermin. *Solid state physics*. New York: Holt, Rinehart and Winston,, 1976.
- [265] John M Ziman. *Electrons and phonons: the theory of transport phenomena in solids*. Oxford university press, 2001.
- [266] Dam Thanh Son and Naoki Yamamoto. Berry curvature, triangle anomalies, and the chiral magnetic effect in fermi liquids. *Phys. Rev. Lett.*, 109:181602, Nov 2012.
- [267] Di Xiao, Yugui Yao, Zhong Fang, and Qian Niu. Berry-phase effect in anomalous thermoelectric transport. *Phys. Rev. Lett.*, 97:026603, Jul 2006.
- [268] Liang Dong, Cong Xiao, Bangguo Xiong, and Qian Niu. Berry phase effects in dipole density and the mott relation. *Phys. Rev. Lett.*, 124:066601, Feb 2020.
- [269] Yang Zhang, Yan Sun, and Binghai Yan. Berry curvature dipole in weyl semimetal materials: An ab initio study. *Phys. Rev. B*, 97:041101, Jan 2018.

- [270] Chuanchang Zeng, Snehasish Nandy, and Sumanta Tewari. Nonlinear transport in weyl semimetals induced by berry curvature dipole. *Phys. Rev. B*, 103:245119, Jun 2021.
- [271] Fernando de Juan, Adolfo G Grushin, Takahiro Morimoto, and Joel E Moore. Quantized circular photogalvanic effect in weyl semimetals. *Nature communications*, 8(1):15995, 2017.
- [272] Banasree Sadhukhan and Tanay Nag. Role of time reversal symmetry and tilting in circular photogalvanic responses. *Phys. Rev. B*, 103:144308, Apr 2021.
- [273] Rui-Chun Xiao, Zibo Wang, Zhi-Qiang Zhang, Junwei Liu, and Hua Jiang. Magnus hall effect in two-dimensional materials. *Chinese Phys. Lett.*, 38(5):057301, June 2021.
- [274] C. R. Woods, L. Britnell, A. Eckmann, R. S. Ma, J. C. Lu, H. M. Guo, X. Lin, G. L. Yu, Y. Cao, R. V. Gorbachev, A. V. Kretinin, J. Park, L. A. Ponomarenko, M. I. Katsnelson, Yu. N. Gornostyrev, K. Watanabe, T. Taniguchi, C. Casiraghi, H.-J. Gao, A. K. Geim, and K. S. Novoselov. Commensurate–incommensurate transition in graphene on hexagonal boron nitride. *Nat. Phys.*, 10(6):451–456, Jun 2014.
- [275] Gianluca Giovannetti, Petr A. Khomyakov, Geert Brocks, Paul J. Kelly, and Jeroen van den Brink. Substrate-induced band gap in graphene on hexagonal boron nitride: Ab initio density functional calculations. *Phys. Rev. B*, 76:073103, Aug 2007.
- [276] Fernando de Juan, Mauricio Sturla, and María A. H. Vozmediano. Space dependent fermi velocity in strained graphene. *Phys. Rev. Lett.*, 108:227205, May 2012.
- [277] Hualing Zeng, Junfeng Dai, Wang Yao, Di Xiao, and Xiaodong Cui. Valley polarization in MoS₂ monolayers by optical pumping. *Nat. Nanotechnol.*, 7(8):490–493, June 2012.
- [278] Kin Fai Mak, Keliang He, Jie Shan, and Tony F. Heinz. Control of valley polarization in monolayer MoS₂ by optical helicity. *Nat. Nanotechnol.*, 7(8):494–498, June 2012.
- [279] Di Xiao, Wang Yao, and Qian Niu. Valley-contrasting physics in graphene: Magnetic moment and topological transport. *Phys. Rev. Lett.*, 99:236809, Dec 2007.
- [280] Sonja Predin, Paul Wenk, and John Schliemann. Trigonal warping in bilayer graphene: Energy versus entanglement spectrum. *Phys. Rev. B*, 93:115106, Mar 2016.
- [281] Edward McCann and Vladimir I. Fal’ko. Landau-level degeneracy and quantum hall effect in a graphite bilayer. *Phys. Rev. Lett.*, 96:086805, Mar 2006.

- [282] Binghai Yan and Claudia Felser. Topological materials: Weyl semimetals. *Annu. Rev. Condens. Matter Phys.*, 8(1):337–354, 2017.
- [283] Chen Fang, Matthew J. Gilbert, Xi Dai, and B. Andrei Bernevig. Multi-weyl topological semimetals stabilized by point group symmetry. *Phys. Rev. Lett.*, 108:266802, Jun 2012.
- [284] Bohm-Jung Yang and Naoto Nagaosa. Classification of stable three-dimensional dirac semimetals with nontrivial topology. *Nat. Commun.*, 5(1):4898, September 2014.
- [285] Bitan Roy, Pallab Goswami, and Vladimir Juričić. Interacting weyl fermions: Phases, phase transitions, and global phase diagram. *Phys. Rev. B*, 95:201102, May 2017.
- [286] A. A. Burkov. Anomalous hall effect in weyl metals. *Phys. Rev. Lett.*, 113:187202, Oct 2014.
- [287] Simin Nie, Yan Sun, Fritz B. Prinz, Zhijun Wang, Hongming Weng, Zhong Fang, and Xi Dai. Magnetic semimetals and quantized anomalous hall effect in eub₆. *Phys. Rev. Lett.*, 124:076403, Feb 2020.
- [288] Helin Cao, Jifa Tian, Ireneusz Miotkowski, Tian Shen, Jiuning Hu, Shan Qiao, and Yong P. Chen. Quantized hall effect and shubnikov–de haas oscillations in highly doped bi₂se₃: Evidence for layered transport of bulk carriers. *Phys. Rev. Lett.*, 108:216803, May 2012.
- [289] Hidetoshi Masuda, Hideaki Sakai, Masashi Tokunaga, Yuichi Yamasaki, Atsushi Miyake, Junichi Shiogai, Shintaro Nakamura, Satoshi Awaji, Atsushi Tsukazaki, Hironori Nakao, Youichi Murakami, Taka hisa Arima, Yoshinori Tokura, and Shintaro Ishiwata. Quantum hall effect in a bulk antiferromagnet EuMnBi₂ with magnetically confined two-dimensional dirac fermions. *Sci. Adv.*, 2(1):e1501117, January 2016.
- [290] Masaki Uchida, Yusuke Nakazawa, Shinichi Nishihaya, Kazuto Akiba, Markus Kriener, Yusuke Kozuka, Atsushi Miyake, Yasujiro Taguchi, Masashi Tokunaga, Naoto Nagaosa, et al. Quantum hall states observed in thin films of dirac semimetal Cd₃As₂. *Nature communications*, 8(1):2274, 2017.
- [291] Cheng Zhang, Yi Zhang, Xiang Yuan, Shiheng Lu, Jinglei Zhang, Awadhesh Narayan, Yanwen Liu, Huiqin Zhang, Zhuoliang Ni, Ran Liu, Eun Sang Choi, Alexey Suslov, Stefano Sanvito, Li Pi, Hai-Zhou Lu, Andrew C. Potter, and Faxian Xiu. Quantum hall effect based on weyl orbits in Cd₃As₂. *Nature*, 565(7739):331–336, December 2018.

[292] Tian Liang, Jingjing Lin, Quinn Gibson, Satya Kushwaha, Minhao Liu, Wudi Wang, Hongyu Xiong, Jonathan A. Sobota, Makoto Hashimoto, Patrick S. Kirchmann, Zhi-Xun Shen, R. J. Cava, and N. P. Ong. Anomalous hall effect in ZrTe5. *Nat. Phys.*, 14(5):451–455, March 2018.

[293] Fangdong Tang, Yafei Ren, Peipei Wang, Ruidan Zhong, John Schneeloch, Shengyuan A. Yang, Kun Yang, Patrick A. Lee, Genda Gu, Zhenhua Qiao, and Liyuan Zhang. Three-dimensional quantum hall effect and metal–insulator transition in ZrTe5. *Nature*, 569(7757):537–541, May 2019.

[294] S. Galeski, X. Zhao, R. Wawrzynczak, T. Meng, T. Förster, P. M. Lozano, S. Honnali, N. Lamba, T. Ehmcke, A. Markou, Q. Li, G. Gu, W. Zhu, J. Wosnitza, C. Felser, G. F. Chen, and J. Gooth. Unconventional hall response in the quantum limit of HfTe5. *Nat. Commun.*, 11(1):5926, November 2020.

[295] Kaifei Kang, Tingxin Li, Egon Sohn, Jie Shan, and Kin Fai Mak. Nonlinear anomalous hall effect in few-layer WTe2. *Nat. Mater.*, 18(4):324–328, February 2019.

[296] Dushyant Kumar, Chuang-Han Hsu, Raghav Sharma, Tay-Rong Chang, Peng Yu, Junyoung Wang, Goki Eda, Gengchiau Liang, and Hyunsoo Yang. Room-temperature nonlinear hall effect and wireless radiofrequency rectification in weyl semimetal TaIrTe4. *Nat. Nanotechnol.*, 16(4):421–425, January 2021.

[297] M. Büttiker. Four-terminal phase-coherent conductance. *Phys. Rev. Lett.*, 57:1761–1764, Oct 1986.

[298] N. P. Butch, P. Syers, K. Kirshenbaum, A. P. Hope, and J. Paglione. Superconductivity in the topological semimetal yptbi. *Phys. Rev. B*, 84:220504, Dec 2011.

[299] C. Timm, A. P. Schnyder, D. F. Agterberg, and P. M. R. Brydon. Inflated nodes and surface states in superconducting half-heusler compounds. *Phys. Rev. B*, 96:094526, Sep 2017.

[300] M. Mofazzel Hosen, Gyanendra Dhakal, Klauss Dimitri, Hongchul Choi, Firoza Kabir, Christopher Sims, Orest Pavlosiuk, Piotr Wiśniewski, Tomasz Durakiewicz, Jian-Xin Zhu, Dariusz Kaczorowski, and Madhab Neupane. Observation of dirac state in half-heusler material YPtBi. *Scientific Reports*, 10(1), July 2020.

[301] F. F. Tafti, Takenori Fujii, A. Juneau-Fecteau, S. René de Cotret, N. Doiron-Leyraud, Atsushi Asamitsu, and Louis Taillefer. Superconductivity in the noncentrosymmetric half-heusler compound luptbi: A candidate for topological superconductivity. *Phys. Rev. B*, 87:184504, May 2013.

- [302] Z. K. Liu, L. X. Yang, S.-C. Wu, C. Shekhar, J. Jiang, H. F. Yang, Y. Zhang, S.-K. Mo, Z. Hussain, B. Yan, C. Felser, and Y. L. Chen. Observation of unusual topological surface states in half-heusler compounds LnPtBi ($\text{Ln}=\text{Lu, Y}$). *Nature Communications*, 7(1), September 2016.
- [303] Cheng-Ping Zhang, Jiewen Xiao, Benjamin T. Zhou, Jin-Xin Hu, Ying-Ming Xie, Binghai Yan, and K. T. Law. Giant nonlinear hall effect in strained twisted bilayer graphene. arXiv:2010.08333, 2020.
- [304] Mikael C. Rechtsman, Julia M. Zeuner, Yonatan Plotnik, Yaakov Lumer, Daniel Podolsky, Felix Dreisow, Stefan Nolte, Mordechai Segev, and Alexander Szameit. Photonic floquet topological insulators. *Nature*, 496(7444):196–200, Apr 2013.
- [305] Gregor Jotzu, Michael Messer, Rémi Desbuquois, Martin Lebrat, Thomas Uehlinger, Daniel Greif, and Tilman Esslinger. Experimental realization of the topological haldane model with ultracold fermions. *Nature*, 515(7526):237–240, November 2014.
- [306] Karen Wintersperger, Christoph Braun, F. Nur Ünal, André Eckardt, Marco Di Liberto, Nathan Goldman, Immanuel Bloch, and Monika Aidelsburger. Realization of an anomalous floquet topological system with ultracold atoms. *Nat. Phys.*, 16(10):1058–1063, June 2020.
- [307] Sebabrata Mukherjee, Alexander Spracklen, Manuel Valiente, Erika Andersson, Patrik Öhberg, Nathan Goldman, and Robert R. Thomson. Experimental observation of anomalous topological edge modes in a slowly driven photonic lattice. *Nat. Commun.*, 8(1):13918, Jan 2017.
- [308] Lukas J. Maczewsky, Julia M. Zeuner, Stefan Nolte, and Alexander Szameit. Observation of photonic anomalous floquet topological insulators. *Nat. Commun.*, 8(1), January 2017.

List of figures

1.3 Formation of the cyclotron orbits in the bulk, and skipping orbits at the edge of the system is shown. Magnetic field is applied perpendicular to the plane, and it gives rise to an anti-clockwise motion of the electrons. It is seen that at the upper edge of the sample, while electrons perform half of the orbital motion in the right direction, at the bottom edge they will do the same but in the opposite (left) direction. This happens so that the net current is conserved, giving rise to edge current at the boundaries of the sample.

1.4 (a) Graphene with nearest and next-nearest neighbor hopping. $\hat{a}_1 = (1, 0)$, $\hat{a}_2 = (\frac{1}{2}, \frac{\sqrt{3}}{2})$ are the Bravais lattice vectors. Different sub-lattice(s) in the unit cell of graphene is indicated by blue and orange colors respectively. (b) Gapped bulk bandstructure of graphene with Kane-Mele Hamiltonian [24]. In presence of the second nearest neighbor term, bulk Dirac cones get gapped. (c) Bandstructure in the slab geometry is shown for $W = 60$ unit cells finite along the \hat{a}_2 -direction. Parameters taken as $t = 1$, $t_2 = 0.15$, $\lambda_v = 0.1$. energy ε , and momentum k are measured in the unit of t , and $1/a_1$ respectively. λ_v is the staggered sub-lattice potential (λ_v). Gapless spin-polarized helical edge states are depicted, i.e. at each edge of the system, there is counter-propagating edge states corresponding to spin up and spin down channel.

1.5 (a) Tetragonal lattice structure with two atoms A and B in the unit cell. (b) Bulk bandstructure for the Hamiltonian as mentioned in Eq. (2) of [40]. It can be seen that the bulk spectrum is gapped everywhere in the BZ. (c) Slab bandstructure for (001) surface shows the existence of topologically protected gapless states. The gapless surface states originating from the C_4 crystalline symmetry are quadratic in nature.

1.6 (a) Schematic BZ for a topological crystalline insulator with mirror symmetry M_y . Due to M_y , there are two planes in the surface BZ which are left invariant, namely $k_y = 0, \pi$. (b) Schematic surface band structure (along $k_x = 0$ cut) with two chiral edge states for each mirror invariant plane. 17

2.1 Left: Three-dimensional system formed out of graphene layers (horizontal lines) separated by thin insulating layers (gray boxes). The spacers are polar, having a positively charged (+) and a negatively charged (−) side. Using spacer layers with an alternating orientation leads to graphene sheets which have an alternating doping ($\pm\mu$). The unit cell of the heterostructure (bracket) consists of two graphene layers, and the full system shows reflection symmetry about one layer (\mathcal{R}). By applying a uniform magnetic field along the stacking direction, neighboring graphene layers form quantum Hall phases with opposite Chern numbers, such that their chiral edge states propagate in opposite directions (horizontal arrows). Right: our conventions for the graphene lattice, with Bravais vectors \vec{e}_x and \vec{e}_y . Nearest and next nearest neighbor hoppings are labeled t and t_2 . There are two sites, denoted a and b in every unit cell (marked by a blue contour). 26

3.3	Panel (a): Triangular lattice model of H_{TI} , Eqs. (3.2) and (3.4). Sites are shown in black, hoppings in gray, and mirror planes as shaded areas. The blue arrows represent Bravais vectors $\mathbf{a}_{1,2,3}$. Panel (b): Bandstructure of the model defined by Eqs. (3.8) and (3.4) computed in a slab geometry. Only states on the top surface are shown. Panel (c): Cut of the same bandstructure along the $k_1 = k_2$ mirror plane, with k_m labeling the momentum along the mirror plane. Panel (d): Bandstructure for model defined by Eqs. (3.8) and (3.5), along the same $k_1 = k_2$ mirror plane. All bandstructures are obtained in a slab geometry with hard wall boundary conditions perpendicular to \mathbf{a}_3 and a thickness of 40 unit cells. In (b) and (c) we set $\mu = 3$, $\lambda = 1$, $\alpha = 5$, and $\varepsilon = 0.4$, whereas $\varepsilon = 0.1$ in panel (d). The color scale in panels (c) and (d) denotes the integrated probability density of wavefunctions on the top- and bottom-most 8 sites of the slab, such that surface modes appear in red (dark gray) and bulk modes in light green (light gray).	46
3.4	Bandstructure of Pd_2HgSe_3 and of Pt_2HgSe_3 . The inset presents a zoom of the area enclosed by the red dotted-line square.	49
3.5	Momentum-resolved surface spectral densities of Pd_2HgSe_3 . Left: [100] surface. Right: [001] surface. A pair of Dirac cones associated with the mirror Chern number are observed at \bar{X}	50

3.6	Bandstructure of the model obtained using Eq. (3.9) in an infinite slab geometry, with thickness of 40 unit cells in the z direction, using $\mu = 3$ and $\lambda = 1$. Only states which are localized on the top surface and have energies $ E \leq 1$ are shown. To better visualize the surface Dirac cones, we set $\alpha = \varepsilon = 0$, such that each Dirac cone is doubly degenerate. The hexagonal contour marks the boundary of the surface BZ, mirror invariant lines are shown in dashed red, and black arrows indicate the reciprocal lattice vectors of the surface $\mathbf{b}_1 = (\sqrt{3}/2, 1/2)$ and $\mathbf{b}_2 = (0, -1)$	52
3.7	Sketch of the real-space hopping terms corresponding to the function $f^{(X)}$ of Eq. (3.9). Shown is the triangular lattice describing H_{TI} at constant z coordinate. Starting from a site on The hopping amplitudes are $t_1 = -3/8$ (blue dotted lines), $t_2 = 3/16$ (orange dashed lines), and $t_3 = 3/32$ (green solid lines). The structure of the hoppings preserves the three-fold rotation symmetry of the model.	53
4.1	(a) Crystal structure. (b) Brillouin zone. (c,d) Band structure and density of states of LiBiZn and LiSbZn, respectively. The weight associated with Bi-6p (or Sb-5p) is depicted in orange while that of Zn-4s, Bi-6s (or Sb-5s) and Li-2s in blue.	59
4.2	(a) Band structure of LiBiZn under uniaxial strain $\delta = -0.02$. Thinner black curves are the bands without strain. (b) Band structure for $\delta = 0.02$. The path chosen include one of the eight Weyl nodes found in the $k_z = 0$ plane, of coordinates $\frac{2\pi}{a}(0.017, 0.006, 0)$	61
4.3	(a) [1,-1,0] Zn-terminated surface spectral density structure of LiBiZn under uniaxial strain $\delta = -0.02$. The panel on the right is a zoom of the white square in the left panel. (b) Analogous results for strain $\delta = 0.02$. (c),(d) Zoom of the data in (a),(b), respectively. The path width in the zooms is $0.04 \times 2\pi/a$	62

4.4	(a) Wilson loop in the $k_z = 0$ plane for the four band model Eq. 4.1 with $\delta < 0$. (b) Same for $\delta > 0$. (c) Wannier center evolution in the plane defined by the TRIMs Γ , $\vec{G}_1/2$ and $\vec{G}_2/2$ for LiZnBi under compressive strain. (d) Same as (c) in the case of tensile strain.	64
4.5	Schematic diagram of the column geometry (top view). Blue circles correspond to Bi (or Sb) and orange circles correspond to Zn. Li is omitted for clarity. Bulk, surface and hinge regions are denoted by the boxes labelled with B, S and H respectively. Notice also that the downfolded Hamiltonian does not contain orbitals at the Li site.	65
4.6	Hinge band structure in the absence of strain for a system having 14×14 unit cells along the \hat{y} and \hat{z} directions and infinite along \hat{x} . (a),(b) Energy dispersion for LiBiZn and LiSbZn, respectively. Larger point sizes indicate larger amplitude of the wavefunction at the hinges. The color code compares the probability amplitude of the wavefunctions at the hinges and surfaces, such that pure red corresponds to a hinge mode, pure blue to a surface state, and white to a state with equal probability per site in both regions. (c),(d) Local density of states for LiBiZn and LiSbZn, respectively, at $\varepsilon = -0.35$ eV.	66
4.7	Change in the energy of the hinge modes at $k_x = 0$ ($\Delta\varepsilon_0$) and $k_x = \pi$ ($\Delta\varepsilon_0$) as a function of uniaxial strain perpendicular to the hinge.	67
4.8	band structure for (a) LiBiZn and (b) LiSbZn is shown. Red, blue and green colors indicate the band structures obtained from DFT, full wannier tight-binding, and truncated wannier tight-binding Hamiltonian respectively. The k -path is chosen as same in 4.1.	70

5.1 The evolution of BC and Fermi surface in ML graphene (5.16) with warping $\lambda_1 = \lambda_2 = \lambda_3 = \lambda$ and strain $v_2 \neq v_1$. Top panel: The BC ($\Omega_z^{ML}(\mathbf{k}, \zeta = +1)$) and x component of the velocity ($v_x^{ML}(\mathbf{k}, \zeta = +1)$) over the Fermi surface are shown for (a) unstrained ML graphene without warping ($v_2 = v_1, \lambda = 0$), and strained ML graphene ($v_2 = 2v_1$) with C_3 symmetric warping of different strengths (b) $\lambda = 0.2$, (c) $\lambda = 0.35$, (d) $\lambda = 0.5 \text{ eV}\cdot\text{\AA}^2$. Bottom panel: (e)-(h) depict $\Omega_z^{ML}(\mathbf{k}, \zeta = -1)$ and $v_x^{ML}(\mathbf{k}, \zeta = -1)$. The strength of $\Omega_z^{ML}(\mathbf{k}, \zeta)$ and $v_x^{ML}(\mathbf{k}, \zeta)$ are represented in the color codes side by side. The parameters (in the units of energy eV) used in the calculations are $\Delta_g = 0.06 \text{ eV}$, $v_1 = 0.87 \text{ eV}\cdot\text{\AA}$. The Fermi surface is plotted for the constant energy $E = -0.28 \text{ eV}$ 85

5.2 The total valley summed contributions of (a) MH conductivity σ (in the unit of $10^{-3} \text{ e}^2/\text{V}\cdot\text{A}$) and (b) MN conductivity α (in the unit of $10^{-5} \text{ eV}\cdot\text{A}/\text{V}\cdot\text{K}$) in the presence of strain ($v_2 = 2v_1$) for different warping strengths $\lambda = 0.2, 0.35$ and $0.5 \text{ eV}\cdot\text{\AA}^2$ are shown for ML graphene. Noticeably, the warping can enhance the responses even after valley sum is performed, as it generates asymmetric contributions between valleys. We consider $\Delta U = 0.01 \text{ eV}$ and $k_B T = 0.001 \text{ eV}$. All other parameters are kept same as that of in Fig. 5.1. The chemical potential μ is chosen in the unit of eV throughout the paper. 89

5.3 The evolution of BC and Fermi surface in BL graphene (5.23) with strain w for warping $\lambda_1 = \lambda_2 = \lambda_3 = \lambda = 0.001 \text{ eV}\cdot\text{\AA}^2$. Left column: The BC $\Omega_z^{BL}(\mathbf{k}, \zeta = +1)$ and $v_x^{BL}(\mathbf{k}, \zeta = +1)$ over the Fermi surface of BL graphene (a) $w = -3m$, (c) $w = -m$, (e) $w = 0$, (g) $w = m$ and (i) $w = 3m$ are shown. Right column: We repeat the same set of calculations for $\zeta = -1$ valley. The parameters (in the units of eV) used are $\Delta_g = 0.06 \text{ eV}$, $m = 0.008 \text{ eV}\cdot\text{\AA}^2$, and $v = 0.5 \text{ eV}\cdot\text{\AA}$. The Fermi surface is plotted for the constant energy $E = -0.04 \text{ eV}$ 91

5.4 Valley responses of (a) MH (in the unit of $10^2 e^2/$), (b) MN (in the unit of $10^{-1} e k_B/$) conductivities in BL graphene with $\Delta U = 0.01$ eV, and $k_B T = 0.001$ eV for $w = -3m, 0, 3m$. All other parameters are kept same as that of in Fig. 5.3. The prominent and asymmetric valley responses in presence of strain for BL graphene are markedly different from the symmetric responses for ML graphene. 93

5.5 Valley summed (a) MH (in the unit of $10e^2/$), (b) MN (in the unit of $10^{-2} e k_B/$) conductivities in BL graphene for $w = -3m, 0, 3m$. The transport behavior changes with strain substantially. We consider the same parameters as used in Fig. 5.4. 95

5.6 Evolution of BC and Fermi surface, calculated from Eq. (5.27), with different warping strengths (a) $\lambda=50$ eV·Å³, (b) $\lambda=200$ eV·Å³ and (c) $\lambda=400$ eV·Å³ are shown. Fermi surface is plotted for $E=-0.05$ eV. We note that for $\lambda=50$ eV·Å³, the Fermi surface remains circular, which gradually evolves to hexagonal shape with increasing λ . We consider $v=1$ eV·Å and $E_0=0$ in our calculation. 96

5.7 (a) MH (in the unit of $10^{-2} e^2/$) and (b) MN (in the unit of $10^{-4} e k_B/$) conductivities as a function of chemical potential for different warping strength $\lambda = 50, 200$ and 400 eV·Å³ are depicted. The parameters used are $v=1$ eV·Å, $\Delta U = 0.01$ eV, and $k_B T = 0.001$ eV. 98

5.8 The distribution of the BC and the Fermi surfaces, calculated from Eq. (5.31), in (a) [(d)] single Weyl node with $n = 1$, (b) [(e)] double Weyl node with $n = 2$ and (c) [(f)] triple Weyl node with $n = 3$ for untilted case i.e., $C_+ = 0$ [tilted case i.e., $C_+ = 2.0$] are shown. The Fermi surface is calculated for $E=-0.05$ eV with $v = 1$ eV·Å. The deformation of BC is clearly observed with increasing non-linearity and anisotropy in the WSM. 99

5.9 (a) MH (in the unit of $10e^2/$) and (b) MN (in the unit of $ek_B/$) conductivities are shown for tilted and untilted Weyl nodes with $\zeta = +1$. We consider $v = 1 \text{ eV}\cdot\text{\AA}$, $\Delta U = 0.01 \text{ eV}$, and $k_B T = 0.001 \text{ eV}$. We observe that the untilted Weyl node with $C_+ = 0$ (tilted Weyl node with $C_+ = 0.6$) results in null (substantial) Magnus responses. We note that MH and MN conductivities are exactly opposite at two opposite Weyl nodes with $\zeta = +1$ and -1 owing to the anti-symmetric nature of BC (Eq. (5.33)). 101

5.10 (a) MH (in the unit of $10e^2/$) conductivity is shown for different strengths of the tilting parameter (C_+) for fixed $n = 1$. Gradual increase in the response is observed with increasing tilt strength C_+ . All other parameters are kept same as mentioned in Fig. 5.9. 104

List of tables

4.1	Tight-binding parameters for LiBiZn and LiSbZn.	69
-----	---	----

Declaration

Hiermit versichere ich, dass ich die vorliegende Arbeit ohne unzulässige Hilfe Dritter und ohne Benutzung anderer als der angegebenen Hilfsmittel angefertigt habe; die aus fremden Quellen direkt oder indirekt übernommenen Gedanken sind als solche kenntlich gemacht. Die Arbeit wurde bisher weder im Inland noch im Ausland in gleicher oder ähnlicher Form einer anderen Prüfungsbehörde vorgelegt.

Die vorliegende Dissertation wurde vom 04.10.2017 bis 30.09.2021 am Leibniz-Institut für Festkörper- und Werkstoffforschung Dresden (IFW Dresden), Institut für theoretische Festkörperphysik (ITF), unter der Betreuung von Prof. Dr. Jeroen van den Brink und Dr. Ion Cosma Fulga angefertigt.

Es haben keine erfolglosen Promotionsverfahren in der Vergangenheit stattgefunden. Die aktuelle Promotionsordnung der Fakultät Mathematik und Naturwissenschaften der Technischen Universität Dresden wird anerkannt.

Sanjib Kumar Das
geboren am 25.06.1993 in Kalkutta, Indien
February 2022